Timing molecular motion and production with a synthetic transcriptional clock

Elisa Franco[*,1], Eike Friedrichs[2], Jongmin Kim[3], Ralf Jungmann[2], Richard Murray[1], Erik Winfree[3,4,5], and Friedrich C. Simmel[2]

[1] *Control and Dynamical Systems, California Institute of Technology, 1200 E. California Blvd, Pasadena, CA 91125, USA*

[2] *Lehrstuhl für Bioelektronik, Physik Department, Technische Universität München, Am Coulombwall 4a, 85748 Garching, Germany*

[3] *Bioengineering, California Institute of Technology, 1200 E. California Blvd, Pasadena, CA 91125, USA*

[4] *Computation and Neural Systems, California Institute of Technology, 1200 E. California Blvd, Pasadena, CA 91125, USA*

[5] *Computer Science, California Institute of Technology, 1200 E. California Blvd, Pasadena, CA 91125, USA*

[*] Present address: Department of Mechanical Engineering, University of California at Riverside, 900 University Ave, Riverside, CA 92125, USA

Contents

1 DNA Sequences

The following DNA sequences were either ordered from IDT DNA (Belgium), IDT DNA (Coralville, IA, USA), IBA (Göttingen, Germany) or biomers.net (Ulm, Germany). These sequences are taken from Kim [2007] and Kim and Winfree [2011].

Oscillator sequences:

T12-t 5'-TTT CTG ACT TTG TCA GTA TTA GTG TGT AGT AGT AGT TCA TTA GTG TCG TTC GTT CTT TGT TTC TCC CTA TAG TGA GTC G

T12-nt 5'-TAMRA-AAG CAA GGG TAA GAT GGA ATG ATA ATA CGA CTC ACT ATA GGG AGA AAC AAA GAA CGA ACG ACA CTA ATG AAC TAC TAC TAC ACA CTA ATA CTG ACA AAG TCA GAA A

T21-t 5'-TTT CTG ACT TTG TCA GTA TTA TCA TTC CAT CTT ACC CTT GCT TCA ATC CGT TTT ACT CTC CCT ATA GTG AGT CG

T21-nt 5'-TexasRed-CAT TAG TGT CGT TCG TTC ACA GTA ATA CGA CTC ACT ATA GGG AGA GTA AAA CGG ATT GAA GCA AGG GTA AGA TGG AAT GAT AAT ACT GAC AAA GTC AGA AA

dI1 5'-GTG TGT AGT AGT AGT TCA TTA GTG TCG TTC GTT CAC AG

A1 5'-TAT TAC TGT GAA CGA ACG ACA CTA ATG AAC TAC TAC-Iowa Black RQ

A2 5'-TAT TAT CAT TCC ATC TTA CCC TTG CTT CAA TCC GT-Iowa Black RQ

rA1 (RNA) 5'-GGG AGA AAC AAA GAA CGA ACG ACA CUA AUG AAC UAC UAC UAC ACA CUA AUA CUG ACA AAG UCA GAA A

rI2 (RNA) 5'-GGG AGA GUA AAA CGG AUU GAA GCA AGG GUA AGA UGG AAU GAU AAU ACU GAC AAA GUC AGA AA

For the data collected in sets 4, 5 and 6 (for details on the data sets, refer to Section 3), T12-nt was labeled with the dye TYE563 instead of TAMRA and T21-nt with TYE665 instead of Texas Red.

For set 6, due to technical constraints of the supplier IDT DNA, T21-nt and T12-nt were respectively shortened of 1 and 6 bases from the 3' end, to have a length of 100 bases. These modifications do not alter the regulatory domains of the switch templates. Also the full length of the main transcription products was not affected, as verified by gel electrophoresis.

Tweezers subsystem (mode I – mode IV):

TW A 5'-RhodamineGreen-TGC CTT GTA AGA GCG ACC ATC AAC CTG GAA TGC TTC GGA T-BHQ1

TW B (I) 5'-CTG TGA ACG AAC GAC ATC CGA AGC ATT CCA GGT

TW C (I) 5'-GGT CGC TCT TAC AAG GCA ACT AAT GAA CTA CTA

TW B (II) 5'-GTT CAT TAG TGT CGT ATC CGA AGC ATT CCA GGT

TW C (II) 5'-GGT CGC TCT TAC AAG GCA TCG TTC ACA GTA ATA

TW B (II*) 5'-TGA AGC AAG GGT AA ATC CGA AGC ATT CCA GGT

TW C (II*) 5'-GGT CGC TCT TAC AAG GCA GAT GGA ATG ATA ATA

TW B (III) 5'-TAT CAT TCC ATC TTA CCC TAT CCG AAG CAT TCC AGG T

TW C (III) 5'-GGT CGC TCT TAC AAG GCA TGC TTC AAT CCG TTT TAC T

TW B (IV) 5'-GTA GTA GTT CAT TAG ATC CGA AGC ATT CCA GGT

TW C (IV) 5'-GGT CGC TCT TAC AAG GCA TGT CGT TCG TTC TTT GTT T

Tweezers insulating subsystem (mode V):

Ins*-nt 5'-CAT TAG TGT CGT TCG TTC ACA GTA ATA CGA CTC ACT ATA GGG AGA TCA AAT TTA CAA CGC AAC TAA CAT ATA ATC GAA GAC TTA ATA CTG ACA AAG TCA

Ins*-t 5'-TTT CTG ACT TTG TCA GTA TTA AGT CTT CGA TTA TAT GTT AGT TGC GTT GTA AAT TTG ATC TCC CTA TAG TGA GTC G

Ins-nt 5'-AAG CAA GGG TAA GAT GGA ATG ATA ATA CGA CTC ACT ATA GGG AGA TCA AAT TTA CAA CGC AAC TAA CAT ATA ATC GAA GAC TTA ATA CTG ACA AAG TC

Ins-t 5'-TTT CTG ACT TTG TCA GTA TTA AGT CTT CGA TTA TAT GTT AGT TGC GTT GTA AAT TTG ATC TCC CTA TAG TGA GTC G

InsOut (RNA) 5'-GGG AGA UCA AAU UUA CAA CGC AAC UAA CAU AUA AUC GAA GAC UUA AUA CUG ACA AAG UCA GAA A

TwCls 5'-AAG TCT TCG ATT ATA TGT TAG TTG CGT TGT AAA TTT GA

TW B (V) 5'-TCA AAT TTA CAA CGC ATC CGA AGC ATT CCA GGT

TW C (V) 5'-GGT CGC TCT TAC AAG GCA AAC TAA CAT ATA ATC

Note that Ins*-t and Ins-t are identical. Mode I tweezers are constructed by hybridizing the arms of the central strand (TW A) with the two flanking strands TW B (I) and TW C (I). Mode II - V tweezers are constructed analogously. Due to technical constraints of the supplier IDT DNA, the 3' ends of the insulators non-template strands are a few bases shorter than the corresponding template strand. This is shown in Figures S7 and S8. This did not affect their regulatory domains nor the length of their transcription products.

Malachite Green subsystem:

MG-t 5'-GAT CCA TTC GTT ACC TGG CTC TCG CCA GTC GGG ATC CCT ATA GTG AGT CG

MG-nt 5'-CAT TAG TGT CGT TCG TTC ACA GTA ATA CGA CTC ACT ATA GGG ATC CCG ACT GGC GAG AGC CAG GTA ACG AAT GGA TC

MG gene (as) 5'-GGA TCC ATT CGT TAC CTG GCT CTC GCC AGT CGG GAT CCT ATA GTG AGT CGT ATT A

MG gene (s) 5'-TAA TAC GAC TCA CTA TAG GAT CCC GAC TGG CGA GAG CCA GGT AAC GAA TGG ATC C

rMG aptamer (RNA) 5'-GGG AUC CCG ACU GGC GAG AGC CAG GUA ACG AAU GGA UC

rMG gene aptamer (RNA) 5'-GGA UCC CGA CUG GCG AGA GCC AGG UAA CGA AUG GAU CC

MG-t and MG-nt constitute the Switch TMG1, MG gene (s) and MG gene (as) are used for preproduction of MG aptamer. The TMG1 Switch and the MG gene present some incidental differences in the consensus and transcribed regions (the aptamer domain does not change). Such differences did not quantitatively affect our experimental results in a significant way. In this paper, we will denote the MG switch aptamer output as rMG, unless otherwise indicated.

2 Relevant Sequence Interactions

This section contains a series of schematic figures, which represent the most relevant predicted interactions among the nucleic acids composing the oscillator and tweezers system. The color coding for the different domains follows the one chosen for the figures in the main paper. These schemes have an illustrative purpose and are not an exhaustive list of all secondary structures that can occur in the system. Toehold-mediated branch migration reactions will be listed and analyzed when the exposed toeholds are longer than 4 bases. We will neglect reactions involving toeholds 4 bases or shorter, under the assumption that the corresponding time scales exceed the oscillator dynamics. Under each figure, we report the reactions that are numerically fitted and analyzed with the extended model in Section 24 and following. Reaction pathway examples are reported for the subsystems where data were not numerically fitted.

As evidenced in Kim and Winfree [2011] through gel electrophoresis, a number of short RNA species accumulates over time during an oscillator experiment. Such short species have lengths between 5-30 bases and are the product of abortive RNAP transcription and incomplete degradation by RNase H. It is known that RNase H may fail to degrade up to 7 RNA bases on the 3' end of DNA in an RNA-DNA duplex. In this section we will only highlight potential interactions of the oscillator and tweezer strands with incomplete degradation products of maximum length. The detailed reactions involving incomplete degradation products can be found in Section 24.

SW12

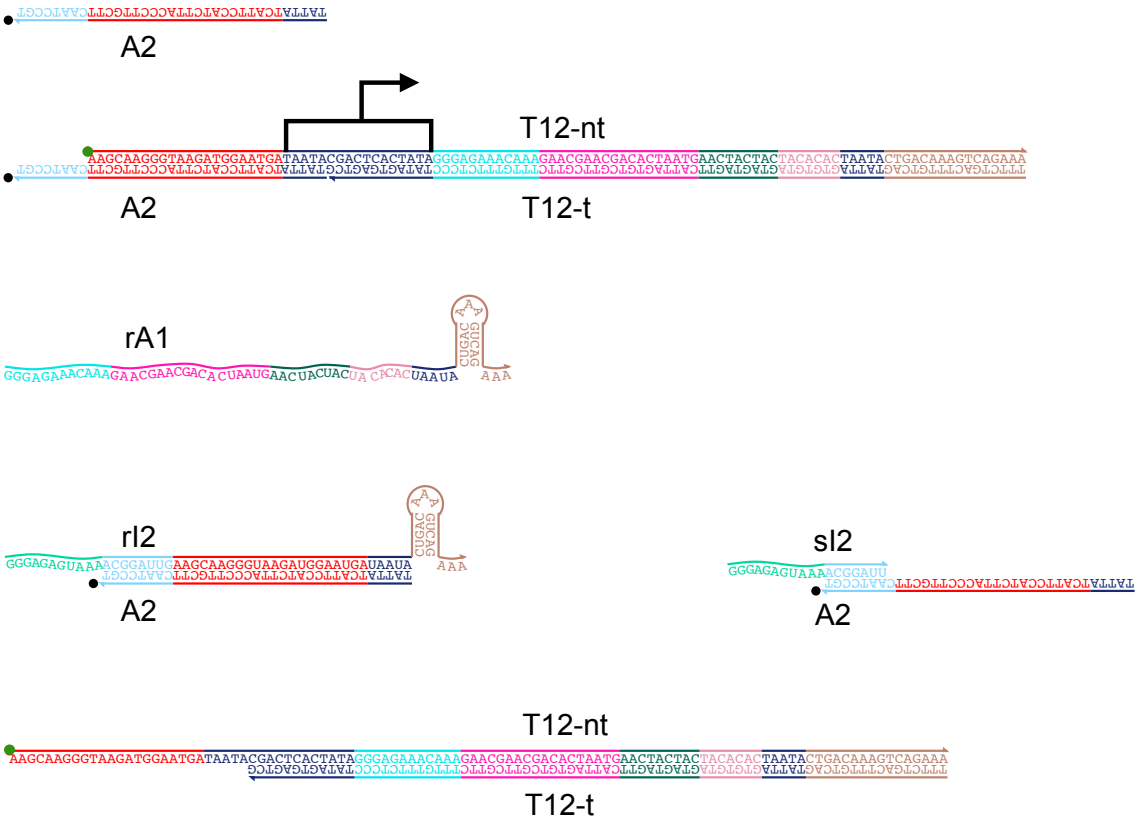

Figure S1: Scheme of relevant interactions for SW12. From top to bottom: activator A2; on-state SW12; output rA1 of SW12; activator A2 sequestered by the RNA input rI2; incomplete RNase H degradation product sI2, binding to A2; off-state SW12.

	Reaction Pathways
Activation:	$\mathrm{A2} + \mathrm{T12} \rightharpoonup \mathrm{T12 \cdot A2}$
Inhibition:	$\mathrm{rI2} + \mathrm{T12 \cdot A2} \rightharpoonup \mathrm{rI2 \cdot A2} + \mathrm{T12}$
Annihilation:	$\mathrm{A2} + \mathrm{rI2} \rightharpoonup \mathrm{rI2 \cdot A2}$
Transcription:	$\mathrm{T12 \cdot A2} + \mathrm{RNAP} \rightleftharpoons \mathrm{T12 \cdot A2 \cdot RNAP} \rightharpoonup \mathrm{rA1} + \mathrm{T12 \cdot A2} + \mathrm{RNAP}$
	$\mathrm{T12} + \mathrm{RNAP} \rightleftharpoons \mathrm{T12 \cdot RNAP} \rightharpoonup \mathrm{rA1} + \mathrm{T12} + \mathrm{RNAP}$
Degradation:	$\mathrm{rI2 \cdot A2} + \mathrm{RNaseH} \rightleftharpoons \mathrm{rI2 \cdot A2 \cdot RNaseH} \rightharpoonup \mathrm{sI2 \cdot A2} + \mathrm{RNaseH}$

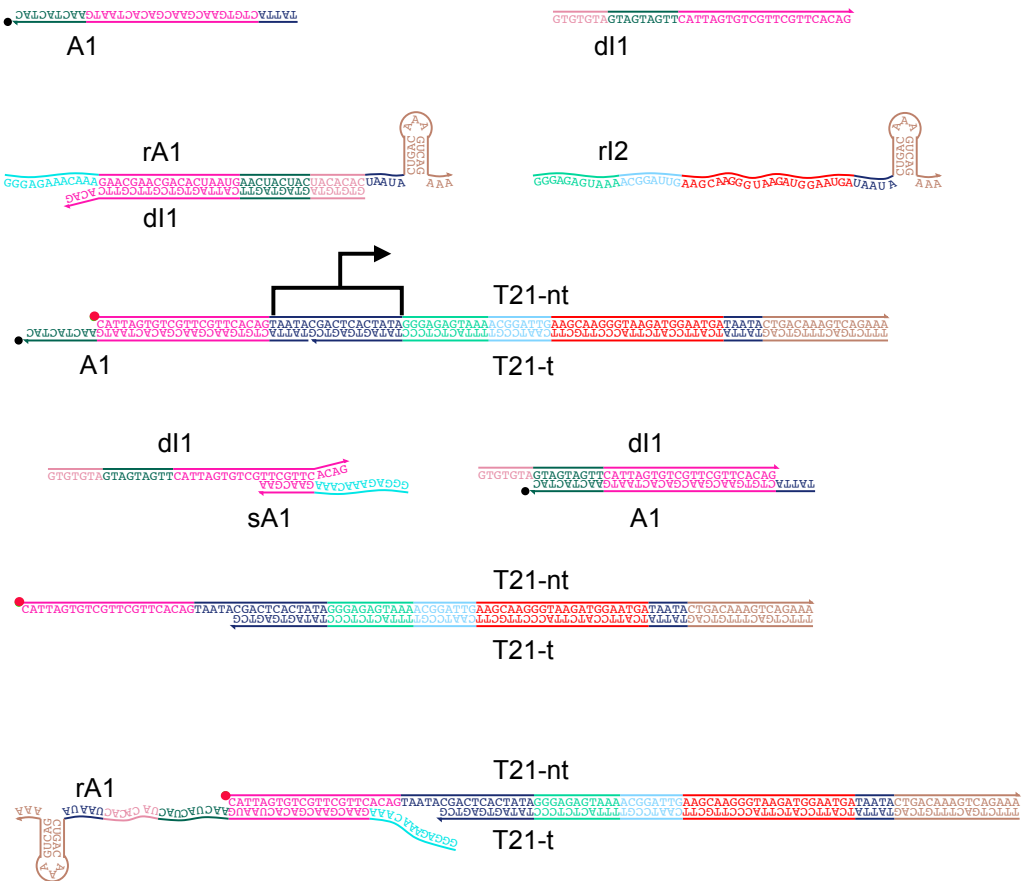

Figure S2: Relevant interactions for SW21. From top to bottom: activator A1 and inhibitor dI1; dI1 sequestered by RNA input rA1 and output rI2 of SW21; on-state SW21; incomplete RNase H degradation product sA1 binding to dI1 and dI1 sequestering the activator A1; off-state SW21; finally, unwanted interaction between RNA input rA1 and off-state SW21. The latter complex is a substrate for RNase H; moreover rA1 has a 16 bases toehold for initiation of strand displacement by inhibitor dI1, and a 9 bases domain exposed for A1 invasion. The T21·rA1 substrate does not represent a suitable binding site for RNA polymerase (Section 18).

Reaction Pathways

Activation:	$A1 + T21 \rightharpoonup T21 \cdot A1$
Inhibition:	$dI1 + T21 \cdot A1 \rightharpoonup dI1 \cdot A1 + T21$
Release:	$rA1 + dI1 \cdot A1 \rightharpoonup rA1 \cdot dI1 + A1$
Annihilation:	$dI1 + A1 \rightharpoonup dI1 \cdot A1$
	$dI1 + rA1 \rightharpoonup dI1 \cdot rA1$
Transcription:	$T21 \cdot A1 + RNAP \rightleftharpoons T21 \cdot A1 \cdot RNAP \rightharpoonup rI2 + T21 \cdot A1 + RNAP$
	$T21 + RNAP \rightleftharpoons T21 \cdot RNAP \rightharpoonup rI2 + T21 + RNAP$
Degradation:	$rA1 \cdot dI1 + RNaseH \rightleftharpoons rA1 \cdot dI1 \cdot RNaseH \rightharpoonup dI1 + RNaseH$

Unmodeled Reactions

Interfering:	$rA1 + T21 \rightharpoonup T21 \cdot rA1$
Recapturing:	$dI1 + T21 \cdot rA1 \rightharpoonup rA1 \cdot dI1 + T21$
Recovering:	$A1 + T21 \cdot rA1 \rightharpoonup A1 \cdot T21 + rA1$
Degradation:	$T21 \cdot rA1 + RNaseH \rightleftharpoons T21 \cdot rA1 \cdot RNaseH \rightharpoonup T21 + RNaseH$

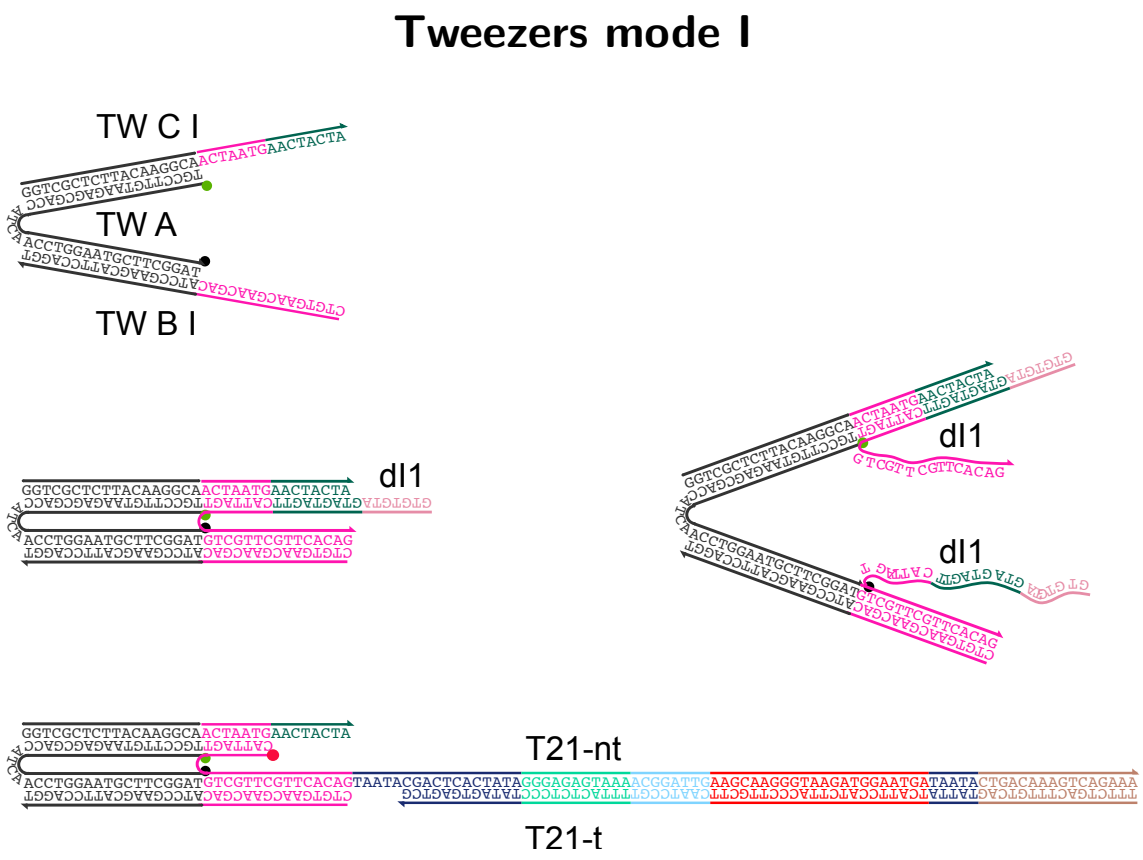

Figure S3: Relevant interactions for tweezers mode I. From top to bottom: tweezers mode I in open state; tweezers in closed state bound to their target dI1. Finally, unwanted interaction between open tweezers mode I and off-state SW21. Activator A1 can invade this undesired complex, binding to the exposed 5-bases `TAATA` promoter domain, thereby displacing the tweezers.

Reaction Pathways

Closing:	$\mathrm{TwI} + \mathrm{dI1} \rightharpoonup \mathrm{TwI} \cdot \mathrm{dI1}$
Opening:	$\mathrm{TwI} \cdot \mathrm{dI1} + \mathrm{rA1} \rightharpoonup \mathrm{dI1} \cdot \mathrm{rA1} + \mathrm{TwI}$

Unmodeled Reactions

Interfering:	$\mathrm{TwI} + \mathrm{T21} \rightharpoonup \mathrm{TwI} \cdot \mathrm{T21}$
Recovering:	$\mathrm{TwI} \cdot \mathrm{T21} + \mathrm{dI1} \rightharpoonup \mathrm{T21} + \mathrm{TwI} \cdot \mathrm{dI1}$
Recapturing:	$\mathrm{TwI} \cdot \mathrm{T21} + \mathrm{A1} \rightharpoonup \mathrm{TwI} + \mathrm{T21} \cdot \mathrm{A1}$
Double binding:	$\mathrm{TwI} + \mathrm{dI1} + \mathrm{dI1} \rightharpoonup \mathrm{TwI} \cdot \mathrm{dI1} \cdot \mathrm{dI1}$
Clearing:	$\mathrm{TwI} \cdot \mathrm{dI1} \cdot \mathrm{dI1} + \mathrm{rA1} + \mathrm{rA1} \rightharpoonup \mathrm{dI1} \cdot \mathrm{rA1} + \mathrm{dI1} \cdot \mathrm{rA1} + \mathrm{TwI}$

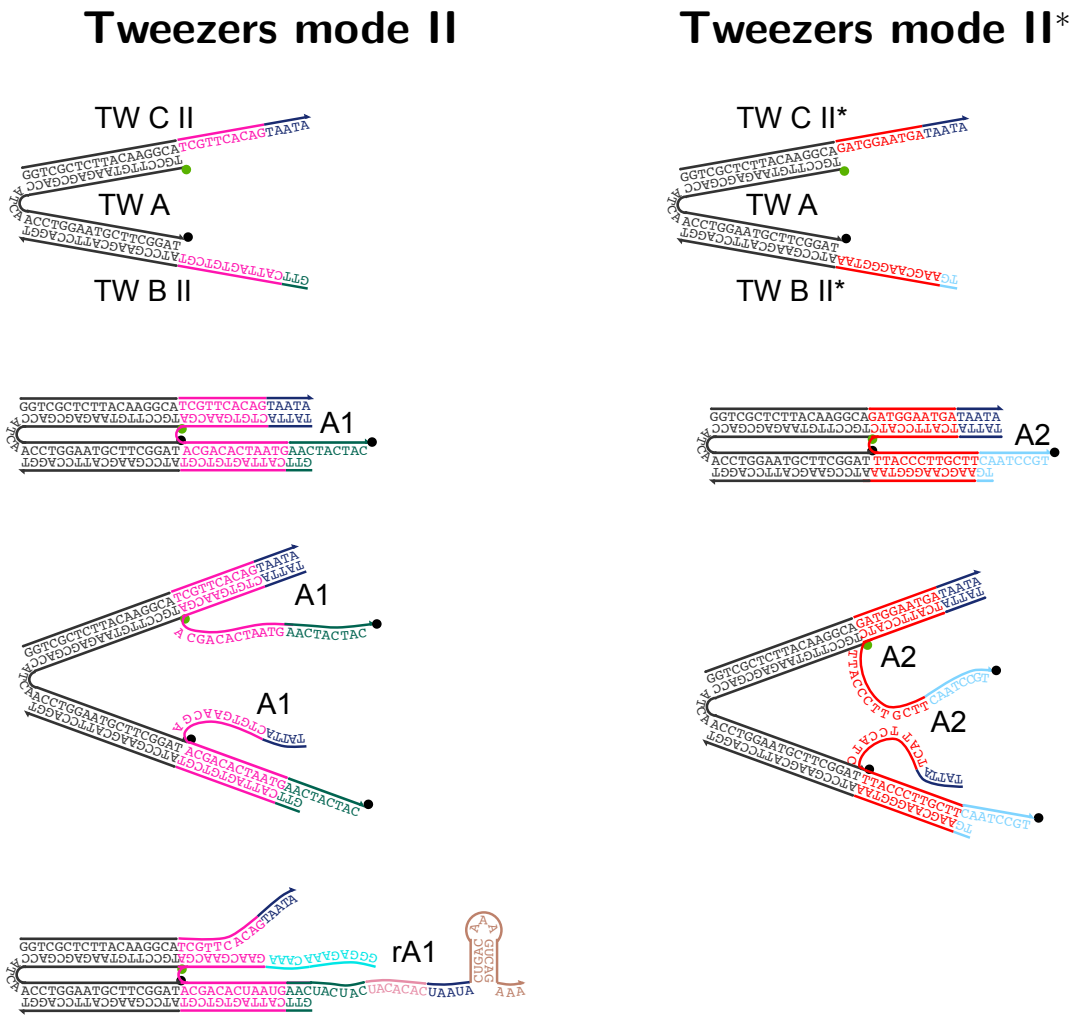

Figure S4: Relevant interactions for tweezers mode II. Left: mode II, with A1 input. Right: mode II*, with A2 input. Left, top to bottom: open tweezers; target A1 closing the tweezers; unwanted interaction with rA1. The latter complex is a substrate for RNase H, and there is a 9 bases toehold for displacement of the tweezers by A1. Right, top to bottom: open tweezers; target A2 closing the tweezers.

	Reaction Pathways	**Reaction Pathway Examples**
	Tweezers mode II	Tweezers mode II*
Closing:	$\mathrm{TwII} + \mathrm{A1} \rightharpoonup \mathrm{TwII} \cdot \mathrm{A1}$	$\mathrm{TwII^*} + \mathrm{A2} \rightharpoonup \mathrm{TwII^*} \cdot \mathrm{A2}$
Opening:	$\mathrm{TwII} \cdot \mathrm{A1} + \mathrm{dI1} \rightharpoonup \mathrm{TwII} + \mathrm{A1} \cdot \mathrm{dI1}$	$\mathrm{TwII^*} \cdot \mathrm{A2} + \mathrm{rI2} \rightharpoonup \mathrm{TwII^*} + \mathrm{A2} \cdot \mathrm{rI2}$

	Unmodeled Reactions
	Tweezers mode II
Interfering:	$\mathrm{TwII} + \mathrm{rA1} \rightharpoonup \mathrm{TwII} \cdot \mathrm{rA1}$
	$\mathrm{TwII} + \mathrm{rA1} + \mathrm{rA1} \rightharpoonup \mathrm{TwII} \cdot \mathrm{rA1} \cdot \mathrm{rA1}$
Recapturing:	$\mathrm{TwII} \cdot \mathrm{rA1} + \mathrm{dI1} \rightharpoonup \mathrm{TwII} + \mathrm{dI1} \cdot \mathrm{rA1}$
Recovering:	$\mathrm{TwII} \cdot \mathrm{rA1} + \mathrm{A1} \rightharpoonup \mathrm{TwII} \cdot \mathrm{A1} + \mathrm{rA1}$
Degradation:	$\mathrm{TwII} \cdot \mathrm{rA1} + \mathrm{RNaseH} \rightleftharpoons \mathrm{TwII} \cdot \mathrm{rA1} \cdot \mathrm{RNaseH} \rightharpoonup \mathrm{TwII} + \mathrm{RNaseH}$
	$\mathrm{TwII} \cdot \mathrm{rA1} \cdot \mathrm{rA1} + \mathrm{RNaseH} \rightleftharpoons \mathrm{TwII} \cdot \mathrm{rA1} \cdot \mathrm{rA1} \cdot \mathrm{RNaseH} \rightharpoonup \mathrm{TwII} + \mathrm{RNaseH}$
Double binding:	$\mathrm{TwII} + \mathrm{A1} + \mathrm{A1} \rightharpoonup \mathrm{TwII} \cdot \mathrm{A1} \cdot \mathrm{A1}$
Clearing:	$\mathrm{TwII} \cdot \mathrm{A1} \cdot \mathrm{A1} + \mathrm{dI1} + \mathrm{dI1} \rightharpoonup \mathrm{dI1} \cdot \mathrm{A1} + \mathrm{dI1} \cdot \mathrm{A1} + \mathrm{TwII}$

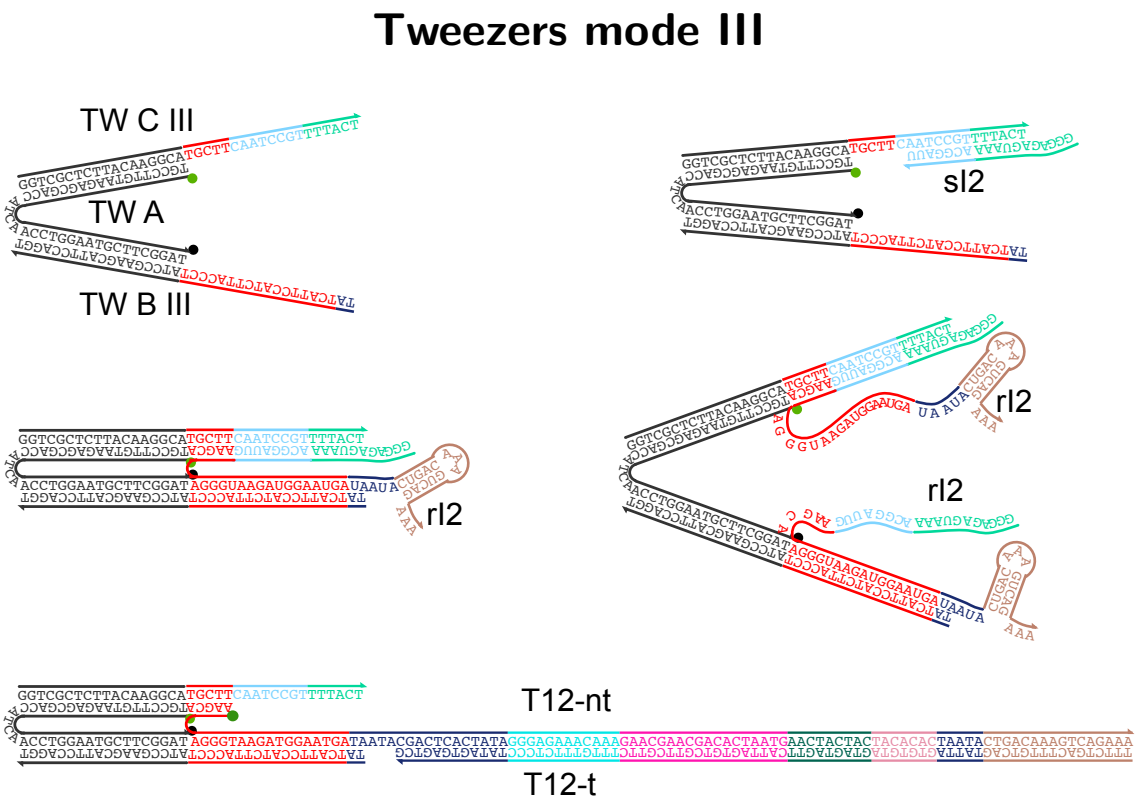

Figure S5: Relevant interactions for tweezers mode III. From top to bottom: open tweezers and incomplete RNase H degradation product sI2 binding to the Tweezers; RNA target rI2 closing the tweezers; undesired complex TwIII·T12. The unwanted complex has a 14-bases exposed toehold that can be targeted by rI2.

Reaction Pathway Examples	
Closing:	$\mathrm{TwIII} + \mathrm{rI2} \rightharpoonup \mathrm{TwIII} \cdot \mathrm{rI2}$
Double binding:	$\mathrm{TwIII} + \mathrm{rI2} + \mathrm{rI2} \rightharpoonup \mathrm{TwIII} \cdot \mathrm{rI2} \cdot \mathrm{rI2}$
Opening/Degradation:	$\mathrm{TwIII} \cdot \mathrm{rI2} + \mathrm{RNaseH} \rightleftharpoons \mathrm{TwIII} \cdot \mathrm{rI2} \cdot \mathrm{RNaseH} \rightharpoonup \mathrm{TwIII} + \mathrm{RNaseH}$
	$\mathrm{TwIII} \cdot \mathrm{rI2} \cdot \mathrm{rI2} + \mathrm{RNaseH} \rightleftharpoons \mathrm{TwIII} \cdot \mathrm{rI2} \cdot \mathrm{rI2} \cdot \mathrm{RNaseH} \rightharpoonup \mathrm{TwIII} + \mathrm{RNaseH}$
Opening/Branch migration:	$\mathrm{TwIII} \cdot \mathrm{rI2} \cdot \mathrm{rI2} + \mathrm{A2} \rightharpoonup \mathrm{TwIII} \cdot \mathrm{rI2} + \mathrm{A2} \cdot \mathrm{rI2}$
Interfering:	$\mathrm{TwIII} + \mathrm{T12} \rightharpoonup \mathrm{TwIII} \cdot \mathrm{T12}$
Recapturing:	$\mathrm{TwIII} \cdot \mathrm{T12} + \mathrm{rI2} \rightharpoonup \mathrm{TwIII} \cdot \mathrm{T12} \cdot \mathrm{rI2}$
Recovering:	$\mathrm{TwIII} \cdot \mathrm{T12} + \mathrm{A2} \rightharpoonup \mathrm{TwIII} + \mathrm{T12} \cdot \mathrm{A2}$

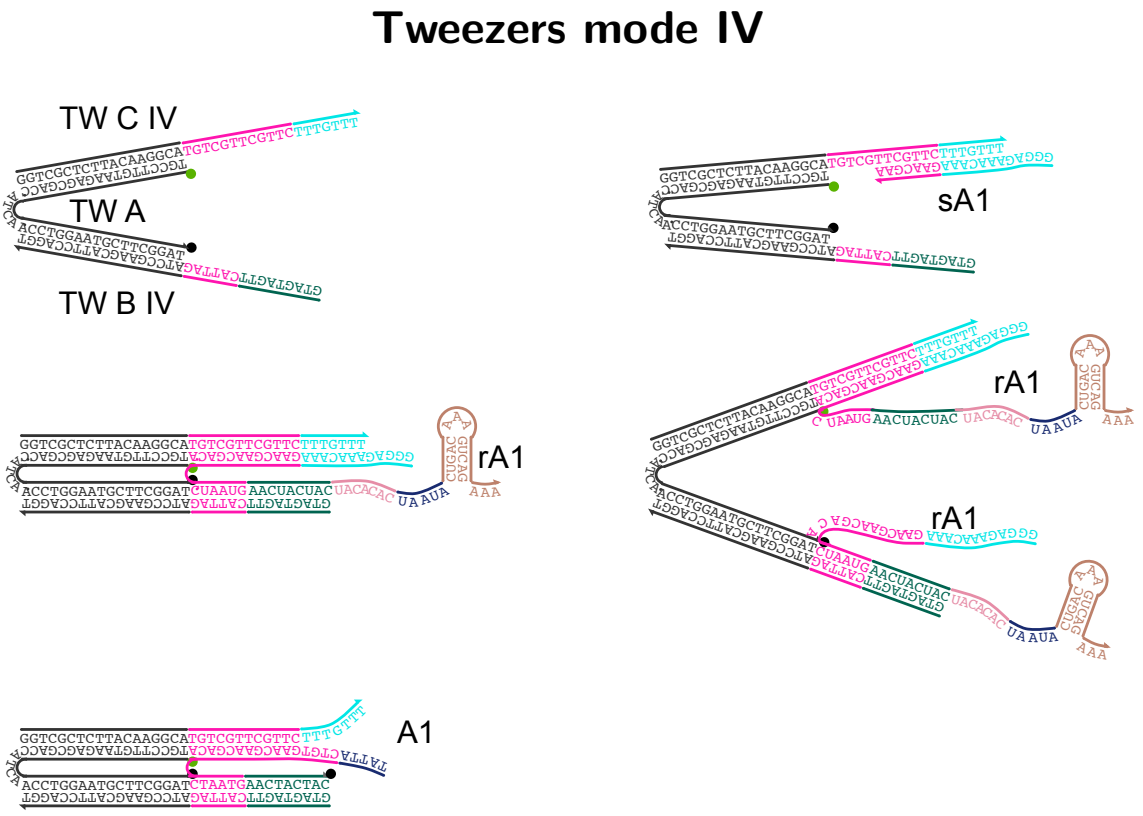

Figure S6: Relevant interactions for tweezers mode IV. From top to bottom: open tweezers and incomplete RNase H degradation product sA1 binding to the tweezers; RNA target rA1 closing the tweezers (this complex can be opened either by RNase H degradation or toehold mediated strand migration by dI1, on the 7-bases exposed light pink domain of rA1); undesired interaction with DNA species A1. The desired target complex TwIV·rA1 shares 7 more bases than the undesired complex TwIV· A1.

Reaction Pathway Examples	
Closing:	$\mathrm{TwIV} + \mathrm{rA1} \rightharpoonup \mathrm{TwIV} \cdot \mathrm{rA1}$
Double binding:	$\mathrm{TwIV} + \mathrm{rA1} + \mathrm{rA1} \rightharpoonup \mathrm{TwIV} \cdot \mathrm{rA1} \cdot \mathrm{rA1}$
Opening:	$\mathrm{TwIV} \cdot \mathrm{rA1} + \mathrm{dI1} \rightharpoonup \mathrm{rA1} \cdot \mathrm{dI1} + \mathrm{TwIV}$
Clearing:	$\mathrm{TwIV} \cdot \mathrm{rA1} \cdot \mathrm{rA1} + \mathrm{dI1} + \mathrm{dI1} \rightharpoonup \mathrm{rA1} \cdot \mathrm{dI1} + \mathrm{rA1} \cdot \mathrm{dI1} + \mathrm{TwIV}$
	$\mathrm{TwIV} \cdot \mathrm{A1} + \mathrm{dI1} \rightharpoonup \mathrm{TwIV} + \mathrm{dI1} \cdot \mathrm{A1}$
Degradation:	$\mathrm{TwIV} \cdot \mathrm{rA1} + \mathrm{RNaseH} \rightleftharpoons \mathrm{TwIV} \cdot \mathrm{rA1} \cdot \mathrm{RNaseH} \rightharpoonup \mathrm{TwIV} + \mathrm{RNaseH}$
	$\mathrm{TwIV} \cdot \mathrm{rA1} \cdot \mathrm{rA1} + \mathrm{RNaseH} \rightleftharpoons \mathrm{TwIV} \cdot \mathrm{rA1} \cdot \mathrm{rA1} \cdot \mathrm{RNaseH} \rightharpoonup \mathrm{TwIV} + \mathrm{RNaseH}$
Interfering:	$\mathrm{TwIV} + \mathrm{A1} \rightharpoonup \mathrm{TwIV} \cdot \mathrm{A1}$
Recovering:	$\mathrm{TwIV} \cdot \mathrm{A1} + \mathrm{rA1} \rightharpoonup \mathrm{TwIV} \cdot \mathrm{rA1} + \mathrm{A1}$

mode V* - Insulator A1

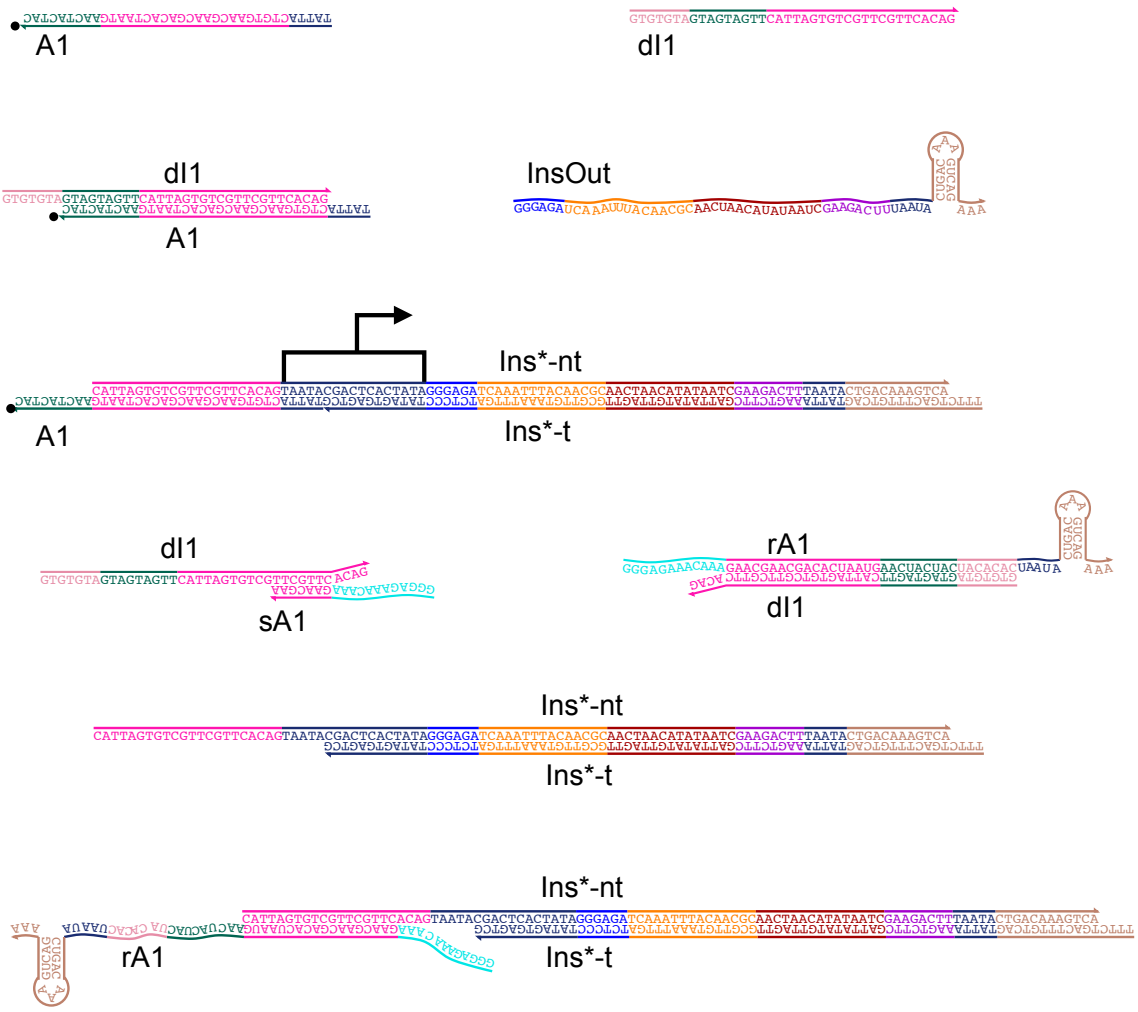

Figure S7: Relevant interactions for the mode V* insulator, with input A1. This insulator switch has the same input domain of SW21, and therefore the same complexes and side reactions as in Figure S2 are represented. The output of the insulator is denoted as InsOut.

Reaction Pathway Examples

Activation:	$A1 + Ins^* \rightharpoonup Ins^* \cdot A1$
Inhibition:	$dI1 + Ins^* \cdot A1 \rightharpoonup dI1 \cdot A1 + Ins^*$
Release:	$rA1 + dI1 \cdot A1 \rightharpoonup rA1 \cdot dI1 + A1$
Annihilation:	$dI1 + A1 \rightharpoonup dI1 \cdot A1$
	$rA1 + dI1 \rightharpoonup rA1 \cdot dI1$
Transcription:	$Ins^* \cdot A1 + RNAP \rightleftharpoons Ins^* \cdot A1 \cdot RNAP \rightharpoonup InsOut + Ins^* \cdot A1 + RNAP$
	$Ins^* + RNAP \rightleftharpoons Ins^* \cdot RNAP \rightharpoonup InsOut + Ins^* + RNAP$
Degradation:	$rA1 \cdot dI1 + RNaseH \rightleftharpoons rA1 \cdot dI1 \cdot RNaseH \rightharpoonup dI1 + RNaseH$
	$Ins^* \cdot rA1 + RNaseH \rightleftharpoons Ins^* \cdot rA1 \cdot RNaseH \rightharpoonup Ins^* + RNaseH$
Interfering:	$rA1 + Ins^* \rightharpoonup Ins^* \cdot rA1$
Recapturing:	$dI1 + Ins^* \cdot rA1 \rightharpoonup rA1 \cdot dI1 + Ins^*$
Recovering:	$A1 + Ins^* \cdot rA1 \rightharpoonup Ins^* \cdot A1 + rA1$

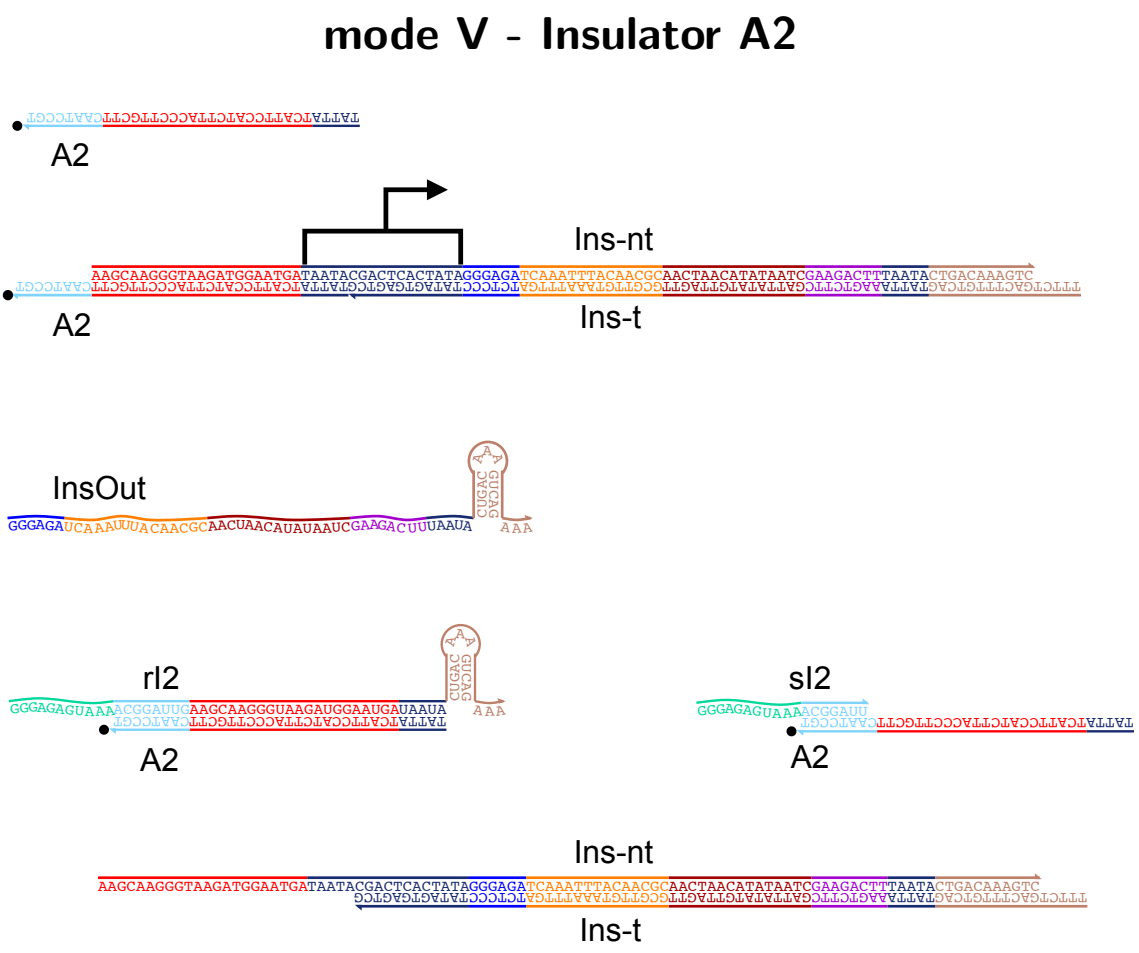

Figure S8: Relevant interactions for the mode V insulator, with input A2. This insulator switch has the same input domain of SW12, and therefore the same complexes as in Figure S1 are represented. The output of the insulator is denoted as InsOut, and is the same as in the insulator having input A1, shown in Figure S7.

Reaction Pathways	
Activation:	$A2 + Ins \rightharpoonup Ins \cdot A2$
Inhibition:	$rI2 + Ins \cdot A2 \rightharpoonup rI2 \cdot A2 + Ins$
Annihilation:	$rI2 + A2 \rightharpoonup rI2 \cdot A2$
Transcription:	$Ins \cdot A2 + RNAP \rightleftharpoons Ins \cdot A2 \cdot RNAP \rightharpoonup InsOut + Ins \cdot A2 + RNAP$
	$Ins + RNAP \rightleftharpoons Ins \cdot RNAP \rightharpoonup InsOut + Ins + RNAP$
Degradation:	$rI2 \cdot A2 + RNaseH \rightleftharpoons rI2 \cdot A2 \cdot RNaseH \rightharpoonup sI2 \cdot A2 + RNaseH$

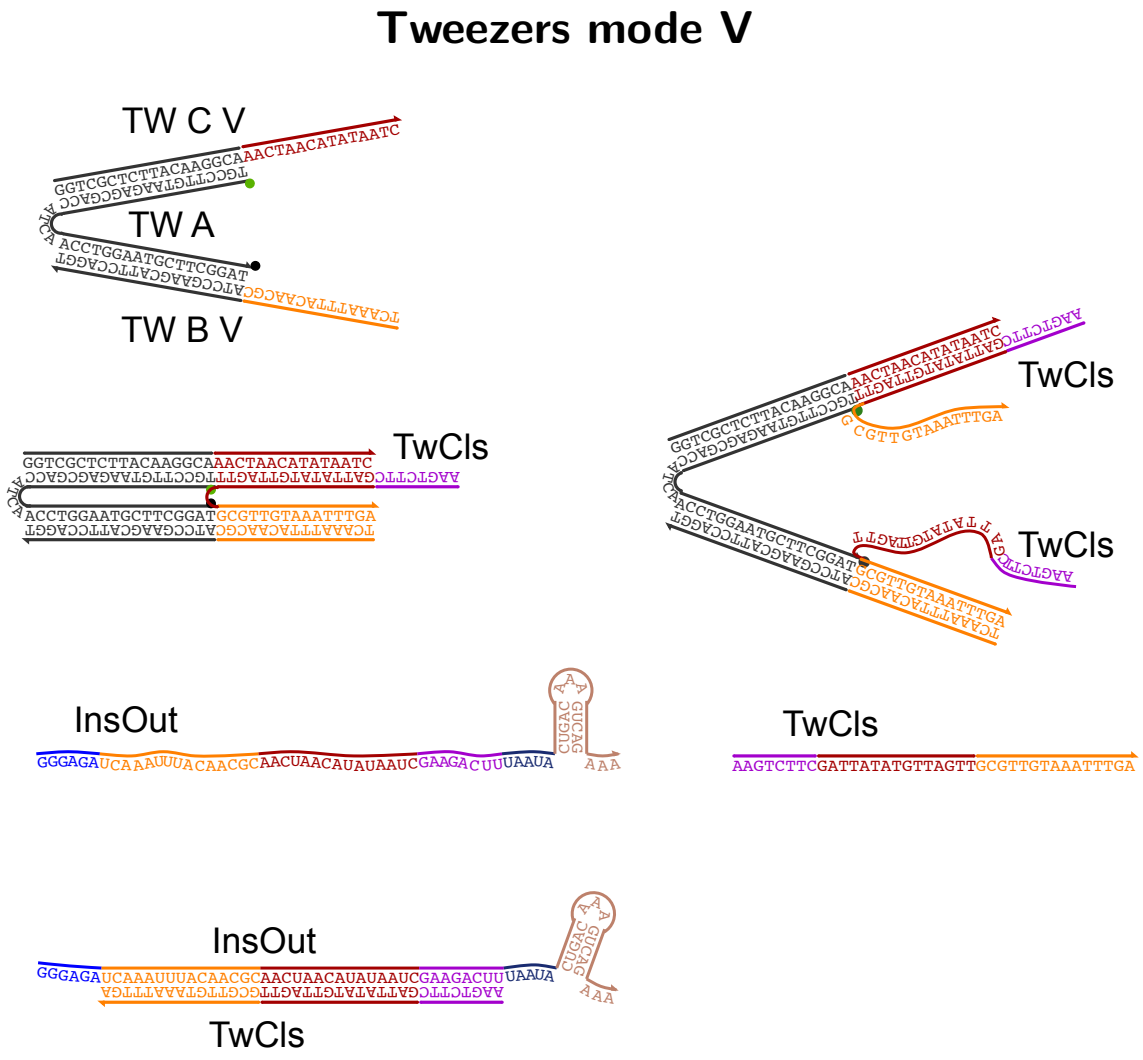

Figure S9: Relevant interactions for the load stage of tweezers mode V. From top to bottom, left to right: Tweezers mode V, open; Tweezers mode V closed by their target TwCls; Tweezers mode V bound to two target molecules TwCls; RNA strand InsOut (output of the insulators in Figures S7 and S8); DNA strand TwCls; TwCls displaced by InsOut.

Reaction Pathways

Closing:	$\mathrm{TwV} + \mathrm{TwCls} \rightharpoonup \mathrm{TwV} \cdot \mathrm{TwCls}$
Opening:	$\mathrm{TwV} \cdot \mathrm{TwCls} + \mathrm{InsOut} \rightharpoonup \mathrm{TwCls} \cdot \mathrm{InsOut} + \mathrm{TwV}$
Annihilation:	$\mathrm{TwCls} + \mathrm{InsOut} \rightharpoonup \mathrm{TwCls} \cdot \mathrm{InsOut}$
Degradation:	$\mathrm{TwCls} \cdot \mathrm{InsOut} + \mathrm{RNaseH} \rightleftharpoons \mathrm{TwCls} \cdot \mathrm{InsOut} \cdot \mathrm{RNaseH} \rightharpoonup \mathrm{TwCls} + \mathrm{RNaseH}$

Unmodeled Reactions

Double binding:	$\mathrm{TwV} + \mathrm{TwCls} + \mathrm{TwCls} \rightharpoonup \mathrm{TwV} \cdot \mathrm{TwCls} \cdot \mathrm{TwCls}$
Clearing:	$\mathrm{TwV} \cdot \mathrm{TwCls} \cdot \mathrm{TwCls} + \mathrm{InsOut} + \mathrm{InsOut} \rightharpoonup \mathrm{TwV} + \mathrm{TwCls} \cdot \mathrm{InsOut} + \mathrm{TwCls} \cdot \mathrm{InsOut}$

Malachite green switch

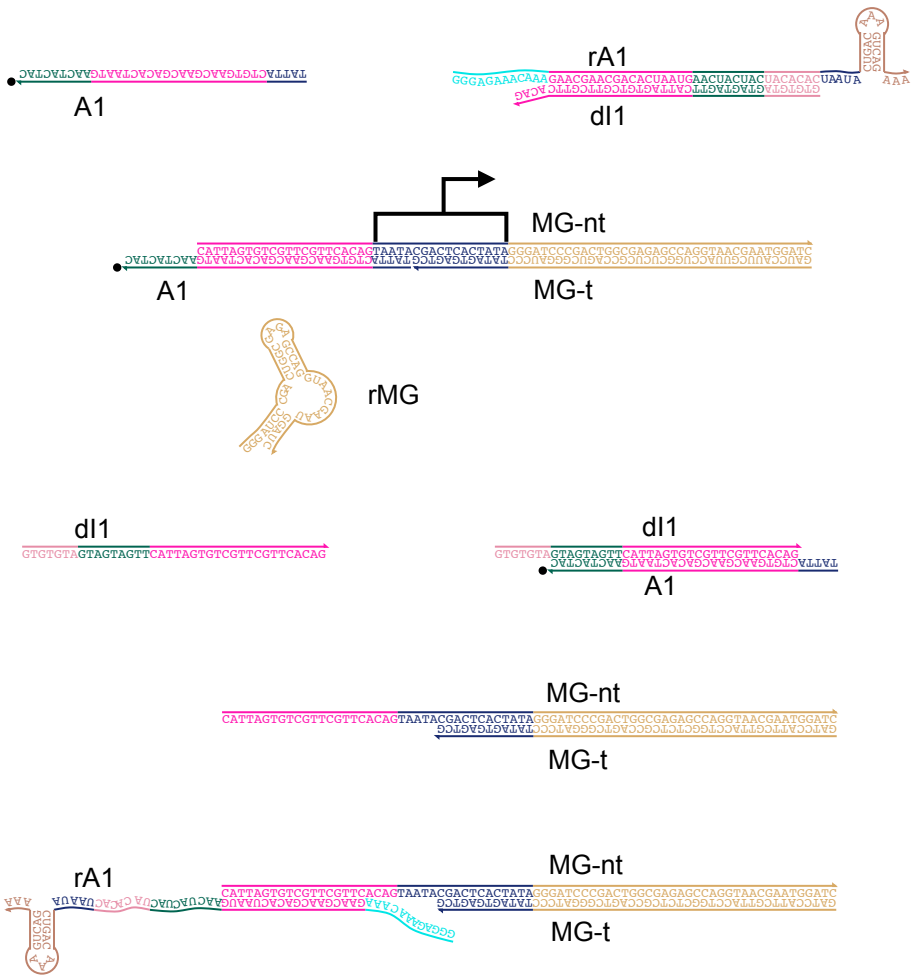

Figure S10: Relevant interactions for the TMG1 switch. This switch has the same input domain of SW21, and therefore the same activation/inhibition and unwanted interaction complexes as in Figure S2 are represented. The output of the switch is the MG aptamer RNA.

Reaction Pathways	
Activation:	$\mathrm{A1} + \mathrm{TMG1} \rightharpoonup \mathrm{TMG1 \cdot A1}$
Inhibition:	$\mathrm{dI1} + \mathrm{TMG1 \cdot A1} \rightharpoonup \mathrm{dI1 \cdot A1} + \mathrm{TMG1}$
Release:	$\mathrm{rA1} + \mathrm{dI1 \cdot A1} \rightharpoonup \mathrm{rA1 \cdot dI1} + \mathrm{A1}$
Annihilation:	$\mathrm{dI1} + \mathrm{A1} \rightharpoonup \mathrm{dI1 \cdot A1}$
	$\mathrm{rA1} + \mathrm{dI1} \rightharpoonup \mathrm{rA1 \cdot dI1}$
Transcription:	$\mathrm{TMG1 \cdot A1} + \mathrm{RNAP} \rightleftharpoons \mathrm{TMG1 \cdot A1 \cdot RNAP} \rightharpoonup \mathrm{rMG} + \mathrm{TMG1 \cdot A1} + \mathrm{RNAP}$
	$\mathrm{TMG1} + \mathrm{RNAP} \rightleftharpoons \mathrm{TMG1 \cdot RNAP} \rightharpoonup \mathrm{rMG} + \mathrm{TMG1} + \mathrm{RNAP}$
Degradation:	$\mathrm{rA1 \cdot dI1} + \mathrm{RNaseH} \rightleftharpoons \mathrm{rA1 \cdot dI1 \cdot RNaseH} \rightharpoonup \mathrm{dI1} + \mathrm{RNaseH}$

Unmodeled Reactions	
Interfering:	$\mathrm{rA1} + \mathrm{TMG1} \rightharpoonup \mathrm{TMG1 \cdot rA1}$
Recapturing:	$\mathrm{dI1} + \mathrm{TMG1 \cdot rA1} \rightharpoonup \mathrm{rA1 \cdot dI1} + \mathrm{TMG1}$
Recovering:	$\mathrm{A1} + \mathrm{TMG1 \cdot rA1} \rightharpoonup \mathrm{A1 \cdot TMG1} + \mathrm{rA1}$
Degradation:	$\mathrm{TMG1 \cdot rA1} + \mathrm{RNaseH} \rightleftharpoons \mathrm{TMG1 \cdot rA1 \cdot RNaseH} \rightharpoonup \mathrm{TMG1} + \mathrm{RNaseH}$

3 Sample Notation

In this supplementary information, several data sets are presented. Within each set, identical DNA stock solutions and enzyme batches are used. Sets A, B, 1, 2, 3 were recorded at Technical University in Munich (TUM); sets 4, 5 and 6 were recorded at Caltech. For more details about sample preparation please refer to Section 4. Each data set consists of several rounds of data acquisition with four samples each. One sample from each round usually is a reference sample containing the oscillator system only, unless otherwise noted. Data acquisition of one round takes one day; for the data recorded at TUM, a specific data set consists of measurements taken several days in a row using the same enzyme pre-mix (as specified in Table S1). We will use the notation TWI-1 (for example) to indicate the mode I tweezers experiments of set 1.

The data presented in the main paper are from data sets 3 and 4 exclusively. Data variability across different samples, rounds of data acquisition and data set are discussed in Sections 11, 12 and 13.

Table S1: Data sets acquisition overview: TUM

SET	**Day 1**	**Day 2**	**Day 3**	**Day 4**	**Day 5**	**Day 6**
A	sample-to-sample (sts-A)					
B	sample-to-sample (sts-B)					
1	sample-to-sample (sts-1)	MG aptamer (MG-1)	tweezers I (TWI-1)	tweezers II (TWII-1)	tweezers III (TWIII-1)	test sample (TS-1)
2	tweezers I (TWI-2)	tweezers II (TWII-2)		MG aptamer (MG-2)		
3	test sample (TS-3)	tweezers I (TWI-3)	tweezers III (TWIII-3)	MG aptamer (MG-3)	tweezers II (TWII-3)	

Table S2: Data sets acquisition overview: Caltech

SET	**Modes:**				
4	tweezers I (TWI-4)	tweezers II (TWII-4)	tweezers III (TWIII-4)	tweezers IV (TWIV-4)	tweezers V (TWV-4)
5	threshold variation I	threshold variation II	threshold variation III		
6	tweezers II (TWII-6)	tweezers II* (TWII*-6)	tweezers V* (TWV*-6)	tweezers V (TWV-6)	

4 Sample Preparation

The protocols followed at TUM and Caltech are thoroughly described in this section. The transcription protocols differ mainly in the RNA polymerase (RNAP) and RNase H handling method, the concentration of ribonucleoside triphosphates (rNTPs) and the DNA activators and inhibitors thresholds.

Operating point

We defined our operating point for the oscillator as a trajectory providing 4-6 oscillations in 16 hours, with amplitude of 80–120 nM.

The dynamics of the core oscillator are a function of several variables: DNA concentrations, buffer composition, concentration and activity of RNAP and RNase H. Most of our experiments were done using the Ambion T7 Megashortscript kit, whose transcription buffer and enzyme mix composition are not disclosed; each production batch is slightly tuned by the vendor to maximize transcription speed. In general, the characteristics of all off-the-shelf enzymes may vary among stocks purchased from the same supplier at different times. Therefore, all else being equal, using enzymes (and transcription buffer) from different production batches may result in significantly different oscillation amplitude and frequency.

To achieve a consistent operating point for all our experiments, we tuned the enzyme volumes (and, in some cases, the buffer composition) when switching to a new enzyme stock. We also empirically found that the concentration of DNA thresholds (A1, A2 and dI1) influences the operating point of the system, as shown in Figure S47. Therefore, we adjusted the thresholds as part of our tuning procedure to reach the desired operating point.

TUM: Sets A, B, 1, 2, 3

The final concentrations of the oscillator DNA strands were: T12 (120 nM), T21 (250

nM), dI1 (700 nM), A1 (250 nM), A2 (500 nM). The T21, T12, TMG1 switch and the TW A, TW B, TW C strands for each tweezer mode were annealed separately in Ambion T7 Megashortscript kit (Cat. n. AM1354) transcription buffer at 0.8x the concentration suggested by the supplier. The strands were annealed by heating up to 95°C for several minutes and cooling the samples down to room temperature over several hours using a Thermomixer (Eppendorf).

For the reaction itself, the Ambion T7 Megashortscript kit transcription buffer was used at a 0.8x the concentration suggested; rNTPs were used at 1.5x the concentration suggested (final concentration of 11.3 mM instead of 7.5 mM each rNTP). The unknown $MgCl_2$ concentration in the transcription buffer was adjusted, by adding final 15 mM to balance the increased rNTP concentration.

To maintain constant enzyme ratios, T7 RNAP enzyme mix (Ambion Megashortscript Kit, Cat. n. AM1354) and RNase H (Ambion, *E. coli* cloned, Cat. n. AM2292, 10 U/μl) were premixed *once for each of the respective data sets.*

The annealed genelets, DNA thresholds and additional $MgCl_2$ were pre-mixed with buffer and rNTPs, once per each data set. At each round of fluorescence data acquisition, appropriate aliquots of such core-oscillator pre-mix were directly added to the quartz cuvettes. DNA tweezers, Malachite Green dye to a final concentration of 10 μM, TMG1 switch and nanopure water were also added in the desired amounts. The cuvettes were then placed in the Fluorolog 3 sample chamber at 37°C, allowing the system to equilibrate for 10-15 minutes. The enzyme mix was finally added in the appropriate volume to each sample, vigorously pipetting up and down to achieve a well-mixed solution. Samples were covered with hexadecane to prevent sample loss by evaporation. In control experiments, we observed a drift of MG fluorescence signal in the presence of hexadecane: therefore, the samples containing MG dye were sealed by a plug of lightly warmed parafilm instead of using hexadecane.

Caltech: Sets 4, 5

The final concentrations of the oscillator DNA strands were: T12 (120 nM), T21 (250 nM), dI1 (650 nM), A1 (300 nM), A2 (550 nM). T21, T12, insulator switches and the TW A, TW B, TW C strands for each tweezer mode were annealed separately in 1x Ambion Megashortscript kit buffer in a digital thermal cycler (MJ Mini 48Well Personal Thermal Cycler, Bio-Rad Laboratories, Inc.) by heating for 1 minute at 95°C and cooling to room temperature in 2 h.

A transcription buffer mix was prepared before each experiment run (for four samples) to a final concentration of 1x Transcription Buffer, 7.5 mM each rNTP (Ambion Megashortscript Kit, Cat. n. AM1354) and nanopure water as appropriate. The $MgCl_2$ concentration was not adjusted. To maintain constant enzyme ratios, T7 RNAP enzyme mix

(Ambion Megashortscript Kit, Cat. n. AM1354) and RNase H (Ambion, *E. coli* cloned, Cat. n. AM2292, 10 U/μl) were premixed once for each round of data acquisition (for four samples). The total enzyme pre-mix volume always exceeded by $\approx 10\%$ the volume required in the experiment.

Each experiment was carried out as follows. First, all DNA strands and all the transcription reagents were pre-mixed in two separate test tubes. The amount of each reagent is calculated to achieve the desired concentration in a final total 240 μl sample volume. The mixes were then split into the four quartz cuvettes of the data acquisition round, each with a final volume of 60 μl. The cuvettes were pre-warmed at 37°C in the Fluorolog 3 sample chamber. The transcription buffer mix was added first, followed by the DNA mix aliquot. We found that this procedure minimized the variability of fluorescence traces across samples in the same data acquisition round.

Each sample was sealed using 35 μl of hexadecane (MP Biomedicals, LLC, Cat. n.195218) to prevent evaporation. After measuring the initial off-state fluorescence for the switch T21 in the spectrofluorimeter, the enzyme mix was added to each sample in the appropriate volume (Table S3), through the sealing oil layer.

Caltech: Set 6

Final concentrations of the oscillator DNA strands were: T12 (120 nM), T21 (250 nM), dI1 (600 nM), A1 (250 nM), A2 (500 nM). The oscillator switches, insulators and the TW A, TW B, TW C strands for each tweezers mode were annealed separately in 1x transcription buffer (Epicentre Biotechnologies, Cat. n. BP1001), undergoing the same thermal treatment as sets 4 and 5.

The transcription buffer mix was prepared prior to each experiment run (for four samples), mixing reagents to the following final concentrations: 1x transcription buffer and 10 mM dithiothreitol (DTT), (Epicentre Biotechnologies, Cat. n. BP1001), 7.5 mM each rNTP (Epicentre Biotechnologies, Cat. n. RN02825), 35 mM $MgCl_2$ and 0.015 U/μl pyrophosphatase (Sigma Aldrich, Cat. n. I1891-100UN, resuspended in Tris HCl 20 mM, pH 7.2, 50% glycerol (v/v)).

T7 RNAP was purchased from Epicentre Biotechnologies, Cat. n. TM910K (200 U/μl). *E. coli* cloned RNase H was purchased from Ambion, Cat. n. AM2292 (10 U/μl).

Each step of the experiments done for set 6 followed closely the procedure described for sets 4 and 5.

Table S3: Overview of the enzyme volumes used in each data set and acquisition round. Measuring the concentration of RNAP and RNase H presents several challenges. For sets A, B and 1–5, we used the Ambion T7 enzyme mix provided with the T7 Megashortscript Kit; the vendor does not provide accurate information regarding the RNAP concentration or weight in each batch. According to Milburn et al. [U. S. Patent 5,256,555, 1993], the mix contains inorganic pyrophosphatase; therefore, absorbance measurements can only provide estimates of the RNAP concentration. In Sections 24-31, we used a nominal concentration $1.25\,\mu$M for RNAP, according to the absorbance measurements; we used a nominal concentration of $1.25\,\mu$M for RNase H, as quoted by the manufacturer. For set 6, we used Epicentre Biotechnology T7 RNAP: the concentration of the lot used in the experiments was 4 μM. See Section 33 for a list of estimated enzyme concentrations.

SET	$V^{sample}(\mu l)$	$V_{T7}(\mu l)$	$V_H(\mu l)$	$V^{tot}_{EnzMix}(\mu l)$	$V^{sample}_{EnzMix}(\mu l)$	V_{T7}/V_H
A	65	90	7.8	97.8	11	11.5
B	65	90	8.6	98.6	10	10.5
1	65	290	25.2	315.2	11	11.5
2	65	180	17.2	197.2	10	10.5
3	65	304	40	344	10	7.6
4	60	22	2.2	24.2	5.6	10.0
5	60	22	2.2	24.2	5.6	10.0
6	60	18	2	20	4	9.0

Table S4: Overview of the concentrations of DNA species used in each data set.

SETS	[T21] (nM)	[A1] (nM)	[dI1] (nM)	[T12] (nM)	[A2] (nM)
A, B, 1, 2, 3	250	250	700	120	500
4	250	300	650	120	550
5 (default)	250	300	600	120	500
6	250	250	600	120	500

5 Fluorescence Data Acquisition

The TUM and Caltech laboratories performed all fluorescence experiments on a Horiba/Jobin Yvon Fluorolog 3 system, using 45 μL sample chamber quartz cuvettes. Fluorescence emission of the dye/quencher pair labelled DNA strands was recorded every minute (data sets A, B, 1, 2 and 3) or every two minutes (data sets 4, 5 and 6). A sample temperature of 37°C was either maintained using a Peltier element (for single samples) or a water circulation thermostat (when a four-sample-changer was used).

6 Fluorescence Spectra

The emission and excitation spectra of the fluorophore–labeled DNA strands were recorded to check for fluorescence crosstalk. The core oscillator templates used for sets A, B, 1, 2, 3 were labeled with TAMRA on T12-nt and with Texas Red on T21-nt. For data sets 4, 5 and 6, TYE563-labeled T12-nt and TYE665-labeled T21-nt were used. Tweezers in all sets were labeled with Rhodamine Green.

TUM: Sets A, B, 1, 2 and 3

The excitation/emission maxima of Rhodamine Green are at 515 nm/540 nm, for TAMRA (T12) they are 557 nm/582 nm, for Texas Red (T21) 595 nm/610 nm, and for Malachite Green 630 nm/655 nm, respectively. For the spectra recordings, experimental buffer conditions were used. Concentration of the dye-carrying species T12 (TAMRA) and T21 (Texas Red) were 100 nM, 400 nM for the tweezers, 1 μM for aptamer-bound Malachite Green (with excess Malachite Green).

From the Rhodamine Green emission spectra (excitation at 515, 557, 595 and 630 nm), we conclude that Rhodamine Green does not interfere with the emission channels of the other dyes. Rhodamine Green is the only dye which is excited significantly at 515 nm, so we do not expect any crosstalk contribution to the Rhodamine Green emission channel either (spectra not shown).

When exciting at 557 nm, there is significant crosstalk between TAMRA and Texas Red. At identical concentrations (100 nM) of both dye-carrying species T12 (TAMRA) and T21 (Texas Red), the Texas Red signal is approximately 20% of the TAMRA signal. In the oscillator circuit, T21 (Texas Red) is used at a concentration more than two times the T12 (TAMRA) concentration (250 nM to 120 nM). Recording fluorescence emission from TAMRA at 582 nm, the Texas Red emission contributes roughly 30-40% of the signal. We therefore recorded TAMRA emission at 570 nm, where its intensity is still relatively high (70% of the emission maximum at 582 nm), and the relative contribution of Texas Red (at equal concentrations) is merely 6% instead of 20%. In the oscillator experiments (T12 120 nM, T21 250 nM), we therefore expect a contribution of approximately 10-15% of the Texas Red emission to the T12 channel. We decided not

to process the T12 channel raw data, as this contribution is not dominating the signal.

For excitation/emission at 595 nm/610 nm, there is no significant crosstalk between any of the dyes and this signal is regarded as exclusively coming from Texas Red emission. Consequently, the data was not corrected for crosstalk, either. For the MG channel (rMG, gene aptamer, at a concentration of 1000 nM, excitation/emission wave-lengths of 630 nm/655 nm), the contribution of Texas Red (T21, 100 nM) to the signal is negligible (1.7%). However, for observing rMG production at a low concentration, the Texas Red signal may initially dominate the signal.

Caltech: Sets 4, 5 and 6

There is a minimal crosstalk contribution between TYE563 and Rhodamine Green: the influence of full quenching of TYE563 (Rhodamine Green) induces a relative change in fluorescence on the Rhodamine Green (TYE563) channel not to exceed 5%. Therefore, crosstalk correction was not implemented. Excitation/emission for TYE563 (T12) was set to its maxima at 549 nm/ 563 nm, those for TYE665 (T21) at 645 nm/665 nm and Rhodamine Green (Tweezers) emission and excitation maxima were set at 504 nm/ 531 nm, according to the recommendation of the supplier IDT DNA.

The transcription reagents used in set 6 were purchased from Epicentre Biotechnology, instead of using the Ambion Megashortscript Kit, as detailed in Section 4. The spectra for this data set were therefore separately recorded for each fluorophore (TYE563, TYE665 and Rhodamine Green): the different buffer did not cause any significant alteration of the spectra, compared to Figure S13.

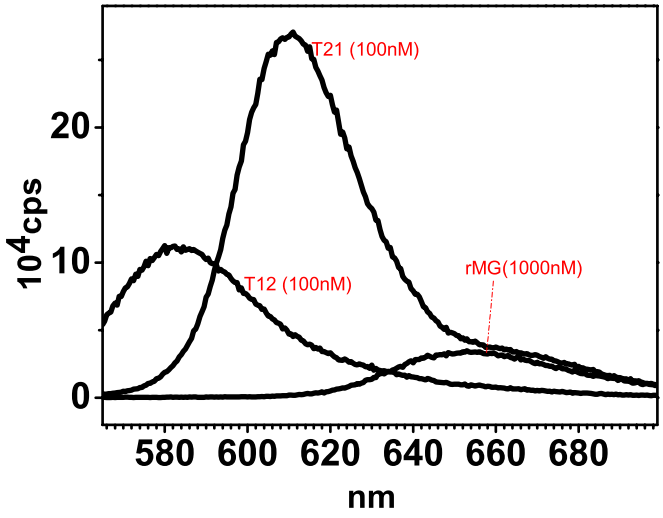

Figure S11: Excitation at 557 nm: Emission spectra of TAMRA (T12), Texas Red (T21) and Malachite Green bound to the MG aptamer (rMG). At the TAMRA emission maximum (582 nm) there is significant contribution of Texas Red to the signal. Therefore, the T12/TAMRA-emission signal was recorded at 570 nm with a smaller crosstalk contribution of Texas Red relative to the TAMRA signal intensity.

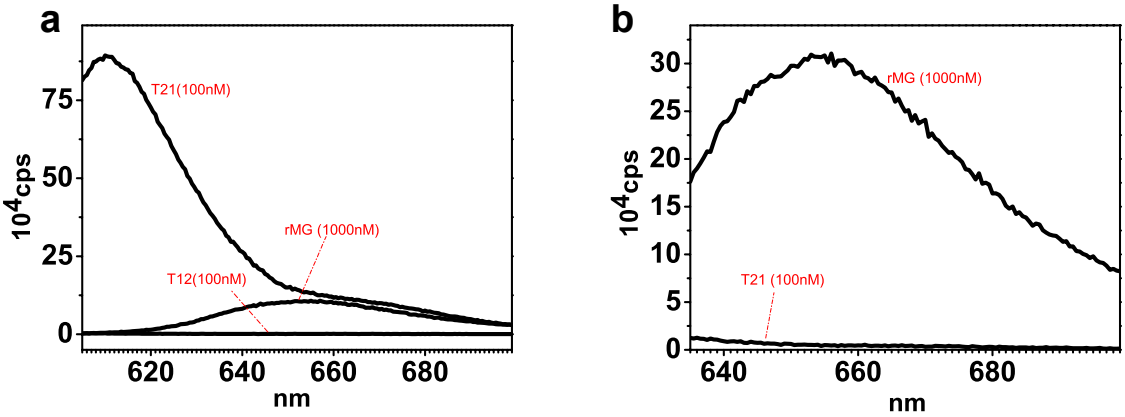

Figure S12: a. Excitation at 595 nm: Emission spectra of TAMRA (T12), Texas Red (T21) and Malachite Green bound to the aptamer (rMG). When recording at 610 nm, the T21/Texas Red channel is considered to be free from crosstalk.
b. Excitation at 630 nm: Emission spectra of Texas Red (T21) and Malachite Green-bound rMG. At high rMG concentrations, there is negligible contribution of Texas Red (T21) to the MG channel signal at 655 nm.

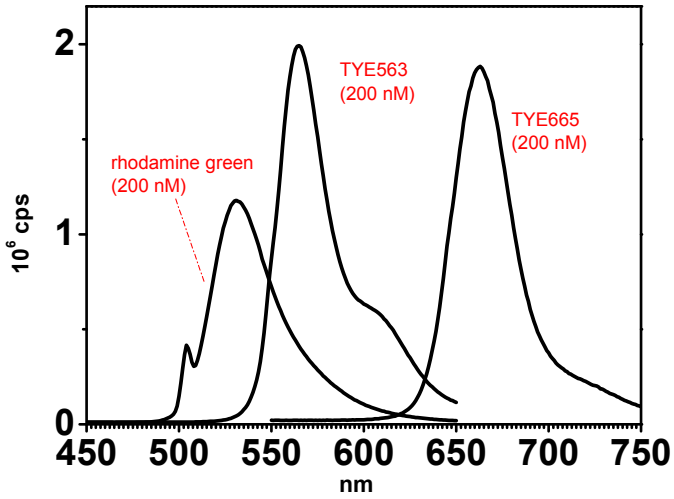

Figure S13: Emission spectra of TYE563 (T12), TYE665 (T21) and Rhodamine Green. Rhodamine Green emission was collected at 531 nm (excitation wavelength 504 nm), TYE563 at 563 nm (excitation at 549 nm) and TYE665 at 665 nm (excitation at 645 nm).

7 Crosstalk Correction

Figure S14a shows the raw data from set 1 MG aptamer production samples (MG-1). The black trace corresponds to the reference sample, while the others correspond to 50 nM (red), 100 nM (blue) and 150 nM load (green) samples. The reference sample contains no load (aptamer switch, in this case); hence, in this sample no aptamer is produced. As can be seen from the emission spectra shown in Section 6, the signal recorded in this case is entirely due to Texas Red crosstalk. This is also obvious from Figure S15a, where the MG channel signal (green trace, intensities in units of 10^4 cps) is directly compared to the Texas Red channel signal (red trace, intensities in units of 10^5 cps). Note that the ratio of the MG channel crosstalk signal to the Texas Red signal varies a little over time, from around 3% at the beginning to 4.3% at t≈1100 min.

Averaging the MG channel ($\mathrm{I}^{\mathrm{MG}}_{\mathrm{raw}}$) and Texas Red signal raw data ($\mathrm{I}^{\mathrm{TXR}}_{\mathrm{raw}}$) of the reference sample separately, gives a Texas Red emission of 2.99% in the MG channel compared to the Texas Red channel signal. Thus, the MG channel corrected data ($\mathrm{I}^{\mathrm{MG}}_{\mathrm{corr}}$) for each data point t_n is corrected from Texas Red emission crosstalk by:

$$\mathrm{I}^{\mathrm{MG}}_{\mathrm{corr}}\,(\mathrm{t}_n) = \mathrm{I}^{\mathrm{MG}}_{\mathrm{raw}}\,(\mathrm{t}_n) - 0.0299\;\mathrm{I}^{\mathrm{TXR}}_{\mathrm{raw}}\,(\mathrm{t}_n)$$

The corrected MG channel data, together with the Texas Red channel data for the reference sample is shown in Figure S15b. As can be seen, there is only negligible crosstalk left. Figure S14b displays the crosstalk corrected MG channel data for all four samples.

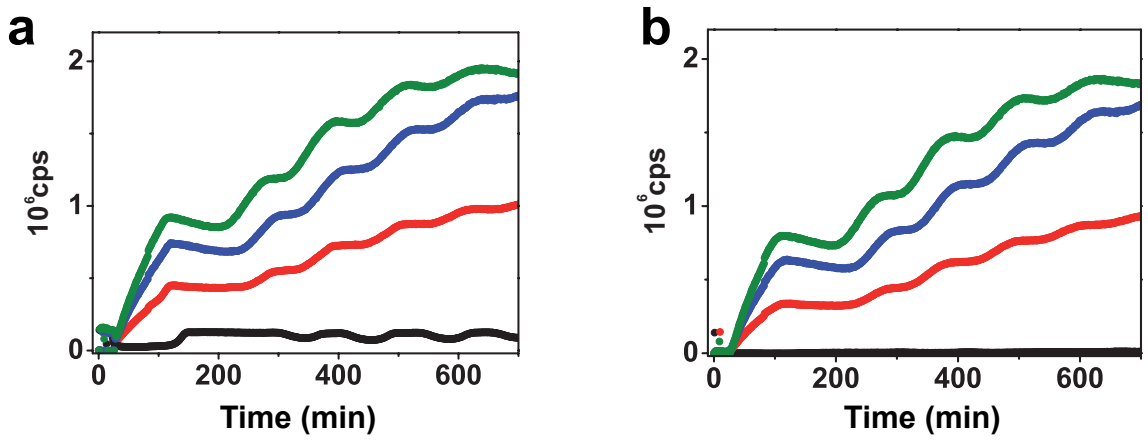

Figure S14: MG channel The MG-1 samples contain TMG1 genelet in different amounts. The reference sample is shown in black, 50 nM load in red, 100 nM load in blue and 150 nM load sample in green.
a. The reference sample does not contain any TMG1 switch: the signal recorded for that sample in the MG channel is solely due to Texas Red crosstalk emission. The order of magnitude of the crosstalk relative to the load fluorescence is relevant and requires correction.
b. Crosstalk-corrected MG channel data.

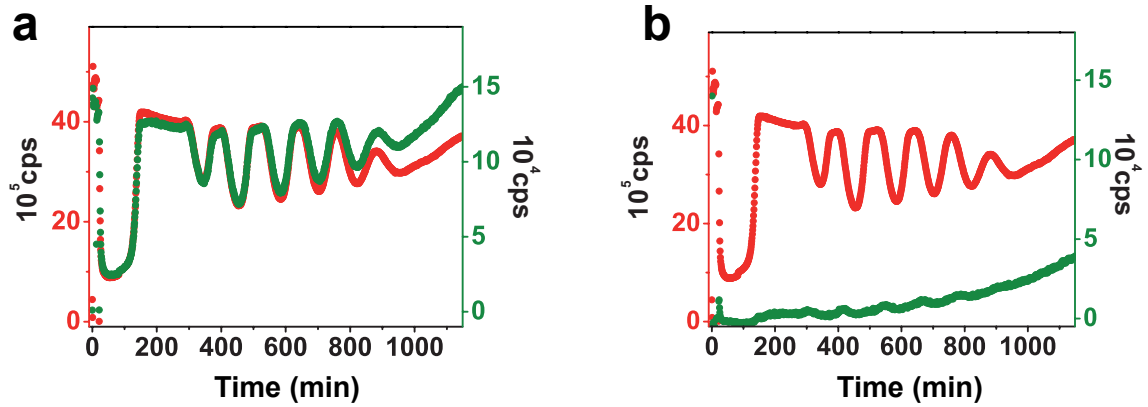

Figure S15: MG and Texas Red channels The MG-1 reference sample contains only the core oscillator, of which we measure the Texas Red labeled switch T21 fluorescence (red trace). This sample does not contain TMG1.
a. The signal detected in the MG channel (green trace) is purely due to crosstalk.
b. Crosstalk-corrected MG channel (green). The detected crosstalk T21 signal is negligible.

8 Fluorescence Data Processing

The raw fluorescence measurements recorded with the Horiba Fluorolog 3 were converted into molar concentrations according to the procedure described in this section. The ideal formula to convert each fluorescence trace to a concentration trace is:

$$C(t_n) = C_0 \frac{\mathrm{I}(t_n) - \mathrm{I}_{\min}}{\mathrm{I}_{\max} - \mathrm{I}_{\min}},$$

where C_0 is the nominal total concentration of the labeled DNA strand, $\mathrm{I}(t_n)$ is the raw fluorescence intensity measured by the instrument, and $\mathrm{I}_{\max}$, $\mathrm{I}_{\min}$ are the maximum and minimum fluorescence signals for the strand at that specific concentration and lamp intensity. In practice, $\mathrm{I}_{\max}$ is the signal that would be measured if all the tweezers (or switch) in the sample were in a fully open (or off) state; accordingly, $\mathrm{I}_{\min}$ corresponds to the signal measured in a fully closed tweezers/on state switch. Unfortunately, the values of $\mathrm{I}_{\max}$ and $\mathrm{I}_{\min}$ may not be both available for each trace. However, we can re–write the above formula as:

$$C(t_n) = C_0 \frac{\mathrm{I}(t_n)/\mathrm{I}_{\max} - \mathrm{r}}{1 - \mathrm{r}},$$

where $\mathrm{r} = \mathrm{I}_{\min}/\mathrm{I}_{\max}$. We were able to successfully use this formula because first, the minimum/maximum fluorescence signal ratio r should be independent of the specific strand concentrations and lamp intensity; therefore, we measured the r values off line. Second, we could determine $\mathrm{I}_{\max}$ for most of our experiments; in some cases, we could instead determine $\mathrm{I}_{\min}$, from which we could estimate $\mathrm{I}_{\max}$=$\mathrm{I}_{\min}/\mathrm{r}$.

To determine the r value, we first collected the average maximum fluorescence intensity $\mathrm{I}_{\max}$ from a calibration sample at known concentration, containing open tweezers (TWI–TWV) or genelet in the off state (T12 or T21). Then, we measured the average minimum quenched fluorescence $\mathrm{I}_{\min}$, by adding to the sample the tweezer closing strand (A1, dI1, A2, rI2, rA1 or TwCls) or activator (quencher-labeled) strand (A1 or A2) in excess. The on/off fluorescence ratio $\mathrm{r} = \mathrm{I}_{\min}/\ \mathrm{I}_{\max}$ was therefore calculated. As noted before, this ratio is independent of the instrument lamp intensity and of the concentration of labeled strands, provided that the closing strand is present in excess. However, we found that r is sensitive to the overall $MgCl_2$ and rNTPs concentration in the sample, in a sequence–dependent manner. In particular, we found that the closed state fluorescence of the tweezers is strongly affected by the overall ionic concentration in the sample. Specifically, the closed state fluorescence is lower in samples with higher $MgCl_2$ concentration. The buffer $MgCl_2$ concentration of the T7 Ambion Megashortscript Kit is unknown: this means that normalization measurements should be carried out with the same kit used for the experiments. This was not possible for the TUM data sets A, B, 1, 2 and 3. However, r's measured with three kits from different lots had at most a 10 $\%$ standard deviation. Therefore, for the TUM data, sets A, B, 1, 2 and 3, the r values were measured with a separate fresh Ambion kit. As an illustrative example, in Figure S17 we show the effects on the normalization of TW II-4 produced by normalization with a

50 $\%$ error in the determination of r. For the Caltech data, sets 4, 5 and 6, the r values were measured with the same transcription mix used for the time–course experiments. Table S5 shows the r and C_0 values used to normalize the different data sets.

The $\mathrm{I_{max}}$ value has to be determined as 'maximum off/open-state' fluorescence level of the monitored strands for each experiment. For the T21 genelet, the $\mathrm{I_{max}}$ value chosen for the TUM data was the averaged fluorescence value of the first large peak (which should correspond to a fully off-state of the switch). For the data recorded at Caltech, the initial T21 off-state fluorescence value prior to addition of enzymes was recorded for each trace. Therefore, $\mathrm{I_{max}}$ was calculated as the initial off-state fluorescence value, averaged across the four samples in the same data acquisition round, decreased by 10% to account for the dilution due to the subsequent addition of the enzyme mix to each sample. Regarding the determination of $\mathrm{I_{max}}$ for the T12 genelet, the data shown at Figure S19 were normalized by observing that the genelet is in a fully on state before adding enzymes; so we used such initial data to determine $\mathrm{I_{min}}$ as the on-state fluorescence, and estimated $\mathrm{I_{max}} = \mathrm{I_{min}}/r$.

For the molecular tweezers, the value of $\mathrm{I_{max}}$ was determined depending on the mode. For modes I and II, across all data sets, $\mathrm{I_{max}}$ was chosen to be the first peak of each trace. For modeII*, $\mathrm{I_{max}}$ was chosen as the maximum fluorescence value over the entire time trace (choosing $\mathrm{I_{min}}$ as the minimum over the trace prior to addition of enzymes, and then estimating $\mathrm{I_{max}} = \mathrm{I_{min}}/\mathrm{r}$ was not feasible, because 400 nM of tweezers may not be fully closed by the A2 amount in solution in case of pipetting inaccuracies). For modes III and IV, $\mathrm{I_{max}}$ was chosen as the high-fluorescence signal measured prior to addition of enzymes, when there is no RNA (closing strand) present in the system. For mode V, the value of $\mathrm{I_{max}}$ was taken as the fluorescence value measured prior to adding the closing strand for set 4; for modes V and V* in set 6, $\mathrm{I_{max}}$ was instead chosen as the fluorescence value of the first large peak of the traces at high amount of insulator (specifically, the traces shown at Figures S45, last row, second column, and Figure S44, last row, second column): such value of $\mathrm{I_{max}}$ was consistent across the data taken for modes V andV*. (Since all the data acquisition rounds for set 6 were recorded in subsequent days, without turning off the spectrofluorimeter, we assumed that lamp fluctuations could be neglected.)

Some of the samples were affected by evaporation (in particular, data set 1 and the mode MG experiments, where samples were not sealed with hexadecane): this caused a drift of the fluorescence traces over time, to values greater than the sample $\mathrm{I_{max}}$. The RNA–operated tweezers, modes III and V, also presented a similar drift, which was not caused by evaporation but presumably by the accumulation of short incomplete degradation products binding to the tweezers' hands. The experiments on mode V andV* tweezers instead presented a drift in the off-state minimum fluorescence, presumably caused by the depletion of rNTPs and by the consequently higher availability of free positive ions Mg^{++} in solution. These two effects produced normalized concentrations exceeding the

total strand amount in solution, or normalized concentrations becoming negative over time. The data affected by such fluorescence drifts were processed with a modified normalization protocol. First, we estimated the minimum fluorescence level for the trace as $\mathrm{I}_{\min} = \mathrm{r} \cdot \mathrm{I}_{\max}$. Then, at each data point we computed $a(t_n) = (\mathrm{I}(t_n) - \mathrm{I}_{\max})/t_n$ and $b(t_n) = (\mathrm{I}_{\min} - \mathrm{I}(t_n))/t_n$. We finally set $\bar{a}$=$\max\{a(t_n)\}$ and $\bar{b}$=$\max\{b(t_n)\}$ and normalized the data as follows:

$$\mathrm{I}_{\max}(t_n) := \mathrm{I}_{\max} + \bar{a} \cdot t_n, \quad \mathrm{I}_{\min}(t_n) := \mathrm{I}_{\min} - \bar{b} \cdot t_n$$
$$C(t_n) = \frac{\mathrm{I}(t_n) - \mathrm{I}_{\min}(t_n)}{\mathrm{I}_{\max}(t_n) - \mathrm{I}_{\min}(t_n)}.$$

This is equivalent to linearly correcting $\mathrm{I}_{\max}$ and $\mathrm{I}_{\min}$ with the minimal slope necessary to maintain all the data within the chosen concentration range. This correction was applied to the data shown in the following figures: Figure S39, set 1; Figure S40, set 1; Figure S42; Figure S43; Figure S44, all data sets; Figure S45, all data sets; Figure S46, sets 1 and 2.

Figure S16 shows the TWII-4 TYE665 channel fluorescence raw data (A), converted into T21 concentrations (B) as described above. The raw data and the corresponding concentrations for the Rhodamine Green channel, TWII-4, is shown in Figure S17, where we also highlight the effects of a 50% error in the estimation of r. Finally in Figure S18 we show the raw data for TWV-6, and the effects of the $\mathrm{I}_{\min}$ linear correction.

Table S5: Parameters for conversion of fluorescence intensities into concentrations

species	**r=** $\mathrm{I}_{\mathrm{MIN}}/\mathrm{I}_{\mathrm{MAX}}$	**C_0(nM)**
T12 (TAMRA)	0.11	120
T21 (Texas Red)	0.05	250
T12 (TYE563)	0.056 (sets 4, 5), 0.045 (set 6)	120
T21 (TYE665)	0.051 (sets 4, 5), 0.05 (set 6)	250
TWI	0.36 (sets A, B, 1, 2, 3); 0.31 (set 4)	50, 100, 150, 200, 400
TWII	0.28 (sets A, B, 1, 2, 3); 0.31 (set 4); 0.3 (set 6)	50, 100, 150, 200, 400
TWII*	0.45 (set 6)	50, 100, 150, 200, 400
TWIII	0.30 (sets A, B, 1, 2, 3); 0.35 (set 4)	50, 100, 150, 200, 400
TWIV	0.47	100, 200, 400
TWV	0.49 (set 4), 0.5 (set 6)	100, 200, 400, 600, 800

To determine the rMG concentration, we used the ratio of intensities of the dyes in their respective channel. From the spectra measurements we know:

$$\frac{\mathrm{I}^{\mathrm{TXR}}_{\mathrm{610nm}}}{\mathrm{I}^{\mathrm{MG}}_{\mathrm{655nm}}} = a\frac{[\mathrm{T21}]}{[\mathrm{rMG}]}.$$

The experimental values give: $a = \frac{26.7\times10^4\times1000}{30.8\times10^4\times100} = 8.7$. Therefore, the concentrations of rMG (given excess of MG dye) can be calculated by $[\mathrm{rMG}]{=}8.7\times250\mathrm{nM}\frac{\mathrm{I}^{MG}_{\mathrm{corr}}(t_n)}{\mathrm{I}^{\mathrm{TXR}}_{\mathrm{max}}}$ using the crosstalk corrected Malachite Green channel data ($\mathrm{I}^{\mathrm{MG}}_{\mathrm{corr}}(\mathrm{t_n})$) and the plateau level intensity of the Texas Red channel ($\mathrm{I}^{\mathrm{TXR}}_{\mathrm{max}}$) of each individual sample.

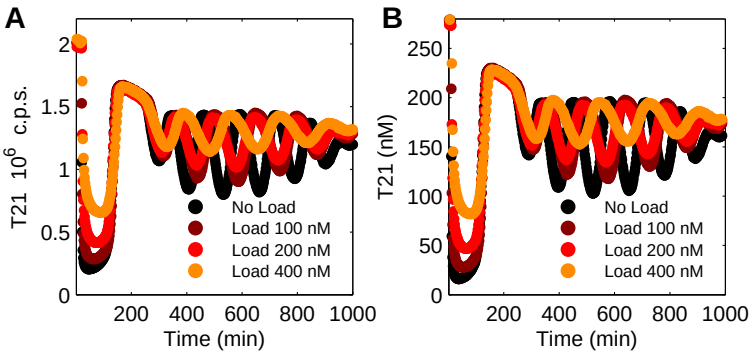

Figure S16: TWII-4 samples, T21 (TYE 665) channel.
A. Raw fluorescence data.
B. Fluorescence data converted to concentrations.

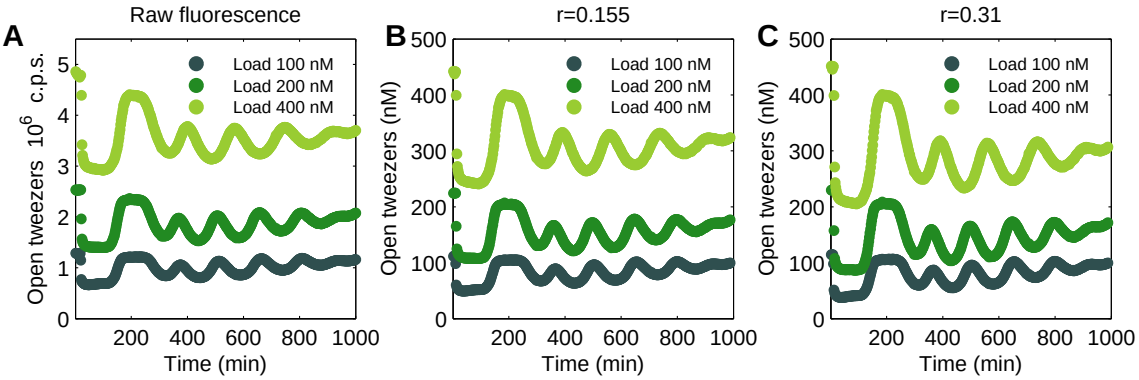

Figure S17: TWII-4 samples, TW II (Rhodamine Green) channel.
A. Raw fluorescence data.
B. Raw data converted to concentrations for TW II, with r=0.155, 50% lower than the correct value, r=0.31.
C. Raw data converted to concentrations for TW II, with r=0.31.

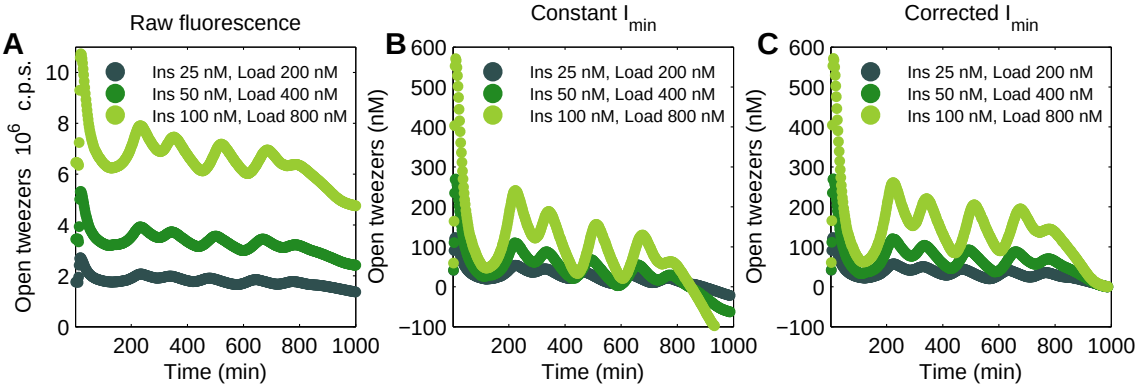

Figure S18: TWV-6 samples, TWV (Rhodamine Green) channel. These data corresponds to the data plotted in Figure S44, third row, second column.
A. Raw fluorescence data for TWV-6.
B. Raw data converted to concentrations for TWV-6, with constant I_{min}=r· I_{max}.
C. Raw data converted to concentrations for TWV-6, with linearly adjusted I_{min}.

9 T12-Channel Data

Throughout this paper, only the T21-channel data (Texas Red or TYE665) are used to characterize the behavior of the oscillator. The T12 fluorescence data (TAMRA or TYE563) were also monitored in each experiment, but their small amplitude does not allow us to derive significant information about the system behavior. (This is consistent with the findings in Kim and Winfree [2011].) In Figure S19a, as an example, we show both the T21 and T12 normalized traces from the TWII-4 sample. (The time-courses of T12 and T21 belonging to the same sample are shown in the same color.) However, only the T21-concentration shows strong oscillations; the T12-concentration oscillates only weakly around 100 nM. For this specific trajectory, the average concentrations are <T12> = 98 nM and <T21>= 163 nM. This gives <T12A2>≈(120 - 98) nM = 22 nM and <T21A1> ≈(250-163) = 87 nM. Across data sets 4 and 6, we found that <T12A2> is on average 20 nM, and <T21A1> is on average 75 nM. From gel electrophoresis data (see Figure S32) we also found that given equal amounts of on–templates, rA1 is produced in much higher amount than rI2. While the same promoter is used for both templates, the k_{cat} values for each switch might vary and be influenced by the flanking domains. T12 is only activated for a short time in each cycle, resulting in presumably small waves of rA1 production.

Looking at the phase portrait of the sample (Figure S19b), the concentration variation of T21/T21A1, Δ[T21]= Δ[T21A1] ≈ 100 nM is much larger than that of T12/T12A2 (Δ[T12]=Δ[T12A2] ≈ 10 nM). This demonstrates an asymmetry between the Switches 12 and 21: the state of SW21 is very sensitive to small changes in the state of SW12, while the state of SW12 does not respond analogously to variations in the state of SW21. Qualitatively, T12 exhibits the same behavior (small waves of modulation) in all samples

and is therefore omitted in the data presented.

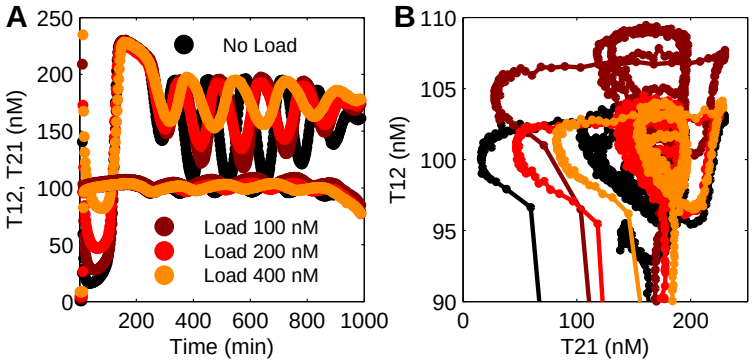

Figure S19: Trajectories of SW12 and SW21.
A. Time traces.
B. Phase portrait. The oscillation amplitude of SW12 is about one order of magnitude smaller than the amplitude of SW21. The traces of SW12 are therefore ignored in the analysis proposed in this paper.

10 Analysis of the oscillations

The period and amplitude of the oscillations are time-varying in most of the experiments. To be able to compare different oscillatory traces, we processed the data in order to consider only the first three full oscillations after the first large and irregular peak.

Period: We calculate the average oscillation period from the first three full oscillations, measured between the first and the fourth minimum.

$$T(n) = t_{\min}(n+1) - t_{\min}(n).$$

The mean period of each sample is defined by $< T >= (T(1)+T(2)+T(3))/3$, if there are at least three full oscillations, otherwise the number is reduced accordingly.

Amplitude: We measure the oscillation amplitude of oscillation cycle n as half the difference between the peaks as defined in Figure S20:

$$A(n) = (c_{\max}(n) - c_{\min}(n))/2.$$

The mean amplitude for each time trace is defined as $< A >= (A(1)+A(2)+A(3))/3$.

As an example, in Figure S20 we show how the peaks and wells were selected for the control sample of Tweezers mode II in data set 3.

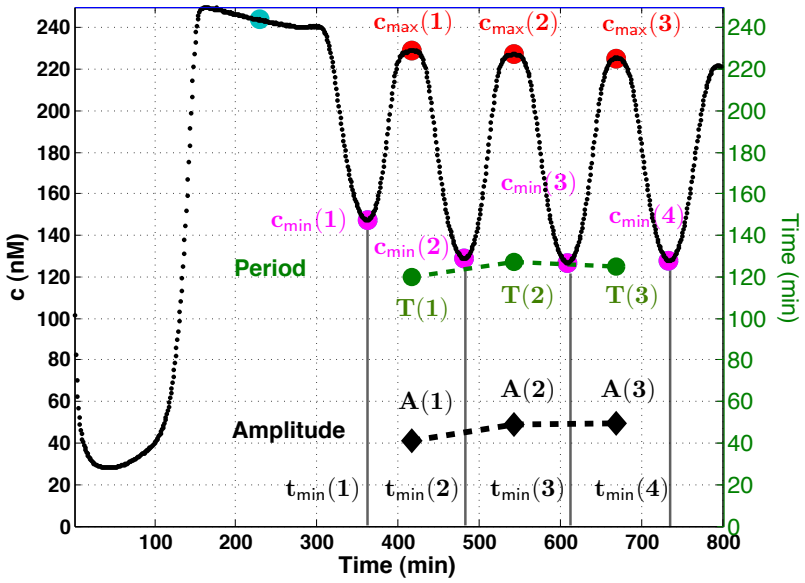

Figure S20: TWII-3. Red circles: selected oscillation maxima. Pink circles: selected oscillation minima. The cyan circle indicates the first large oscillation peak, not selected for period/amplitude analysis. Green trace: period per oscillation. Black trace: amplitude per oscillation.

11 Sample-to-Sample Variations

This section shows the sample-to-sample variability of oscillations in the same data acquisition run (each run includes four different samples). Such variability is mainly caused by pipetting inaccuracies and losses of DNA or enzymes sticking on the tube walls and pipet tips.

Two sample-to-sample variation test were run at TUM, data sets A and B. For each of the data sets we prepared fresh DNA and enzyme stocks. Each of the four samples from one set was pipetted separately from these stocks. Data set 1 also contains a sample-to-sample recording (sts-1) that was taken prior to all other (tweezers and aptamer) measurements. We found that within one set, the oscillation period from sample to sample vary by a maximum of 10% from each other. The period is calculated as detailed in Section 10. All sample-to-sample data sets together with the oscillation periods derived from it are shown in the following figures.

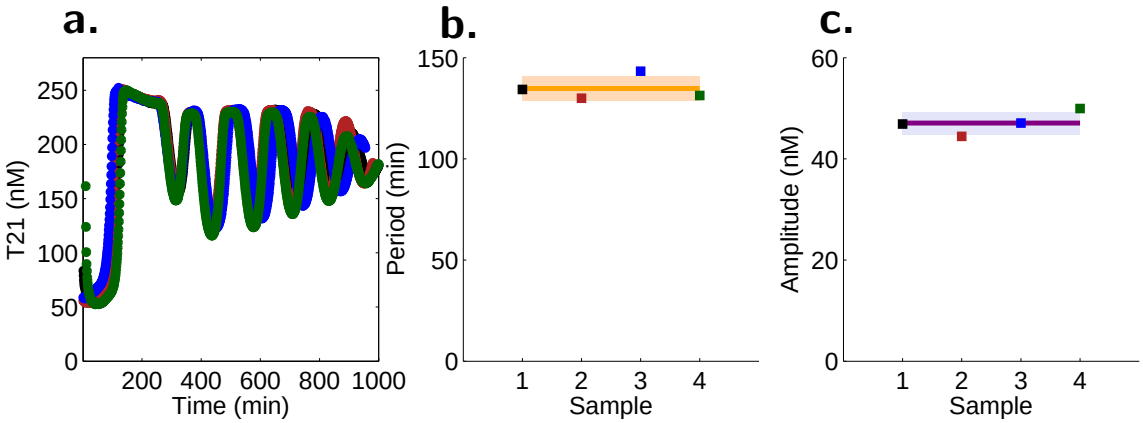

Figure S21: Sample-to-sample variations (set A). All four samples are meant to be identical, prepared from identical stock solutions, which were freshly prepared for this data set.
a. Time traces of the T21 concentrations.
b. Oscillation period determined from the fluorescence traces. Mean value is indicated by the orange solid line. The light orange rectangle highlights the standard deviation.
c. Oscillation amplitude. Mean value is indicated by the purple solid line. The light purple rectangle highlights the standard deviation.

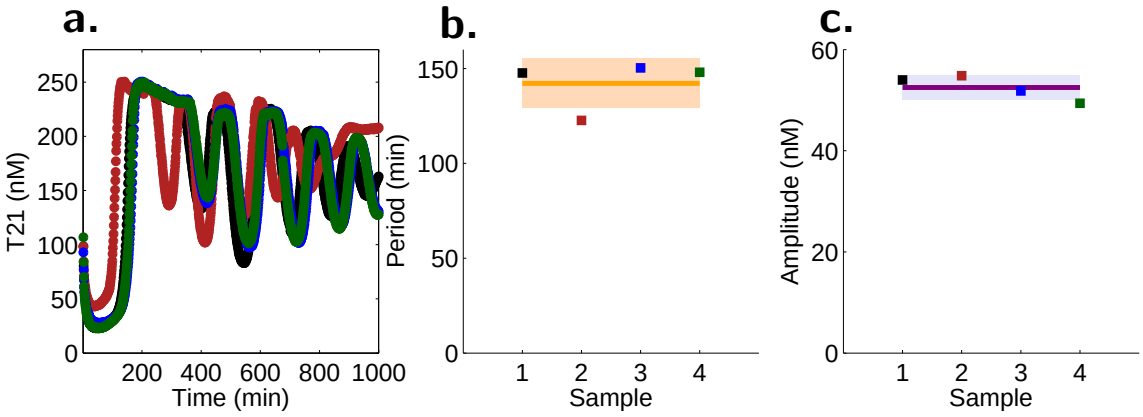

Figure S22: Sample-to-sample variations (set B). Samples are prepared from identical stock solutions, which were freshly prepared for this data set. One sample trace (red) deviates presumably due to an unrecognized pipetting mistake.
a. Time traces of the T21 concentrations.
b. Oscillation period determined from the fluorescence traces. Mean value is indicated by the orange solid line. The light orange rectangle highlights the standard deviation.
c. Oscillation amplitude. Mean value is indicated by the purple solid line. The light purple rectangle highlights the standard deviation.

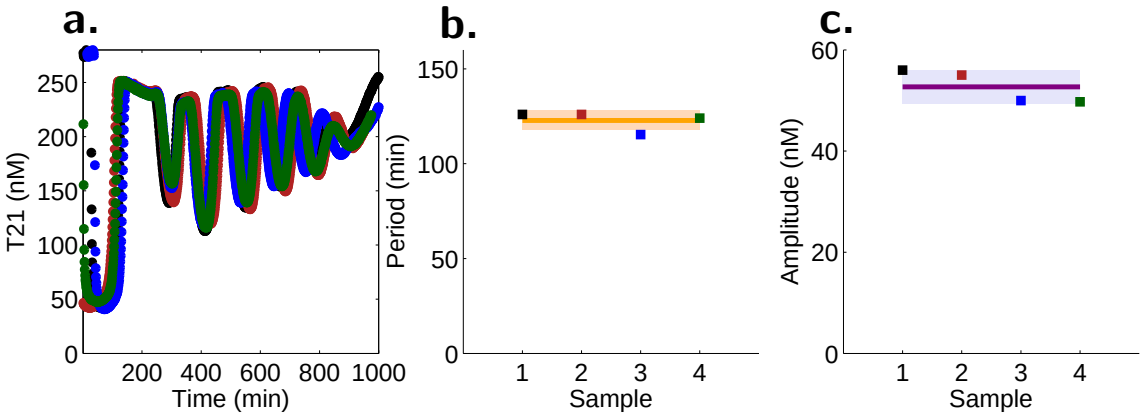

Figure S23: Sample-to-sample-variations (set sts-1). All four samples are meant to be identical, prepared from identical stock solutions, which were freshly prepared for this data set.
a. Time traces of the T21 concentrations.
b. Oscillation period determined from the fluorescence traces. Mean value is indicated by the orange solid line. The light orange rectangle highlights the standard deviation.
c. Oscillation amplitude. Mean value is indicated by the purple solid line. The light purple rectangle highlights the standard deviation.

12 Day-to-day Variations

In this section, we highlight the oscillation variability introduced by pre-mixing of enzymes for use in different days.

For the data collected at TUM, the enzymes T7 RNAP and RNase H were pre-mixed once for each data set, to guarantee consistent enzyme ratios across several experiments. However, we verified that the activity of the enzyme pre-mix slightly changed from day to day. This caused slower oscillations over time, even though the mix was stored in a freezer (-20°C) and cooled on ice during pipetting. This effect is shown in Figure S24, black and red traces: the period slightly increases after 2-3 days.

The enzymes were instead pre-mixed right before each experiment run at Caltech. Pipetting errors are particularly likely when transferring small enzyme volumes, due to their typical ≈50% glycerol storage buffer. To minimize such errors, the volumes transferred were always larger or equal to 2 μl. The total pre-mix volume always exceeded by 20% the volume required in the experiment. Such pipetting precautions allowed us to achieve a fairly stable period across different experiments, as shown in Figure S24, orange trace. Data set 6 (Epicentre Biotechnology reagents), brown trace, showed a more pronounced day-to-day variability in period and amplitude. This is most likely due to the fact that several transcription buffer components (and not just RNAP and RNase H as in the

Ambion protocol) were mixed prior to each data acquisition round (see Section 4 for details on the protocol). For set 6, the amplitude is in particular reduced by the second small peak present in most traces.

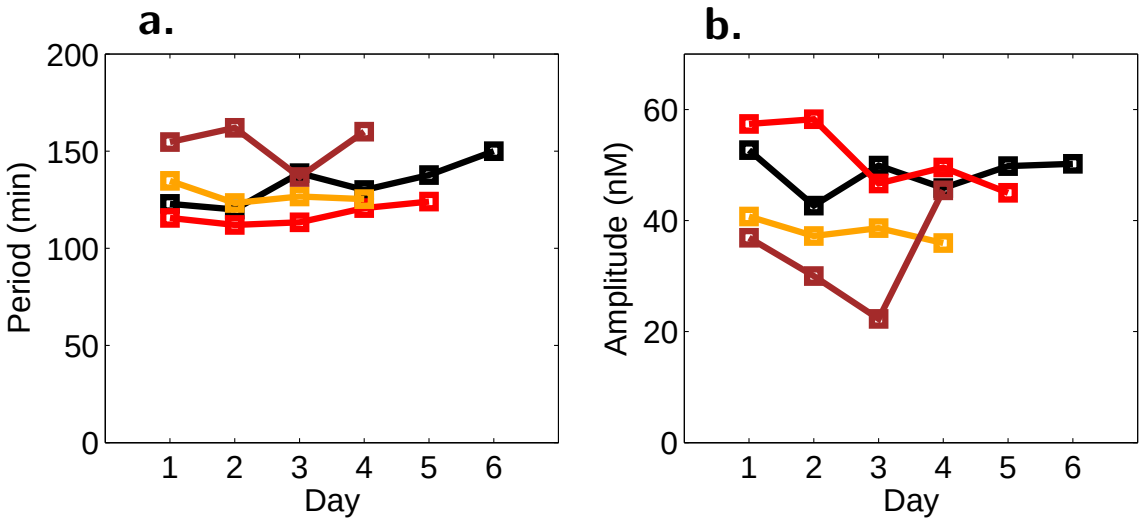

Figure S24: Period (a.) and amplitude (b.) vs. acquisition round numbers (day of acquisition). Data sets 1, 2 and 3 were taken at TUM using the same enzyme pre-mix: this figure shows (black and red trace) the trend of the same enzyme mix performance over several days of use. Set 1 rounds (black) include the sample-to-sample round (sts-1) shown previously (day 1), MG-1 (2), TWI-1 (3), TWII-1 (4), TWIII-1 (5) and a further test sample TS-1 (6). Set 3 rounds (red) include a callibration sample TS-3 (day 1), TWI-3 (2), TWIII-3 (3), MG-3 (4) and TWII-3 (5). The enzymes for sets 4 and 6 (orange and brown traces) were pre-mixed daily and this plot shows the day-to-day variability for this different protocol. Set 4 rounds (orange) include TWI-4, TWII-4, TWIII-4, TWIV-4. The corresponding time traces are presented either in the original paper (sets 3 and 4) or elsewhere in this supplement (set 1). Set 6 rounds (brown) include TWV* control from Figure S45, top; TWV* control from Figure S45, bottom; TWV control from Figure S44, third row; TWV control from Figure S44, fourth row.

13 Set-to-Set Variations

This section considers the overall variability of the oscillator operating point across different data sets: Figure S25 shows the mean and standard deviation of period and amplitude for each data set presented in this paper.

As shown in Sections 11 and 12, sample-to-sample period deviations are around 10%, and there can be activity variations in the enzyme pre-mixes, producing slower oscillations across different days of pre-mix use. To these two sources of variability, we must add the fact that different T7 RNAP/RNase H pre-mixes vary in activity from set to set.

This is in general more evident when switching to a new enzyme batch. Data set 6 presents high variability, particularly in the amplitude, because more reagents (Epicentre Biotechnology) are sequentially added in the transcription protocol, compared to the data sets collected using the T7 Ambion Megashortscript kit. Figure S26 shows a plot of period versus amplitude across different data sets.

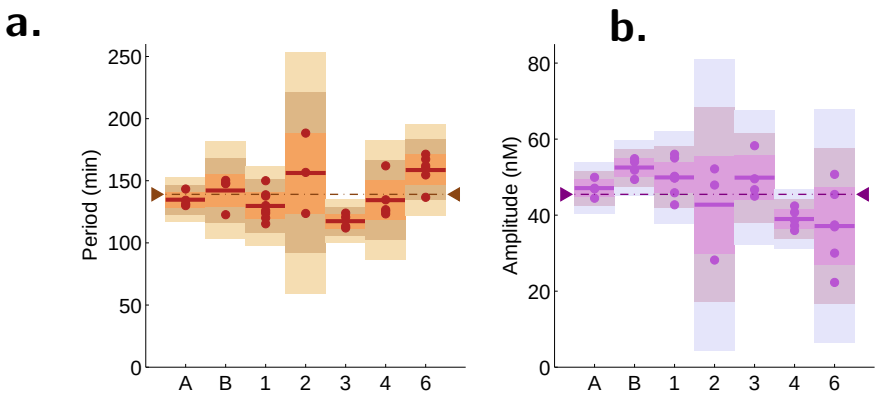

Figure S25: Set-to-set variability of period (a.) and amplitude (b.) of the oscillations. For each data set, data are marked with solid dots, their mean is a solid dark line, and the shaded areas cover the one, two and three standard deviations. The overall mean across data sets is indicated as a dash-dotted line with inward pointing arrows.

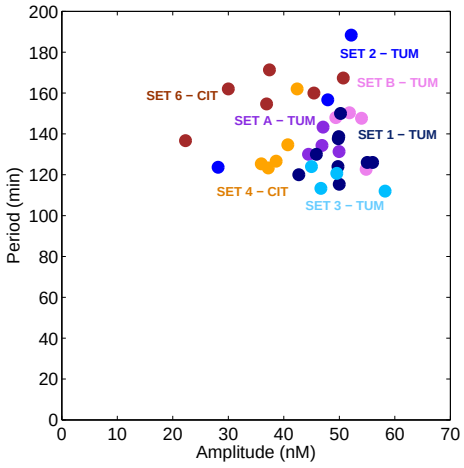

Figure S26: Overview of the period and amplitude correlation for all the control samples presented in this paper.

14 Oscillation Period

The period per each oscillation is measured between the first and the fourth minimum of each time trace. The nth minimum is defined as in Figure S20. Figure S27 gives an overview across different data sets for TWII, displaying the period from minimum n to minimum $n+1$.

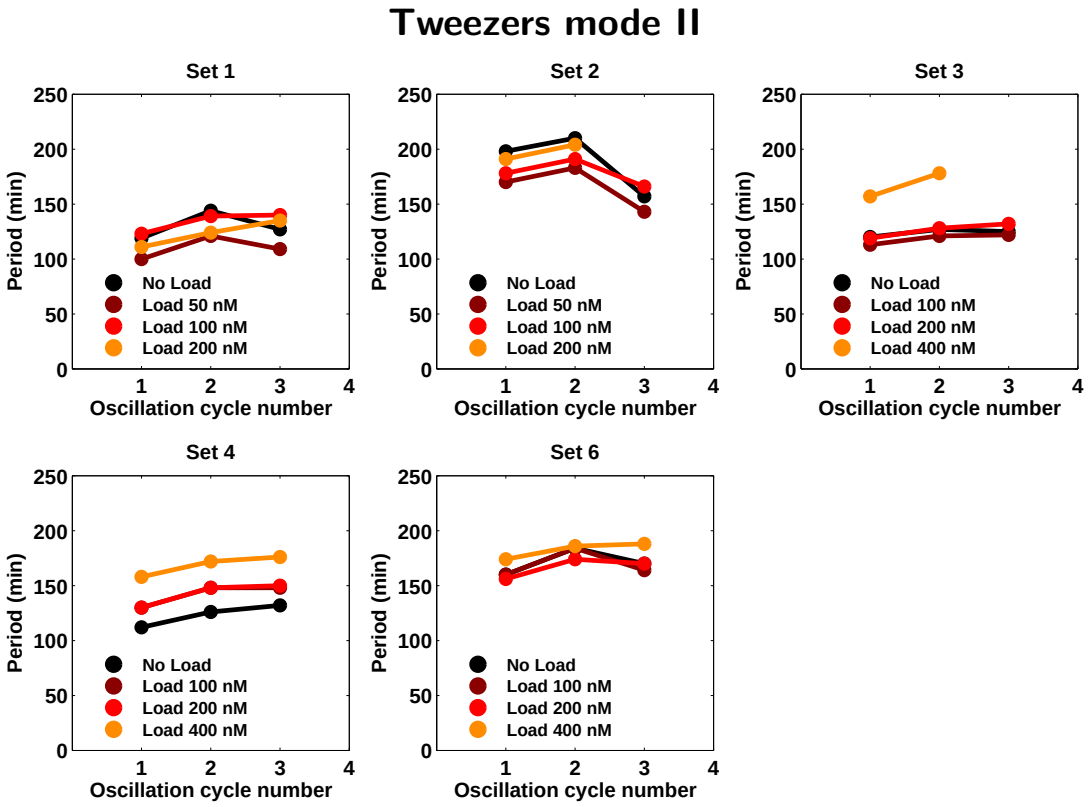

Figure S27: TWII, Period T(n) of each oscillations in the first three full oscillations.

15 Oscillation Amplitude

Figure S28 gives an overview of the oscillator amplitudes as a function of the oscillation cycle number for Tweezers mode II, across different data sets. Recall that the oscillation amplitude of oscillation cycle n is calculated as half the difference between the concentration at maximum and the preceding minimum, defined as in Figure S20:

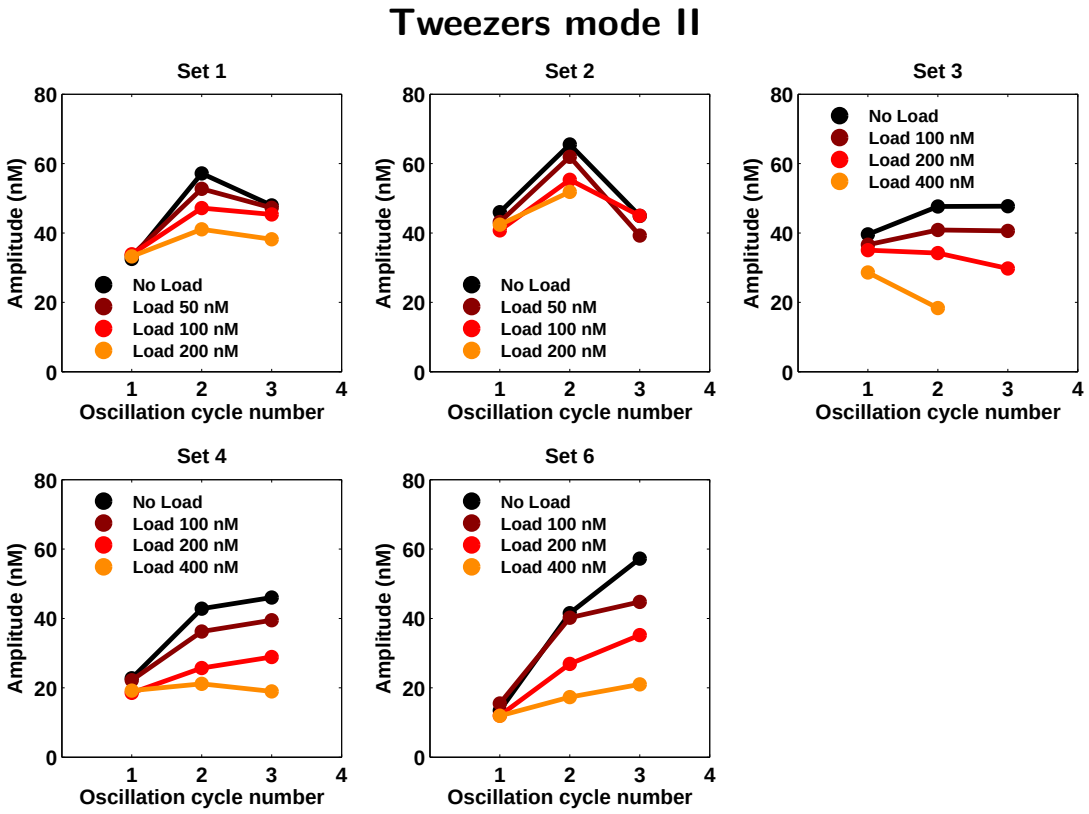

Figure S28: Amplitude A(n) of the oscillations in the first three full oscillations. The higher variability of sets 4 and 6 is due to the fact that in these sets the first oscillation after the plateau peak is consistently smaller than the following ones. Moreover, the protocol used for data set 6 requires more reagents to be sequentially added to the transcription mix, increasing the probability of pipetting inaccuracies.

16 Effects of the Load on the Oscillator Performance

The core oscillator performance is affected by the presence of a load. The higher is the load concentration, the stronger is the depletion of one (or more) of the core oscillator components: this causes an undesired retroactivity effect, namely a distortion of the oscillatory signal. In the following, we will provide some definitions and outline the load retroactivity effects we quantified.

The concentration of load that is to be driven by the oscillator is referred to as the *nominal load concentration*. For modes I–V this is equivalent to the concentration of the tweezers added. For the MG aptamer production mode, the nominal load is given by the MG switch concentration. The maximum swing of the concentration of downstream tweezers (modes I–V), is here called *effective load concentration*, and is calculated as twice the maximum amplitude per oscillation of the tweezers load.

The relative period change $\Delta T/T_0$ is calculated by defining ΔT as the difference between the loaded sample period T and the reference period T_0. We analogously calculate the relative amplitude change $\Delta A/A_0$. The relative period and amplitude changes (in all data sets) are plotted in Figure S29 a and c as a function of the nominal load concentration. As a guide to the eye, we calculated least square linear fits to each of the different modes of tweezers coupling and the rMG production.

The nominal load concentration affects the oscillator period most drastically for modes I and III, while the amplitude is affected by all modes except mode II* and mode V. Indeed, modes II* and V show the smallest effect on the oscillation period and amplitude, when the nominal load concentrations are considered. The period is in general increased by the presence of a load, while we find different amplitude perturbation effects. For some of the modes (I, II, II*, III and IV) a comparison with the effects of threshold variations is drawn in Section 21.

To evaluate the performance of the different modes, the efficiency of the coupling has to be considered. From this point of view, modes II*, III and IV do not qualify as successful coupling modes, because the load oscillation amplitude (defined as in Section 10) is too small (Section 22). Modes I, II, V and V* are actuated more strongly (Figures S30 and S31) with relative effective load concentration between roughly 10 and 60%. The relative change in oscillation period and amplitude is plotted as a function of the effective tweezers load concentration in Figure S29 b and d.

Modes I and II have similar amplitude retroactivity effects. Mode II presents a smaller period retroactivity; however, the percent effective load driven drops as a function of the nominal load, as shown in detail in Figure S30. It is easy to observe that the maximum concentration of Tweezers mode II that can be actuated should be well below [A1]=250 nM, whereas for mode I this boundary is given by [dI1]=700 nM.

For a system near our default operating point, a mean concentration of genelets in the "on" state of roughly 75 nM (30%) for SW21 can be deduced, while this concentration is only around 20 nM (17%) for SW12 (see Section 9). SW12 is turned on only for a short time in each cycle, resulting in a much lower concentration [rA1] as compared to [rI2]. Driving the tweezers with rA1 in mode IV therefore affects the oscillator more strongly than driving with rI2 in mode III, as the resulting reduction in rA1 concentrations yields a larger relative effect on switch activity. Similar reasoning explains why driving with A2 in modeII* has a negligible effect on the core oscillator even with a 400 nM load (Figure S29 and S41). However, the effective concentration of tweezers driven is practically zero. The high rI2 concentration and a toehold-mediated reaction pathway (Figure S4) allows the quick removal of A2 from tweezers; presuming closing of tweezers is slower than removal, the A2 concentration still provides the same effective threshold for SW12 inhibition. Presumably, the closing of tweezers by A2 is also slower than the hybridization of A2 to T12. We can conclude that the presence of a high amount of rI2 prevents direct coupling of TWII*, obviously decreasing the retroactivity.

The insulator of mode V minimally affects the core trajectories, analogously to mode II*. On the other hand, the RNA output InsOut amplifies minimal oscillations in the state of this load switch (analogously to what happens for SW12) and this mode achieves a good signal propagation on TWV.

The insulator designed for mode V* shows very low period retroactivity and has the best performance in terms of effective load driven (Figure S31). However, the amplitude retroactivity is significant. We can try to explain the properties of mode V* as follows. First, mode V* has the same input stage of SW21. This likely means that this load genelet is in an on state for a large fraction of time as SW21, maintaining a high concentration of InsOut (similar to what is observed for rI2). This explains why, given a certain effective load, a much smaller amount of insulator V* is required, compared to insulator V (mostly off as SW12). However, the output of mode V* in turn binds to the TwCls strand forming a substrate for RNase H, which is likely to be abundant most of the time following the reasoning done for rI2 (more abundant than in mode V). This hypothesis is consistent with the large plateaus in Figure S45. Through gel electrophoresis experiments (see Figure S32), we also found that the insulator of mode V* has a much larger off-state transcription rate than SW21. Leakier transcription would also result in larger amounts of InsOut in solution, and more substrate for RNase H. In fact, significantly decreasing the amount of RNase H in solution results in slower reference oscillations with larger amplitude (Section 20). It is thus plausible that the significant amplitude retroactivity of mode V* is caused by the presence of larger amounts of substrate for RNase H. Note that the MG switch has the same input stage of insulator mode V* (SW21), though its retroactivity effects are different: in fact, the aptamer output does not bind to any DNA target and does not create additional substrates for RNase H.

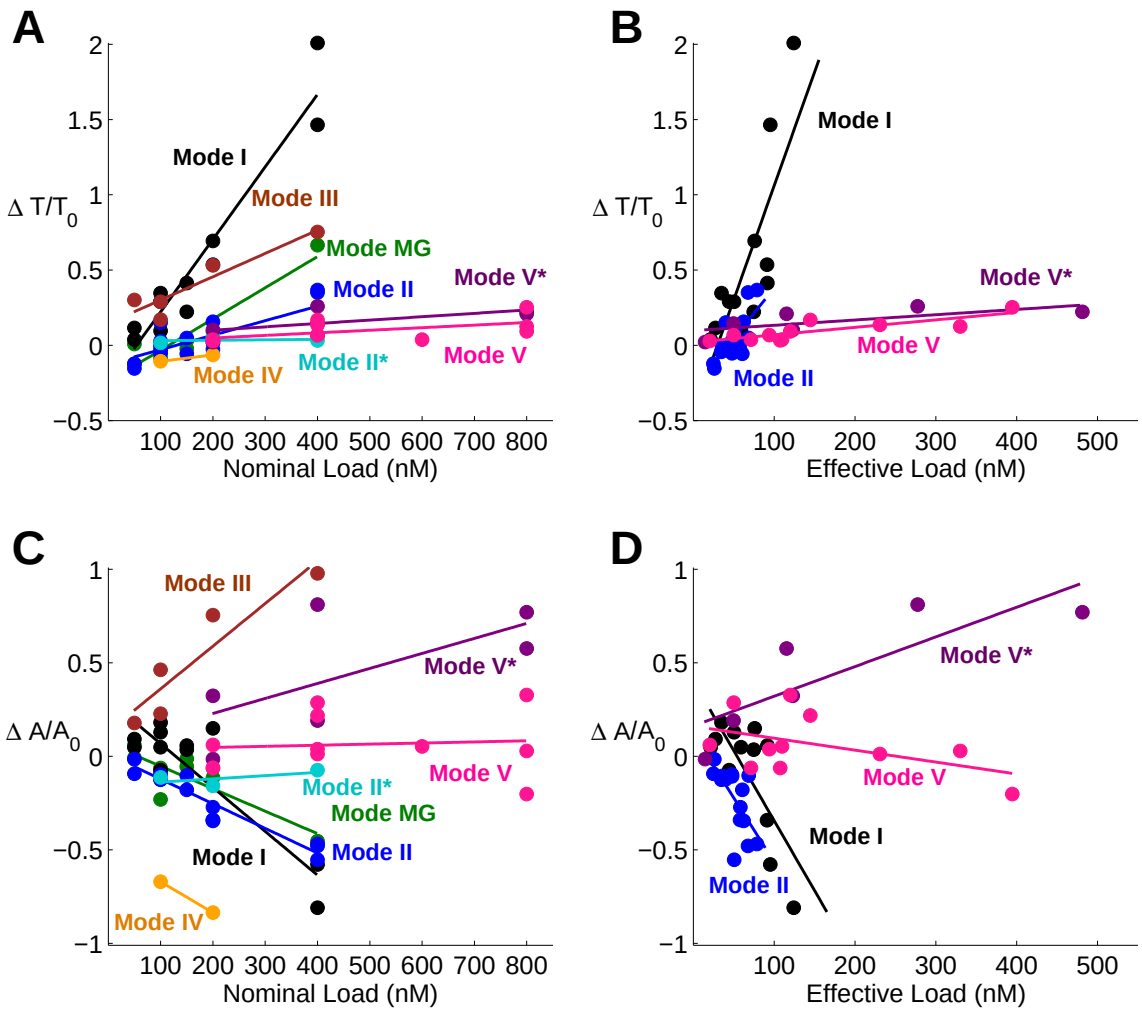

Figure S29: Relative period and amplitude change as a function of the load concentration for all sets. The data points are shown only when the oscillator traces exhibit a detectable amplitude and period. **a.** Nominal tweezer load versus core oscillator period variation. **b** Effective tweezer load versus core oscillator period variation. **c.** Nominal tweezer load versus core oscillator amplitude variation. **d.** Effective tweezer load versus core oscillator amplitude variation.

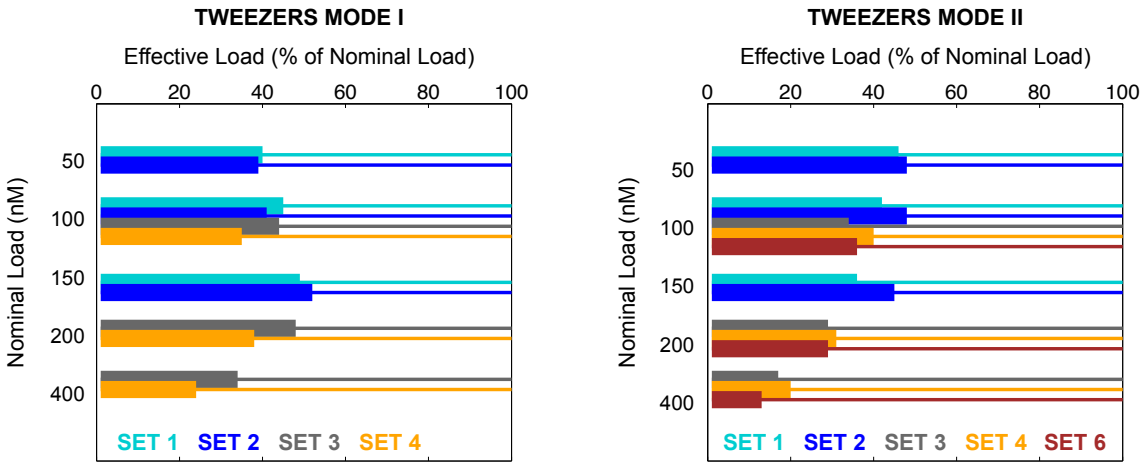

Figure S30: Effective load for mode I and mode II across different data sets.

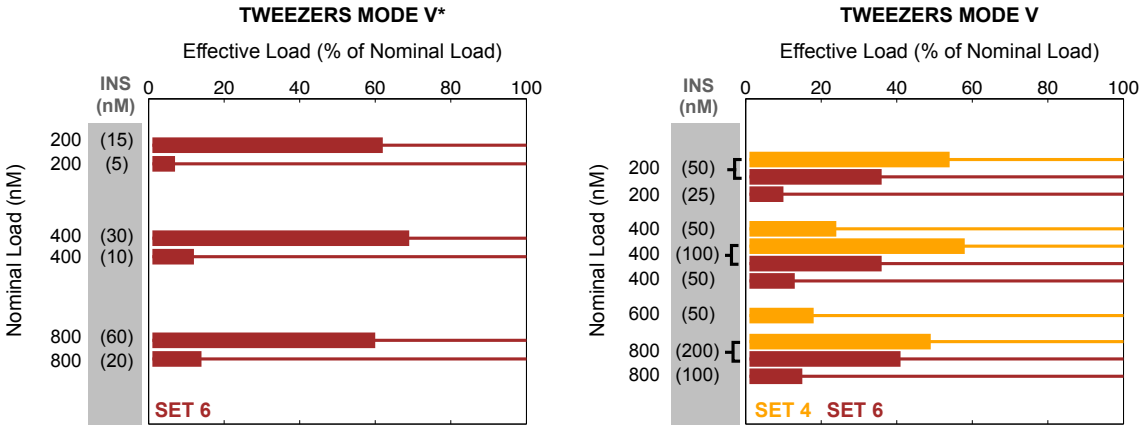

Figure S31: Effective load for mode V* and mode V across different data sets.

17 Leak Transcription from Off-State Switches

The synthetic genelets are switched on and off by displacing part of their nicked promoter region. The switches in the on-state (T12·A2, T21·A1, TMG1·A1) have a fully double-stranded, yet nicked promoter region, whereas in the off-state (T12, T21, TMG1) the promoter region of the switches is partly single-stranded. We tested the off-state and on-state transcription for all of our switches: T12·A2, T21·A1, TMG1·A1, Ins·A2 and Ins*·A1.

Figure S32 shows the gel electrophoresis results of samples from transcription reactions, for the core oscillator switches and the insulator switches. All of the switches were separately annealed and mixed with 1x Ambion Megashortscript kit reagents and 5$\%$ (v/v) Ambion T7 enzyme mix, in the presence or absence of their respective activator strand. Final concentrations of all the annealed switches were 200 nM, and the activators were added in excess, to a final concentration of 350 nM. The reaction was incubated at 37°C for 4 hours. RNA yield was quantified with 10$\%$ denaturing PAGE, run at 21°C. Template T21 has a higher off-state transcription rate than T12. The mode V* insulator, with input domain identical to T21, also exhibits higher off-state transcription than the mode V insulator.

We also transcribed the MG aptamer from its corresponding TMG1 genelet, in the presence of MG dye, measuring the fluorescence trace of MG emission. After $\approx$ 200 min, the activator strand A1 was added in order to turn on transcription. From the ratio of the linear fits before and after addition of A1 (the latter only for the linear regime for $t <$ 800 min), we conclude that the leak transcription rate is only 2.7$\%$ of the on-state transcription rates. RNase I (New England Biolabs) was added at the very end to verify that the fluorescence was caused by transcription of the RNA aptamer.

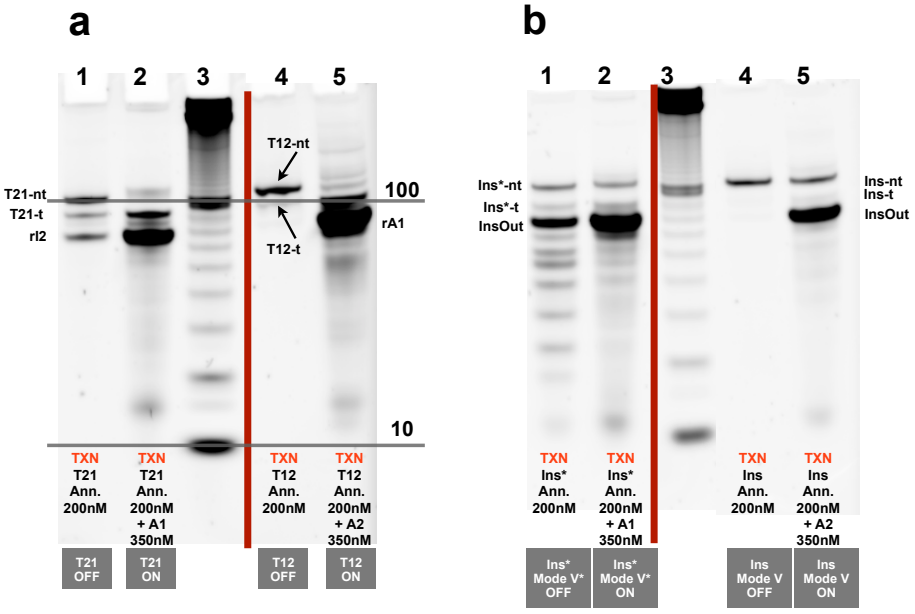

Figure S32: Off-state vs on-state transcription: **a.** Core oscillator switches. **b.** Mode V and mode V* insulator switches. Staining of the template and non-template strands is inconsistent. The red line indicates that the gel image has been processed by cropping some irrelevant bands. (Data collected at Caltech.)

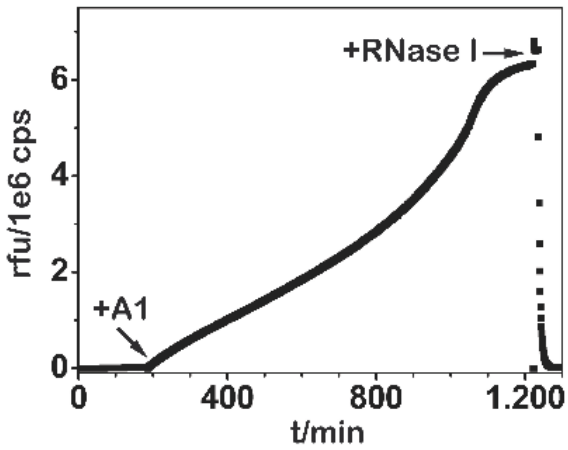

Figure S33: Transcription of MG aptamer before and after addition of activator A1. (Data collected at TUM.)

18 Lack of Transcription From T21·rA1 Complex

We investigated what is the extent of transcription from T21·rA1 complex (See Figure S2). Annealed T21-t and T21-nt strands at 250 nM were added with variable amounts of strands rA1. Transcription was performed in Ambion T7 Megashortscript kit 1x reagents, incubated at 37°C for 4 hours. Yield was quantified with 10% denaturing PAGE, run at 21°C. Additionally, following the same protocol, transcription of A1-activated template T21 was tested, showing strong transcriptional activity. The results show that the unwanted interaction between rA1 and SW21 produces negligible amounts of rI2 transcript, compared to the correct activation pathway (compare lanes 5 and 6 in Figure S34a to lane 5 in Figure S34b). Note that the TMG1 and the insulator mode V^* genelets have the same input domain of T21, and will exhibit the same undesired interaction with rA1. We hypothesize that transcription from those complexes is weak as for the T21 case, even though an experimental verification of this assumption has not been done.

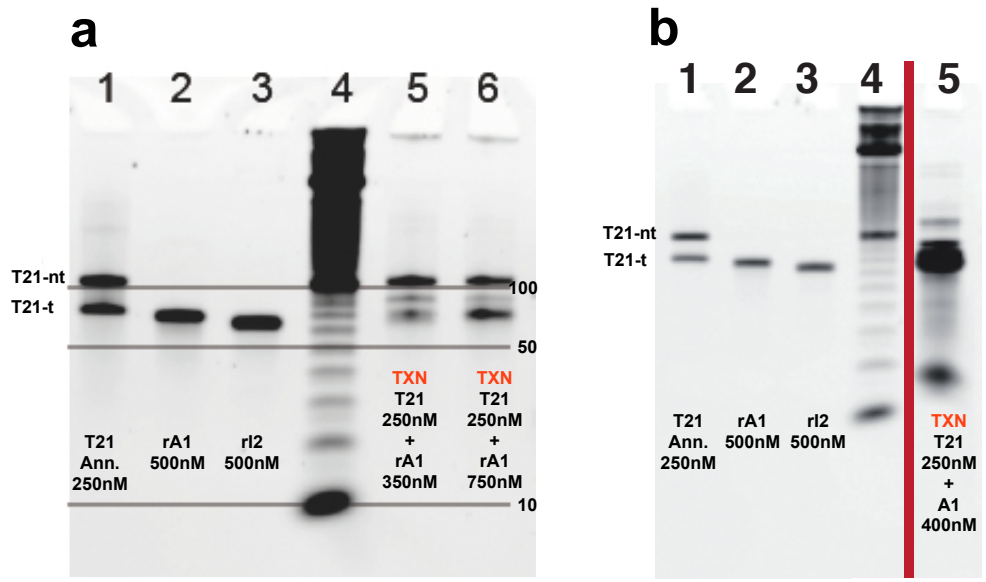

Figure S34: a. Transcription from T21·rA1 complex
Lane 1: Control sample, annealed T21-t and T21-nt at 250 nM, in 1x Ambion T7 Megashortscript transcription buffer. **Lane 2:** Control sample rA1 at 500 nM. **Lane 3:** Control sample rI2 at 500 nM. **Lane 4:** 10 bp DNA ladder. **Lane 5:** Transcription of annealed T21 at 250 nM with rA1 at 350 nM. **Lane 6:** Transcription of annealed T21 at 250 nM with rA1 at 750 nM.
b. Transcription from T21·A1 complex.
Lane 1: Control sample, annealed T21-t and T21-nt at 250 nM, in 1x Ambion T7 Megashortscript transcription buffer. **Lane 2:** Control sample rA1 at 500 nM. **Lane 3:** Control sample rI2 at 500 nM. **Lane 4:** 10 bp DNA ladder. **Lane 5:** Transcription of annealed T21 at 250 nM with A1 at 400 nM. The red line indicates that the gel image has been processed by cropping some non relevant bands between lane 4 and lane 5. (Data collected at Caltech.)

19 Interactions Between Enzymes and Tweezers

Molecular tweezers can be a substrate for RNAP. This was observed through gel electrophoresis and fluorescence measurements on tweezer modes I-IV. Figure S35 shows the results on tweezers mode II. These were tested as a transcription substrate by adding them at a concentration of 200 nM to Ambion T7 Megashortscript kit 1x reagents. A denaturing 10% PAGE run at 21°C shows unknown transcription products of different lengths. Some of these products are degraded by RNase H, as can be seen from Figure S35. This suggests that such products bind to the DNA tweezer strands. In fact, the fluorescence time traces in Figure S36 show that transcription products interact through an unknown mechanism with the tweezers, causing an increase in fluorescence. The presence of RNase H again reduces this phenomenon by degrading tweezers-bound RNA.
The extent of transcription from a tweezer substrate is sequence-specific. Some of the tweezer designs we tested exhibited a drift in fluorescence over time of up to 30% even in the presence of RNase H, and had to be discarded. The presence of T7 promoter sub-sequences in such tweezer designs might have favored the interaction with RNAP.

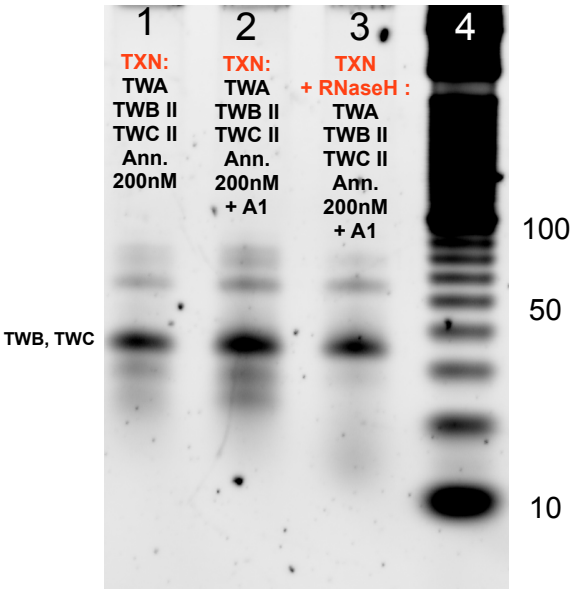

Figure S35: Denaturating 10% PAGE. **Lane 1:** Transcription run on TW II A, B and C all at 200 nM. **Lane 2:** Transcription run on TW II A, B, C and A1 all at 200 nM. Note that TW II A is not visible due to the quencher present on the strand. **Lane 3:** Reaction products of Lane 2 after 30 min incubation with 2% (v/v) Ambion RNase H. Unknown transcription products of different lengths appear in all lanes; some of the products, that most likely bind to the DNA tweezers, are degraded by RNase H and disappear in Lane 3. **Lane 4:** 10 bp DNA Ladder. (Data collected at Caltech.)

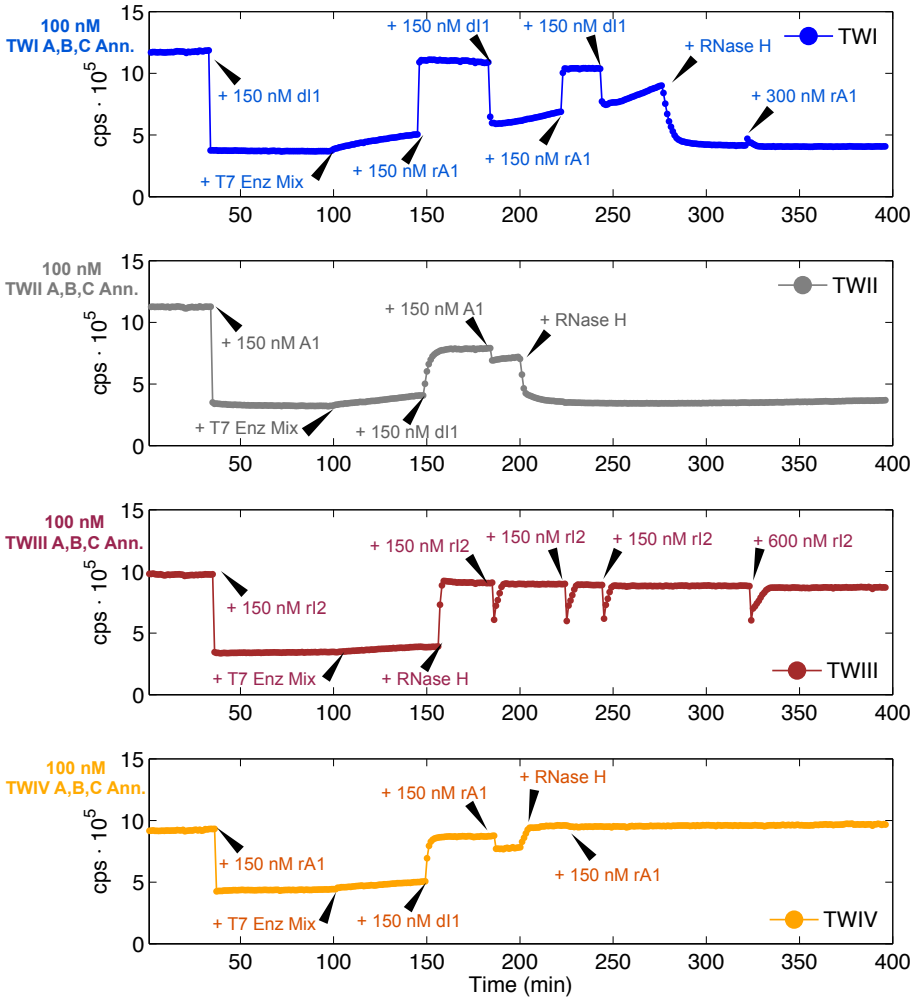

Figure S36: Raw fluorescence time traces showing opening and closing cycles for TW I, II, III and IV. Initially, 100 nM annealed tweezers are present in solution with 1x Ambion T7 Megashortscript kit buffer and 7.5 mM each rNTP. Nucleic acid strands are added at different times according to the indicated labels. Enzymes are added as follows: Ambion T7 Enzyme Mix is added in 3 μL aliquots; RNase H is added in 0.2 μL aliquots (2 units from a stock of Ambion RNase H 10 U/μL). The final volume of each sample is 60 μL. (Data collected at Caltech.)

20 Effect of Changing Enzyme Volume Ratio

In this section, we briefly discuss the dependence of frequency and amplitude of the oscillator on the volume ratio of RNAP and RNase H.

As mentioned before, we tuned the enzyme amounts in the Caltech and TUM protocols in order to achieve a similar operating point, defined as 4-6 full oscillations having amplitude around 100 nM. The tuning operation involved mainly an exploration of the system behavior as a function of the relative enzyme concentrations. As shown in Figure S37, increasing the volume of RNase H produces faster oscillations, and lower amplitude.

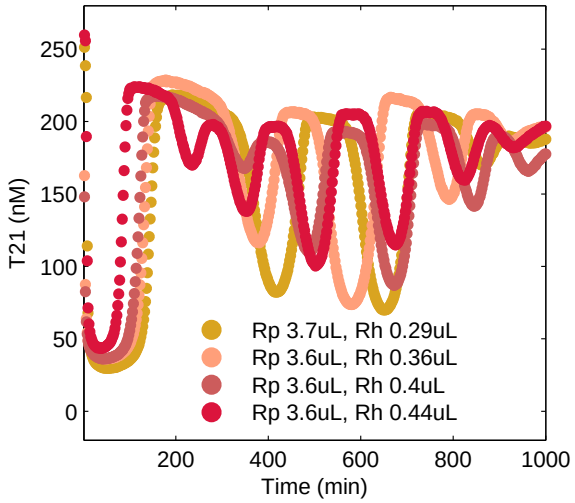

Figure S37: SET 6, with $[dI1]_{tot}$=700 nM, Data taken in different days

21 Effect of Changing the Concentrations of the DNA Thresholds

The influence of different coupling schemes on the dynamics of the transcriptional oscillator can be better understood by considering the effect of the tweezers in the context of the full set of chemical reactions occurring in the system. Due to their interaction with different molecular species in the core oscillator system, the tweezers effectively change the concentrations of the threshold strands A2 and dI1. In mode I, tweezers are closed by dI1 and opened via a strand displacement reaction by rA1. In the core oscillator, strand A1 is similarly bound by dI1 and freed via a strand displacement reaction by rA1. We reasoned that an increase in the concentration of mode I tweezers therefore roughly mimics an increase in A1, which in turn corresponds to an effective reduction of the threshold set by [dI1]. In contrast, increasing the concentrations of tweezers in mode II or mode IV resembles an increase in [dI1]. In mode II, a fraction of activator strands A1 is bound to the tweezers rather than to template T21. Dynamically, the effective

reduction in [A1] should be analogous to an increase in threshold by [dI1]. In mode IV, a fraction of the rA1 transcripts is sequestered by the tweezers, effectively shifting the threshold for activation of SW21 to higher values. Finally, an increase in tweezers concentration in mode III should be similar in effect to an increase in A2 concentration, as a fraction of the rI2 transcripts is bound by the tweezers, while an increase in modeII^* tweezers, which are closed by A2, should correspond to a decreased A2 threshold. We experimentally challenged this interpretation of loads as effective changes in threshold values. Figure S38 shows fluorescence traces recorded from the unloaded oscillator, for which the concentrations of the threshold strands dI1 and A2 were systematically varied. The general trends in amplitude and period closely resemble the trends observed in Figures S39, S40, S41, S42 and S43 for modes I, II,II^*, III, and IV, agreeing well with the heuristic expectations detailed above. An exception is the slowing down of the oscillations with increasing tweezers concentration operated in mode II, perhaps due to the tweezers' direct effect being on A1 rather than dI1. The trends are also numerically analyzed and reproduced in Section 25 and Figure S54.

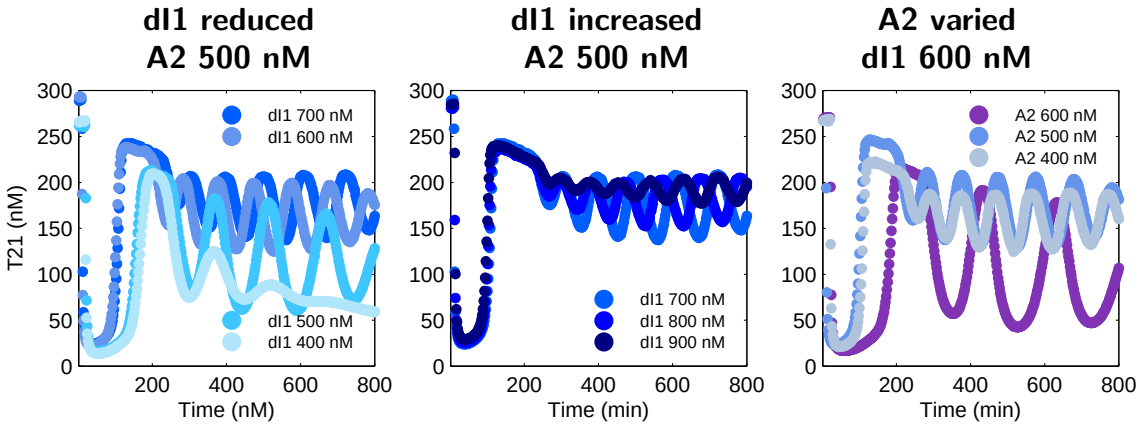

Figure S38: Threshold variation, set 5 samples. Oscillator traces with varying threshold concentrations. **Left:** the concentration of dI1 is reduced from 700 nM to 400 nM. **Center:** The concentration of dI1 is increased from 700 nM to 900 nM. **Right:** The concentration of A2 was varied from 400 nM over 500 nM (default concentration) to 600 nM.

22 Overview of All Data Sets

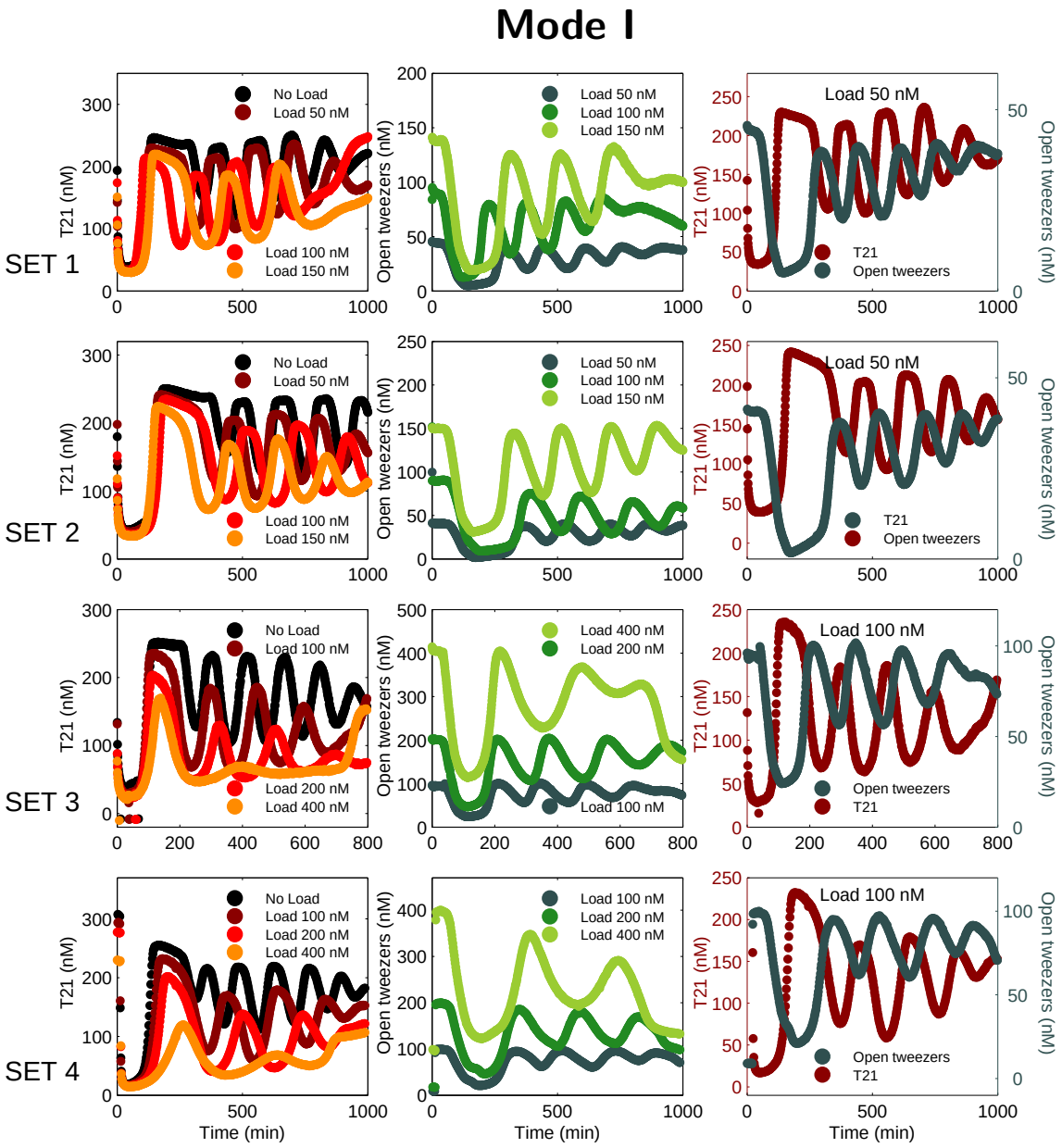

Figure S39: TWI-samples, sets 1–4. Left: Oscillator traces. **Center:** Load traces. **Right:** Oscillator and load traces.

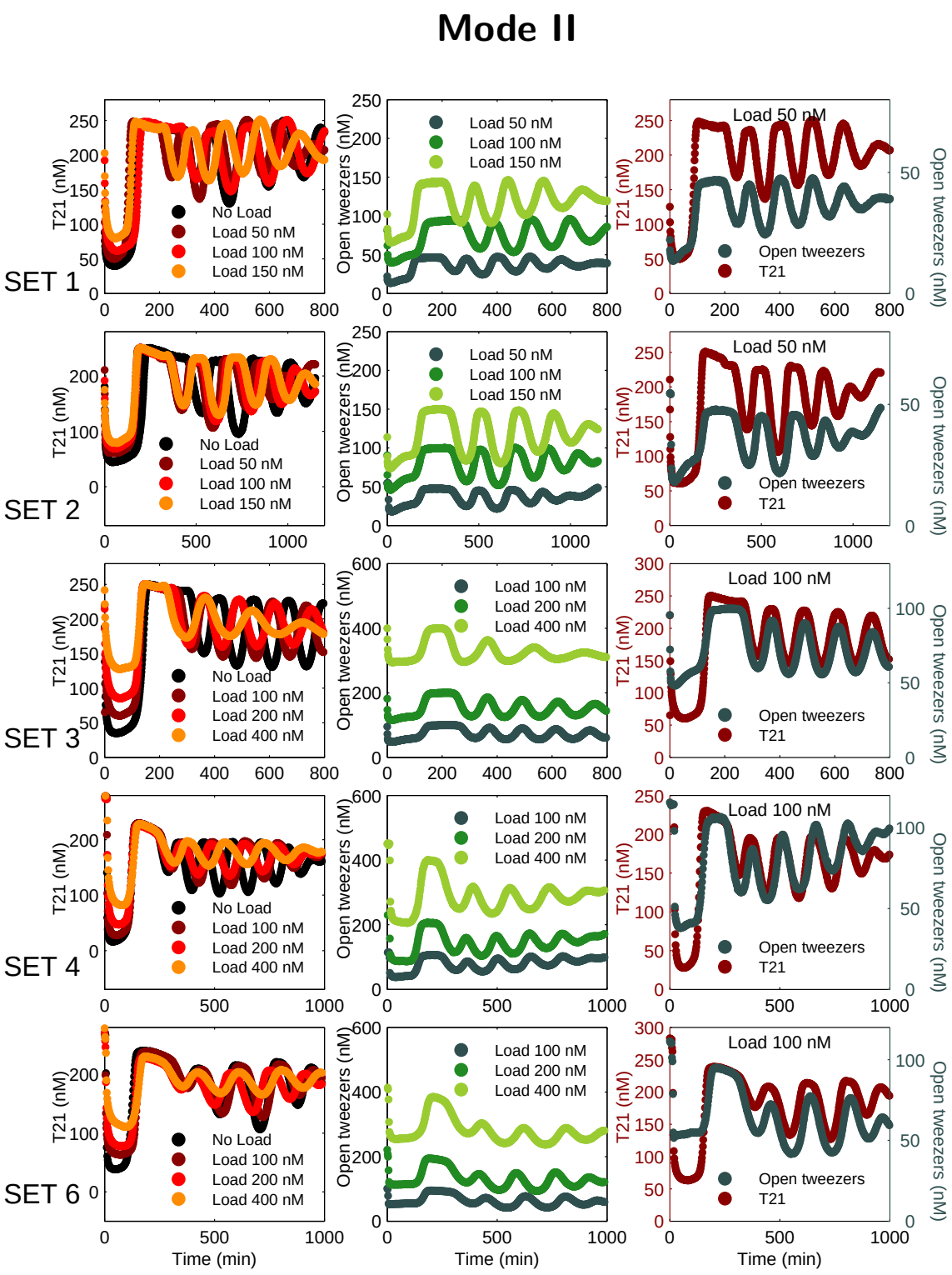

Figure S40: TWII samples, sets 1–4 and 6. Left: Oscillator traces. **Center:** Load traces. **Right:** Oscillator and load traces.

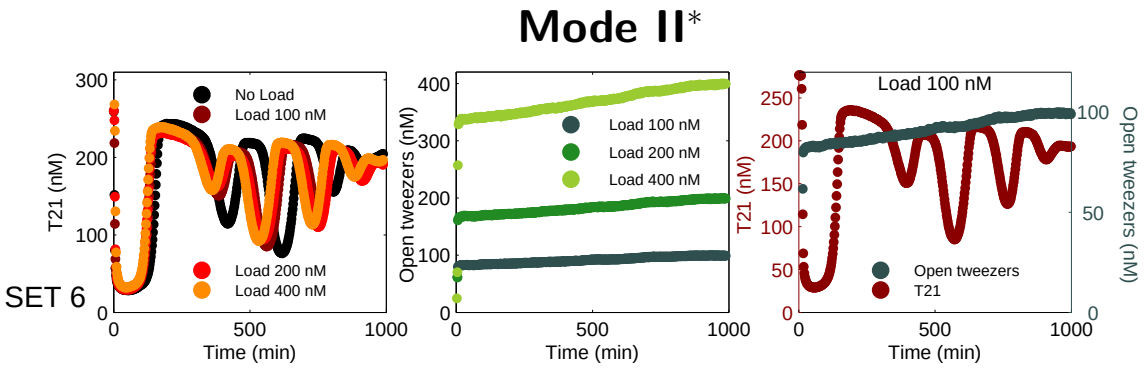

Figure S41: TWII* samples, set 6. Left: Oscillator traces. **Center:** Load traces. **Right:** Oscillator and load traces.

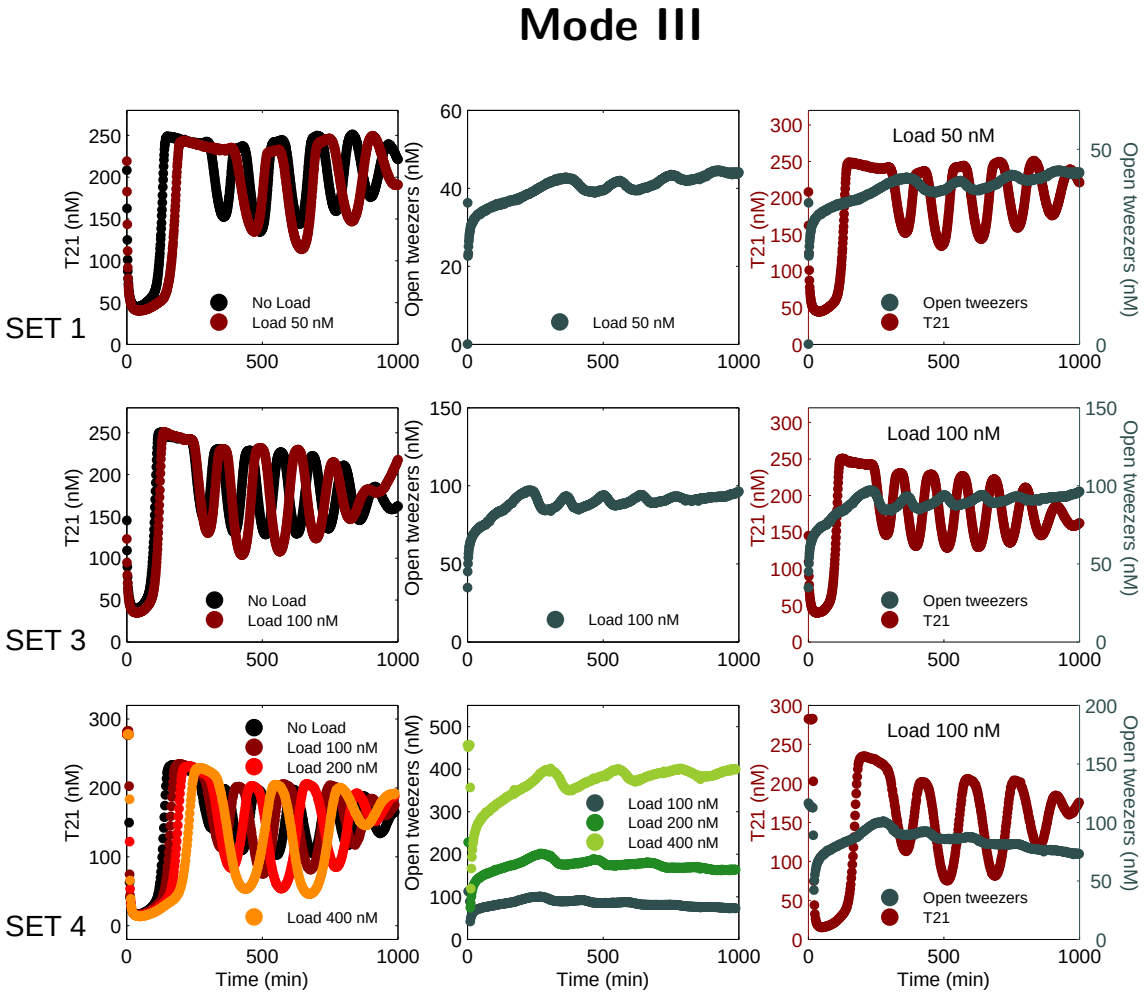

Figure S42: TWIII-samples, sets 1, 3 and 4. Left: Oscillator traces. **Center:** Load traces. **Right:** Oscillator and load traces.

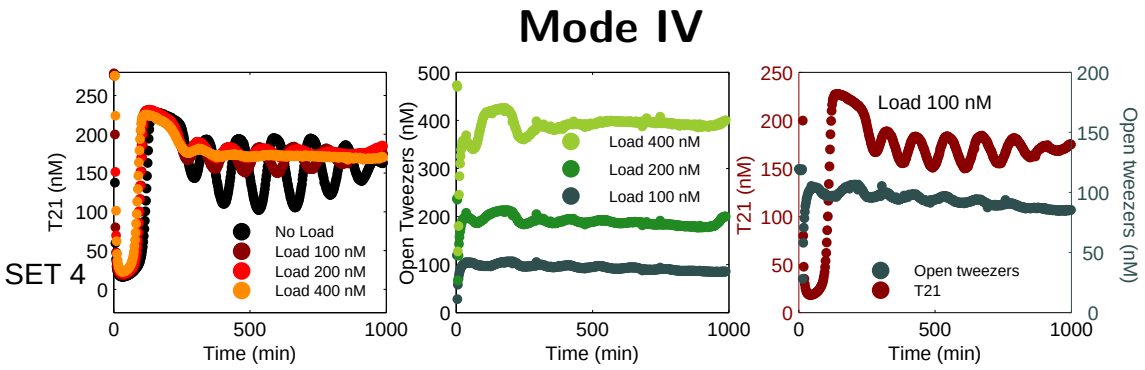

Figure S43: TWIV-samples, set 4. Left: Oscillator traces. **Center:** Load traces. **Right:** Oscillator and corresponding load traces.

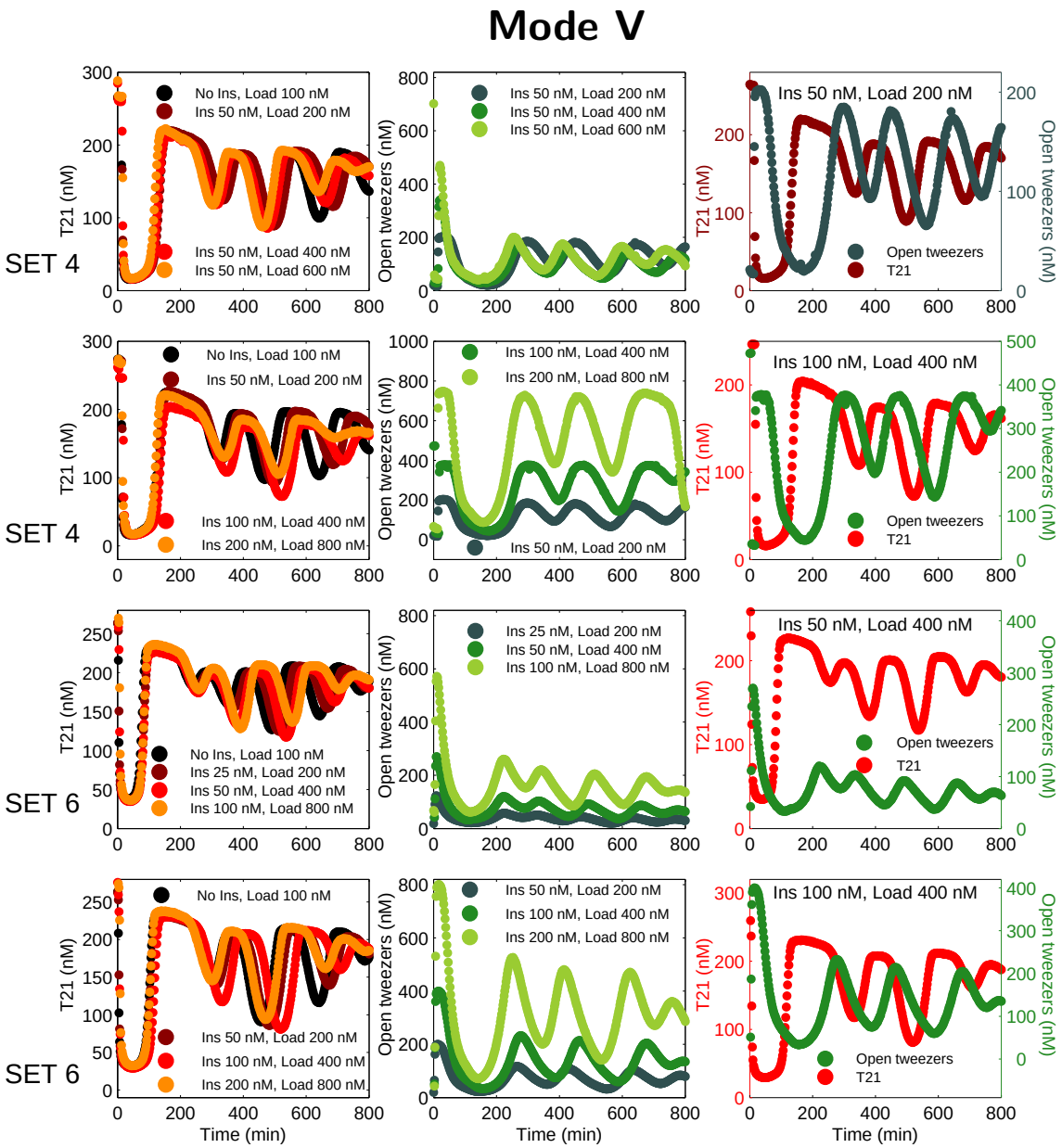

Figure S44: TWV samples, sets 4 and 6. Left: Oscillator traces. **Center:** Load traces. **Right:** Oscillator and corresponding load traces. The TwCls DNA strand was always added in 50 nM excess of TWV load.

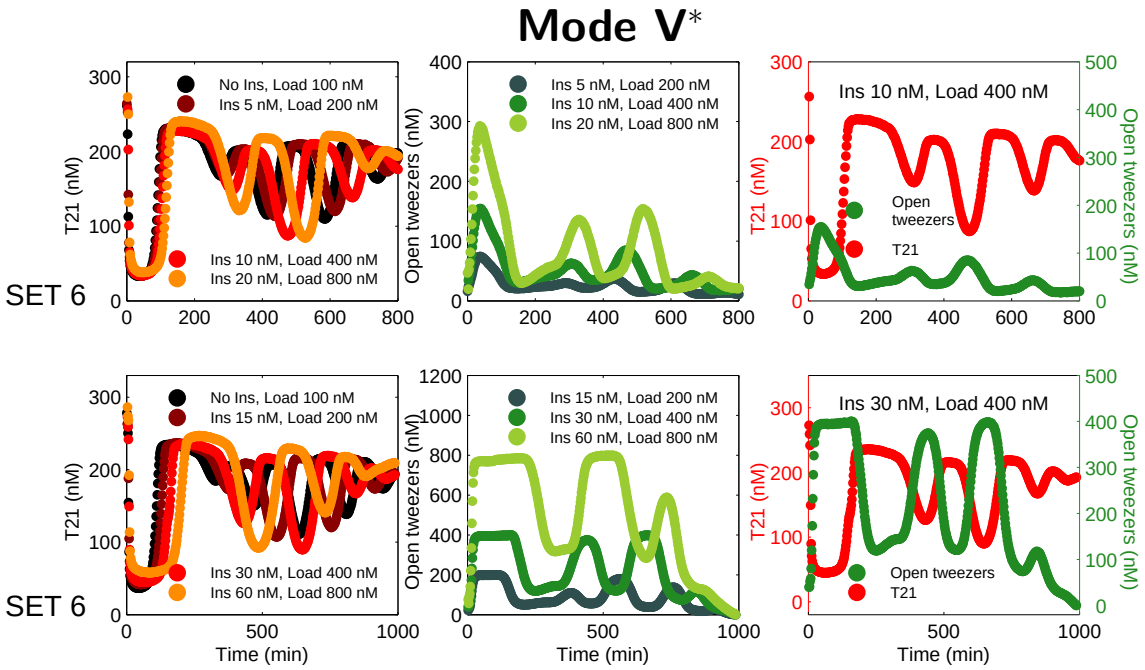

Figure S45: TWV* samples, set 6. Left: Oscillator traces. **Center:** Load traces. **Right:** Oscillator and corresponding load traces. The DNA strand TwCls (closing the mode V tweezers) was always added in 50 nM excess of TWV load.

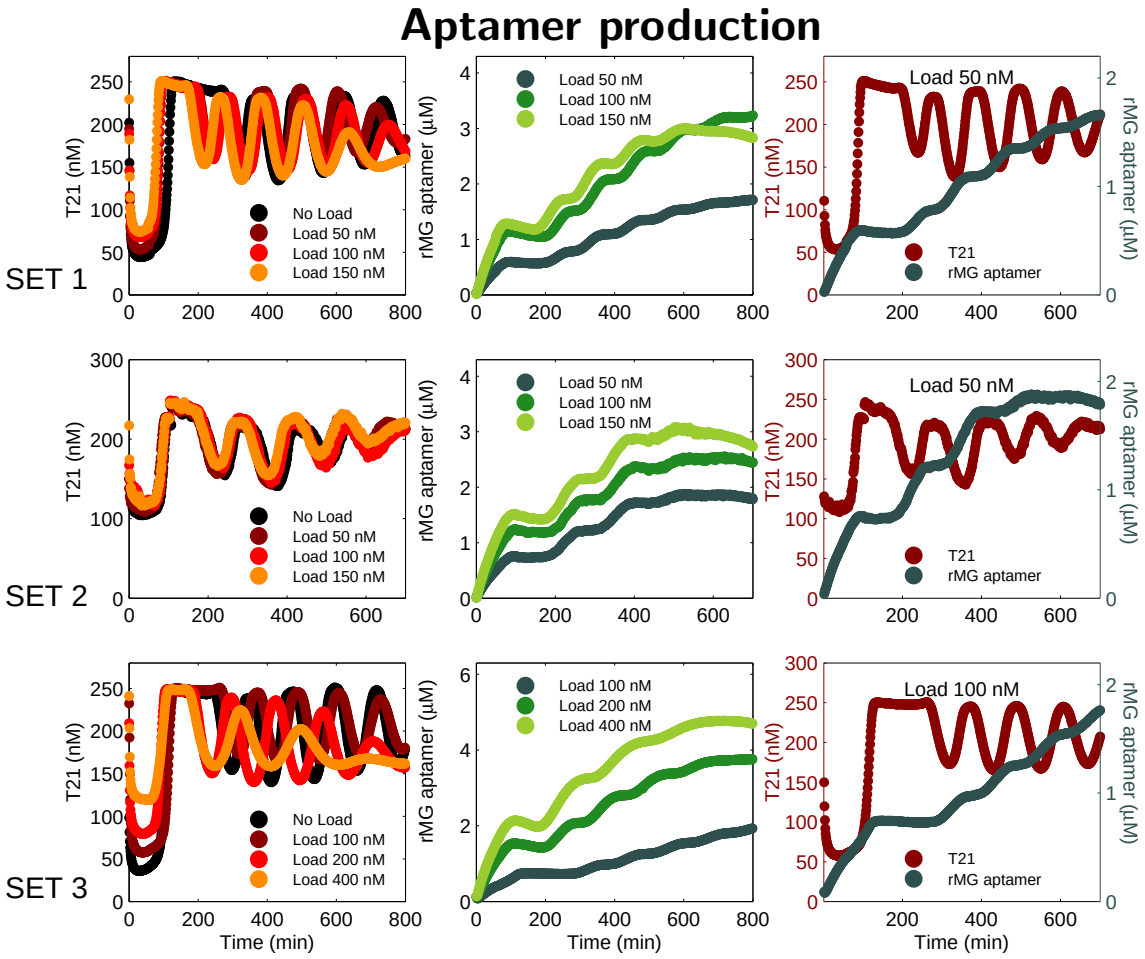

Figure S46: rMG-samples, sets 1, 2 and 3. Left: Oscillator traces. **Center:** Load traces. **Right:** Oscillator and load traces.

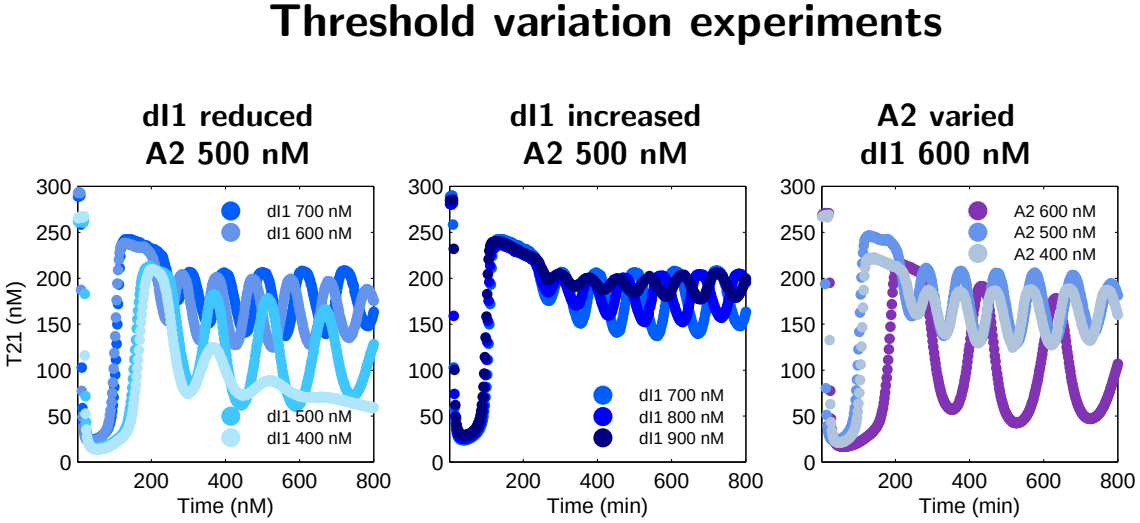

Figure S47: Threshold variation, set 5 samples. Oscillator traces with varying threshold concentrations. **Left:** the concentration of dI1 is reduced from 700 nM to 400 nM. **Center:** The concentration of dI1 is increased from 700 nM to 900 nM. **Right:** The concentration of A2 was varied from 400 nM over 500 nM (default concentration) to 600 nM.

23 Simple Model for the Oscillator: Load Coupling and Insulation

In this section, we will provide further details on the simple oscillator model presented in the main paper.

23.1 A simple model for the transcriptional oscillator and its non-dimensional version

Equations (1)–(4) were proposed in Kim and Winfree [2011] as a simple model for our transcriptional oscillator:

$$\frac{\mathrm{d}[\mathrm{rA1}]}{\mathrm{dt}} = \mathrm{k_p}[\mathrm{SW12}] - \mathrm{k_d}[\mathrm{rA1}], \tag{1}$$

$$\tau\frac{\mathrm{d}[\mathrm{SW21}]}{\mathrm{dt}} = [\mathrm{SW21^{tot}}]\frac{\frac{[\mathrm{rA1}]^{\mathrm{m}}}{\mathrm{KA^m}}}{1+\frac{[\mathrm{rA1}]^{\mathrm{m}}}{\mathrm{KA^m}}} - [\mathrm{SW21}], \tag{2}$$

$$\frac{\mathrm{d}[\mathrm{rI2}]}{\mathrm{dt}} = \mathrm{k_p}[\mathrm{SW21}] - \mathrm{k_d}[\mathrm{rI2}], \tag{3}$$

$$\tau\frac{\mathrm{d}[\mathrm{SW12}]}{\mathrm{dt}} = [\mathrm{SW12^{tot}}]\frac{1}{1+\frac{[\mathrm{rI2}]^{\mathrm{n}}}{\mathrm{KI^n}}} - [\mathrm{SW12}]. \tag{4}$$

A scheme representing the above equations is shown in Figure S48 A. The species rA1 and rI2 are RNA molecules that interact through two "genelet" switches that produce them, respectively SW12 and SW21. In particular, rA1 is an activator for SW21, while rI2 is an inhibitor for SW12. The effectiveness of the RNA species in activating or repressing the switches is modulated by the thresholds KA and KI, and by the Hill coefficients m and n. The relaxation constant τ scales the speed of the switches' dynamics. Unless otherwise noted, from now on the operating point of this oscillator model is defined by the parameters $\mathrm{k_p} = 0.05\,/\mathrm{s}$, $\mathrm{k_d} = 0.002\,/\mathrm{s}$, KA=KI=$.5\,\mu\mathrm{M}$, $[\mathrm{SW21^{tot}}] = [\mathrm{SW12^{tot}}] = 100\,\mathrm{nM}$, m=n=5, $\tau = 500\,\mathrm{s}$. Figure S48 B and C show the system trajectories generated using the MATLAB `ode23` routine from initial conditions $[\mathrm{rA1}](0) = 0\,\mu\mathrm{M}$, $[\mathrm{SW21}](0) = 0\,\mathrm{nM}$, $[\mathrm{rI2}](0) = 0\,\mu\mathrm{M}$, $[\mathrm{SW12}](0) = 100\,\mathrm{nM}$.

Non-dimensional model

The above model can be mapped to a set of non-dimensional differential equations as follows:

Nondimensional variables

$$\mathrm{x} = \frac{[\mathrm{rA1}]}{\mathrm{KA}} \quad \mathrm{v} = \frac{[\mathrm{SW21}]}{[\mathrm{SW21^{tot}}]}$$
$$\mathrm{y} = \frac{[\mathrm{rI2}]}{\mathrm{KI}} \quad \mathrm{u} = \frac{[\mathrm{SW12}]}{[\mathrm{SW12^{tot}}]}$$

Time rescaling

$$\tilde{\mathrm{t}} = \mathrm{t}/\tau$$

Nondimensional parameters

$$\alpha = \frac{\mathrm{k_p}\,[\mathrm{SW12^{tot}}]}{\mathrm{k_d}\,\mathrm{KA}} \quad \beta = \frac{\mathrm{k_p}\,[\mathrm{SW21^{tot}}]}{\mathrm{k_d}\,\mathrm{KI}}$$
$$\gamma = \frac{1}{\mathrm{k_d}\,\tau}$$

Nondimensional equations in $\tilde{t}$

$$\gamma\,\dot{\mathrm{x}} = \alpha\mathrm{u} - \mathrm{x}$$
$$\dot{\mathrm{v}} = \frac{\mathrm{x^m}}{1+\mathrm{x^m}} - \mathrm{v}$$
$$\gamma\,\dot{\mathrm{y}} = \beta\mathrm{v} - \mathrm{y}$$
$$\dot{\mathrm{u}} = \frac{1}{1+\mathrm{y^n}} - \mathrm{u}$$

Given our choice of the parameters, $\gamma = 1$. A value of $\gamma \approx 1$ is required to achieve oscillations, as found in Kim and Winfree [2011].

Existence of periodic orbits

It is convenient to investigate the existence of periodic orbits by taking into consideration the non-dimensional model. We will start by making the following observations:

1. The equilibrium of each variable x, v, y and u depends monotonically on its input. For example, given a fixed input $\bar{\mathrm{u}}_1$, the equilibrium of $\bar{\mathrm{x}}$ is $\bar{\mathrm{x}}_1 = \alpha\bar{\mathrm{u}}_1$. For any $\bar{\mathrm{u}}_2$, $\bar{\mathrm{u}}_2 > \bar{\mathrm{u}}_1$, then $\bar{\mathrm{x}}_2 > \bar{\mathrm{x}}_1$.
2. The trajectories of this system are always bounded. In fact, the switches concentration is bounded: $\mathrm{u}, \mathrm{v} \in [0, 1]$. The dynamics of x and y are exponentially stable, given a constant bounded input.
3. The system admits a unique equilibrium. In fact, by setting to zero the non-dimensional dynamics, we can derive the following expressions for the system null-clines:
$$\bar{\mathrm{x}} = \alpha\frac{1}{1+\bar{\mathrm{y}}^{\mathrm{n}}}, \qquad \bar{\mathrm{y}} = \beta\frac{\bar{\mathrm{x}}^{\mathrm{m}}}{1+\bar{\mathrm{x}}^{\mathrm{m}}}.$$
The above curves are monotonic and intersect in a single point, as shown in Figure S48 D. Therefore, the system admits a single equilibrium.

Based on the observations above, we can invoke the Mallet-Paret theorem (Mallet-Paret and Smith [1990]). This theorem is the extension of the Poincaré-Bendixson theorem

to dimension higher than 2, and is valid when the system dynamics are monotonic and cyclic, as in our case.
Based on the theorem, if observations 1., 2. and 3. are true, and if the unique admissible equilibrium of the system is unstable, then the system must admit a periodic orbit. We can verify the stability properties of the equilibrium by inspecting the eigenvalues of the Jacobian matrix at the equilibrium:

$$\mathsf{J} = \begin{bmatrix} \frac{\partial \mathrm{f_1}}{\partial \mathrm{x}} & \frac{\partial \mathrm{f_1}}{\partial \mathrm{v}} & \frac{\partial \mathrm{f_1}}{\partial \mathrm{y}} & \frac{\partial \mathrm{f_1}}{\partial \mathrm{u}} \\ \frac{\partial \mathrm{f_2}}{\partial \mathrm{x}} & \cdots & \cdots & \frac{\partial \mathrm{f_2}}{\partial \mathrm{u}} \\ \vdots & \cdots & \cdots & \vdots \\ \frac{\partial \mathrm{f_4}}{\partial \mathrm{x}} & \cdots & \cdots & \frac{\partial \mathrm{f_4}}{\partial \mathrm{u}} \end{bmatrix} = \begin{bmatrix} -1 & 0 & 0 & \alpha \\ \frac{\mathrm{m}\bar{\mathrm{x}}^{(\mathrm{m}-1)}}{(1+\bar{\mathrm{x}}^{\mathrm{m}})^2} & -1 & 0 & 0 \\ 0 & \beta & -1 & 0 \\ 0 & 0 & -\frac{\mathrm{n}\bar{\mathrm{y}}^{(\mathrm{n}-1)}}{(1+\bar{\mathrm{y}}^{\mathrm{n}})^2} & -1 \end{bmatrix}.$$

The entries of the above matrix are evaluated at the unique equilibrium, which is the intersection of the nullclines shown in Figure S48 D. Note that the nullclines and the corresponding equilibrium depend on the choice of the paramters. Decreasing β, for example, causes the equilibrium to move towards higher values of x and lower values of y. If β is too small, the periodic orbit is lost (Figure S48 D). If we assume for simplicity that $\alpha = \beta$ and $\mathrm{m} = \mathrm{n}$, we can numerically assess the eigenvalues of the Jacobian as shown in Figure S48 E: eigenvalues with positive real part, and therefore a periodic orbit, are found in the blue region.

23.2 Oscillator coupled to a molecular load and stationary approximation

We want to transmit the oscillations to a downstream molecule L. Without loss of generality, we will assume we can couple $\mathrm{rI2}$ to L (the same analysis can be easily carried out for $\mathrm{SW21}$, $\mathrm{SW12}$ and $\mathrm{rA1}$.) Following the main text, we will consider two different cases:

- $\mathrm{rI2}$ is consumed by the load. Chemical reactions: $\mathrm{rI2} + \mathrm{L} \xrightarrow{\mathrm{k_f}} \mathrm{L^a} \xrightarrow{\mathrm{k_r}} \mathrm{L}$.
- $\mathrm{rI2}$ is not consumed by the load. Chemical reactions: $\mathrm{rI2} + \mathrm{L} \xrightarrow{\mathrm{k_f}} \mathrm{L^a} \xrightarrow{\mathrm{k_r}} \mathrm{rI2} + \mathrm{L}$.

The overall model is as follows:

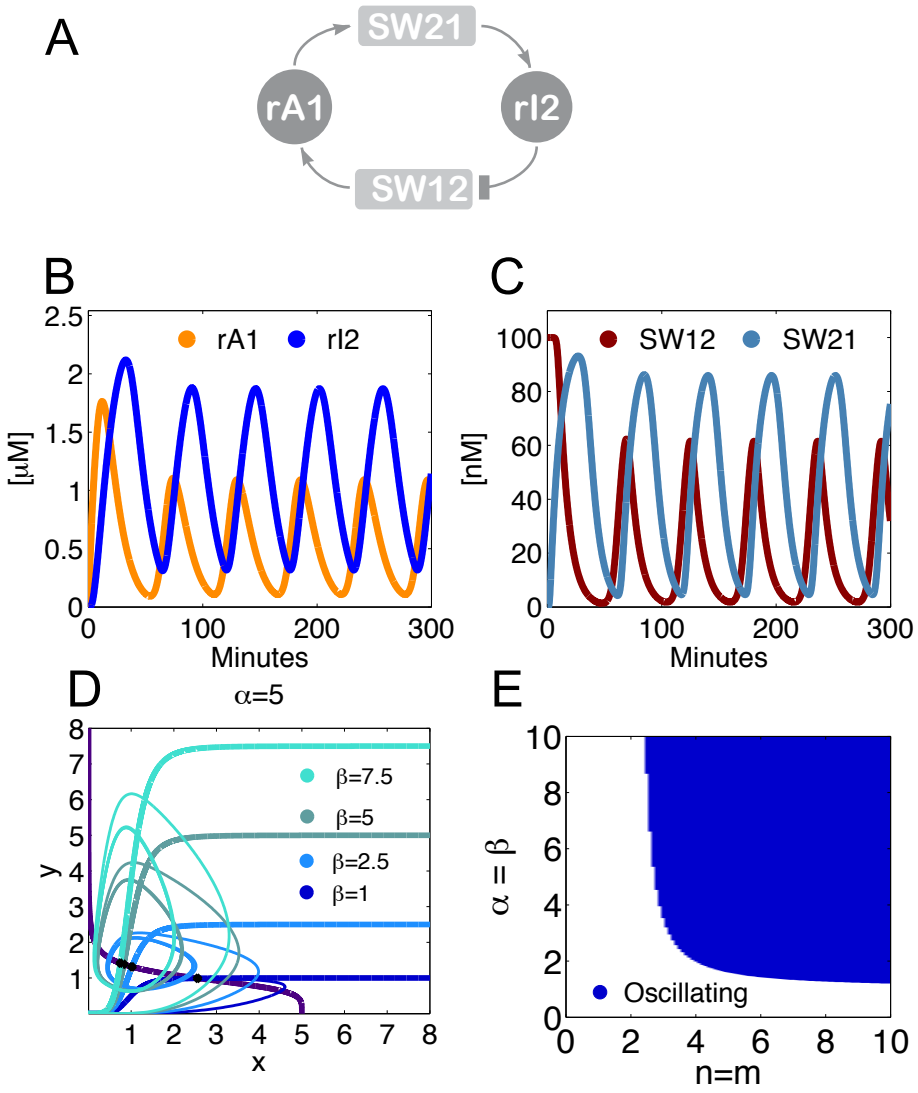

Figure S48: A. Scheme representing the simple oscillator model. B. Simulated rI2 and rA1 trajectories. C. Simulated SW12 and SW21 trajectories. D. Nullclines and corresponding trajectories (starting from zero initial conditions) for the nondimensional model of the oscillator, plotted for varying β and $\alpha = 5$. E. Oscillatory domain calculated for the nondimensional model when for simplicity we assume $\alpha = \beta$ and m=n. The nominal parameters used for these numerical simulations are chosen for illustrative purposes as: $\mathrm{k_p} = 0.05\,/\mathrm{s}$, $\mathrm{k_d} = 0.002\,/\mathrm{s}$, KA=KI=$.5\,\mu\mathrm{M}$, $[\mathrm{SW21^{tot}}] = [\mathrm{SW12^{tot}}] = 100\,\mathrm{nM}$, m=n=5, $\tau = 500\,\mathrm{s}$ (except for panel D, where β is varied).

$$\frac{\mathrm{d}[\mathrm{rA1}]}{\mathrm{dt}} = \mathrm{k_p}[\mathrm{SW12}] - \mathrm{k_d}[\mathrm{rA1}], \tag{5}$$

$$\tau\frac{\mathrm{d}[\mathrm{SW21}]}{\mathrm{dt}} = [\mathrm{SW21^{tot}}]\frac{\frac{[\mathrm{rA1}]^{\mathrm{m}}}{\mathrm{KA}^{\mathrm{m}}}}{1+\frac{[\mathrm{rA1}]^{\mathrm{m}}}{\mathrm{KA}^{\mathrm{m}}}} - [\mathrm{SW21}], \tag{6}$$

$$\frac{\mathrm{d}[\mathrm{rI2}]}{\mathrm{dt}} = \mathrm{k_p}\cdot[\mathrm{SW21}] - \mathrm{k_d}\cdot[\mathrm{rI2}]\underbrace{+\mathrm{k_r}\cdot[\mathrm{L^a}]\overbrace{-\mathrm{k_f}\cdot[\mathrm{L}][\mathrm{rI2}]}^{\mathrm{consumptive}}}_{\mathrm{non-consumptive}}, \tag{7}$$

$$\tau\frac{\mathrm{d}[\mathrm{SW12}]}{\mathrm{dt}} = [\mathrm{SW12^{tot}}]\frac{1}{1+\frac{[\mathrm{rI2}]^{\mathrm{n}}}{\mathrm{KI}^{\mathrm{n}}}} - [\mathrm{SW12}], \tag{8}$$

$$\frac{\mathrm{d}[\mathrm{L^a}]}{\mathrm{dt}} = -\mathrm{k_r}\cdot[\mathrm{L^a}] + \mathrm{k_f}\cdot[\mathrm{L}][\mathrm{rI2}], \tag{9}$$

and a schematic representation is given in Figure S49 A. For illustrative purposes, we choose $\mathrm{k_r} = 0.006\,/\mathrm{s}$ and $\mathrm{k_f} = 7.9\cdot 10^3\,/\mathrm{M/s}$.

The dynamics of $[\mathrm{rI2^{tot}}]$ are independent from the load in the consumptive coupling under pseudo steady state conditions

If we assume that $\mathrm{k_r} \approx \mathrm{k_d}$, we can show that the behavior of the total amount of $\mathrm{rI2}$ is independent from the load, when we look at timescale shorter than the oscillation period:

$$\begin{aligned}\frac{\mathrm{d}[\mathrm{rI2^{tot}}]}{\mathrm{dt}} &= \frac{\mathrm{d}[\mathrm{rI2}]}{\mathrm{dt}} + \frac{\mathrm{d}[\mathrm{L^a}]}{\mathrm{dt}} = \mathrm{k_p}\cdot[\mathrm{SW21}] - \mathrm{k_d}\cdot[\mathrm{rI2}] - \mathrm{k_f}\cdot[\mathrm{L}][\mathrm{rI2}] - \mathrm{k_r}\cdot[\mathrm{L^a}] + \mathrm{k_f}\cdot[\mathrm{L}][\mathrm{rI2}],\\ &= \mathrm{k_p}\cdot[\mathrm{SW21}] - \mathrm{k_d}\cdot([\mathrm{rI2}] + [\mathrm{L^a}]),\\ &= \mathrm{k_p}\cdot[\mathrm{SW21}] - \mathrm{k_d}\cdot[\mathrm{rI2^{tot}}].\end{aligned}$$

Since $[\mathrm{rI2^{tot}}]$ is independent from $[\mathrm{L}]$, it is legitimate to solve separately the dynamics of $[\mathrm{L^a}]$ in the short time scale.

$$\begin{aligned}\frac{\mathrm{d}[\mathrm{L^a}]}{\mathrm{dt}} &= -\mathrm{k_r}\cdot[\mathrm{L^a}] + \mathrm{k_f}\cdot([\mathrm{L^{tot}}] - [\mathrm{L^a}])([\mathrm{rI2^{tot}}](\mathrm{t}) - [\mathrm{L^a}]),\\ &= \mathrm{k_f}\cdot[\mathrm{L^{tot}}][\mathrm{rI2^{tot}}](\mathrm{t}) - [\mathrm{L^a}]\{\mathrm{k_r} + \mathrm{k_f}\cdot([\mathrm{L^{tot}}] + [\mathrm{rI2^{tot}}](\mathrm{t}))\} + \mathrm{k_f}\cdot[\mathrm{L^a}]^2.\end{aligned}$$

The above differential equation is Lipschitz continuous and has no finite escape time, therefore its solution is unique at all times. If $[\mathrm{rI2^{tot}}]$ is a positive forcing input to the system, the equation is an inhomogeneous ordinary differential equation which is driven by a periodic input.

It is possible to demonstrate that the solution to the above ordinary differential equation converges to a periodic orbit, whose period is determined by that of the input. An elegant

way to prove this is to use the so called "contractivity" theory, and follow the theorems proposed in Russo et al. [2010]. In short, it is sufficient to verify that the linearization of the differential equation is bounded by a negative constant and is therefore contractive. Since our system evolves on a compact and convex set, such property is global inside such set, and for any initial condition the system will converge to the periodic solution. If $\mathrm{d}[\mathrm{L^a}]/\mathrm{dt} = \mathrm{f}([\mathrm{L^a}], [\mathrm{rI2^{tot}}])$, we have:

$$\begin{aligned}\frac{\partial \mathrm{f}([\mathrm{L^a}], [\mathrm{rI2^{tot}}])}{\partial [\mathrm{L^a}]} &= -(\mathrm{k_r} + \mathrm{k_f} \cdot [\mathrm{rI2^{tot}}](\mathrm{t}) + \mathrm{k_f} \cdot [\mathrm{L^{tot}}]) + 2\mathrm{k_f} \cdot [\mathrm{L^a}], \\ &= -\left(\mathrm{k_r} + \mathrm{k_f} \cdot \underbrace{([\mathrm{rI2^{tot}}](\mathrm{t}) - [\mathrm{L^a}])}_{\geq 0} + \mathrm{k_f} \cdot \underbrace{([\mathrm{L^{tot}}] - [\mathrm{L^a}])}_{\geq 0} \right) \leq -\mathrm{c}^2,\end{aligned}$$

with $\mathrm{c} = \sqrt{\mathrm{k_r}} > 0$. This verifies the condition of contractivity, and therefore we know that the load dynamics always converge to a periodic solution, having the same period as the input $[\mathrm{rI2^{tot}}]$.

If we indicate as $[\overline{\mathrm{L^a}}]$ the stationary solution, we can estimate the convergence speed by looking at the dynamics of the error $\mathrm{e} = [\mathrm{L^a}] - [\overline{\mathrm{L^a}}]$:

$$\frac{\mathrm{de}}{\mathrm{dt}} = -\mathrm{k_r} \cdot \mathrm{e} - \mathrm{k_f} \cdot ([\mathrm{rI2^{tot}}] + [\mathrm{L^{tot}}]) \cdot \mathrm{e} + \mathrm{k_f} \cdot \mathrm{e}([\overline{\mathrm{L^a}}] + [\mathrm{L^a}]).$$

Take $\mathrm{V} = \mathrm{e}^2$ as a Lyapunov function for the system:

$$\begin{aligned}\frac{\mathrm{dV}}{\mathrm{dt}} = \frac{\mathrm{dV}}{\mathrm{de}}\frac{\mathrm{de}}{\mathrm{dt}} &= 2\mathrm{e} \cdot \left(-\mathrm{k_r} - \mathrm{k_f} \cdot ([\mathrm{rI2^{tot}}](\mathrm{t}) + [\mathrm{L^{tot}}] - [\mathrm{L^a}] - [\overline{\mathrm{L^a}}])\right) \cdot \mathrm{e}, \\ &= 2 \cdot \left(-\mathrm{k_r} - \mathrm{k_f} \cdot \underbrace{([\mathrm{rI2^{tot}}](\mathrm{t}) - [\mathrm{L^a}])}_{\geq 0} - \mathrm{k_f} \cdot \underbrace{([\mathrm{L^{tot}}] - [\overline{\mathrm{L^a}}])}_{\geq 0} \right) \cdot \mathrm{e}^2, \\ &= -2 \cdot \mathrm{Q} \cdot \mathrm{e}^2,\end{aligned}$$

where Q is a positive coefficient. Therefore, the dynamics of $[\mathrm{L^a}]$ converge exponentially to their stationary solution, and the speed is driven by the coefficient $\mathrm{Q} > \mathrm{k_r} \approx \mathrm{k_d}$.

To sum up, we can state that the equation:

$$\frac{\mathrm{d}[\mathrm{L^a}]}{\mathrm{dt}} = -\mathrm{k_r} \cdot [\mathrm{L^a}] + \mathrm{k_f} \cdot ([\mathrm{L^{tot}}] - [\mathrm{L^a}])([\mathrm{rI2^{tot}}](\mathrm{t}) - [\mathrm{L^a}])$$

converges exponentially to the stationary solution with a timescale that is faster than $1/\mathrm{k_r}$.

Quasi steady state approximation for the load dynamics

We have just shown that the dynamics of the load converge to the stationary solution with a speed $1/\mathrm{k_r}$: based on our choice of $\mathrm{k_r} = 0.006\,/\mathrm{s}$, we know that the speed of convergence is on the order of $160\,\mathrm{s}$. The nominal oscillator period for our simple model is around 1 hour, or $3600\,\mathrm{s}$. Therefore, it is legitimate to approximate the load dynamics with the quasi steady state expression:

$$[\widehat{\mathrm{L^a}}](\mathrm{t}) \approx [\mathrm{L^{tot}}] \left(1 - \frac{\mathrm{k_r}}{\mathrm{k_r} + \mathrm{k_f}[\mathrm{rI2}](\mathrm{t})}\right). \tag{10}$$

The validity of this approximation is illustrated in Figure S51 A and B, assuming that $\mathrm{k_r} = 0.006\,/\mathrm{s}$ and $\mathrm{k_f} = 7.9 \cdot 10^3\,/\mathrm{M/s}$.

Coupling efficiency: Assuming that $[\mathrm{rI2}](\mathrm{t})$ is a sinusoidal signal, we can use the static load approximation to evaluate the efficiency of the signal transmission. In particular, we can compute the amplitude of the load as a function of the oscillator amplitude. We will assume that $[\mathrm{rI2}](\mathrm{t}) = \mathrm{A_0} + \mathrm{A_1}\sin\omega\mathrm{t}$, where $\mathrm{A_0}, \mathrm{A_1} > 0$ and $\mathrm{A_0} > \mathrm{A_1}$. Define $\kappa = \mathrm{k_r}/\mathrm{k_f}$. The amplitude of the load oscillations is then given by:

$$\mathrm{A_L} = \frac{\mathrm{L^{tot}}}{2}\left(\frac{\kappa}{\kappa + (\mathrm{A_0} - \mathrm{A_1})} - \frac{\kappa}{\kappa + (\mathrm{A_0} + \mathrm{A_1})}\right).$$

By taking the derivative of $\mathrm{A_L}$ with respect to κ, and setting the derivative to zero, we can calculate the value of κ that maximizes $\mathrm{A_L}$:

$$\kappa_{\max} = \sqrt{\mathrm{A_0^2} - \mathrm{A_1^2}}.$$

For instance, take $\mathrm{A_0} \approx 1.1\,\mu\mathrm{M}$ and $\mathrm{A_1} \approx 0.8\,\mu\mathrm{M}$ as in the nominal oscillations for $[\mathrm{rI2}]$. Then, if we assume $\mathrm{k_r} = 0.006\,/\mathrm{s}$, the value of $\mathrm{k_f}$ that maximizes the load amplitude is $\mathrm{k_f} \simeq 7.9 \cdot 10^3\,/\mathrm{M/s}$. In the numerical simulations shown in the main paper, and reported here for the readers' convenience, we chose $\omega = 1 \cdot 10^{-3}\,\mathrm{rad/s}$, which is a good approximation of the nominal oscillation frequency of the system in the absence of load.

Perturbation of the oscillator caused by the load:

We can use the quasi steady state approximation of the $[\mathrm{L^a}](\mathrm{t})$ dynamics in the differential equation modeling $[\mathrm{rI2}]$. This will give us a simpler expression to gain insight into the perturbation (or retroactivity) effect of the load on the oscillator dynamics. We will again consider the two separate cases of consumptive and non-consumptive coupling.

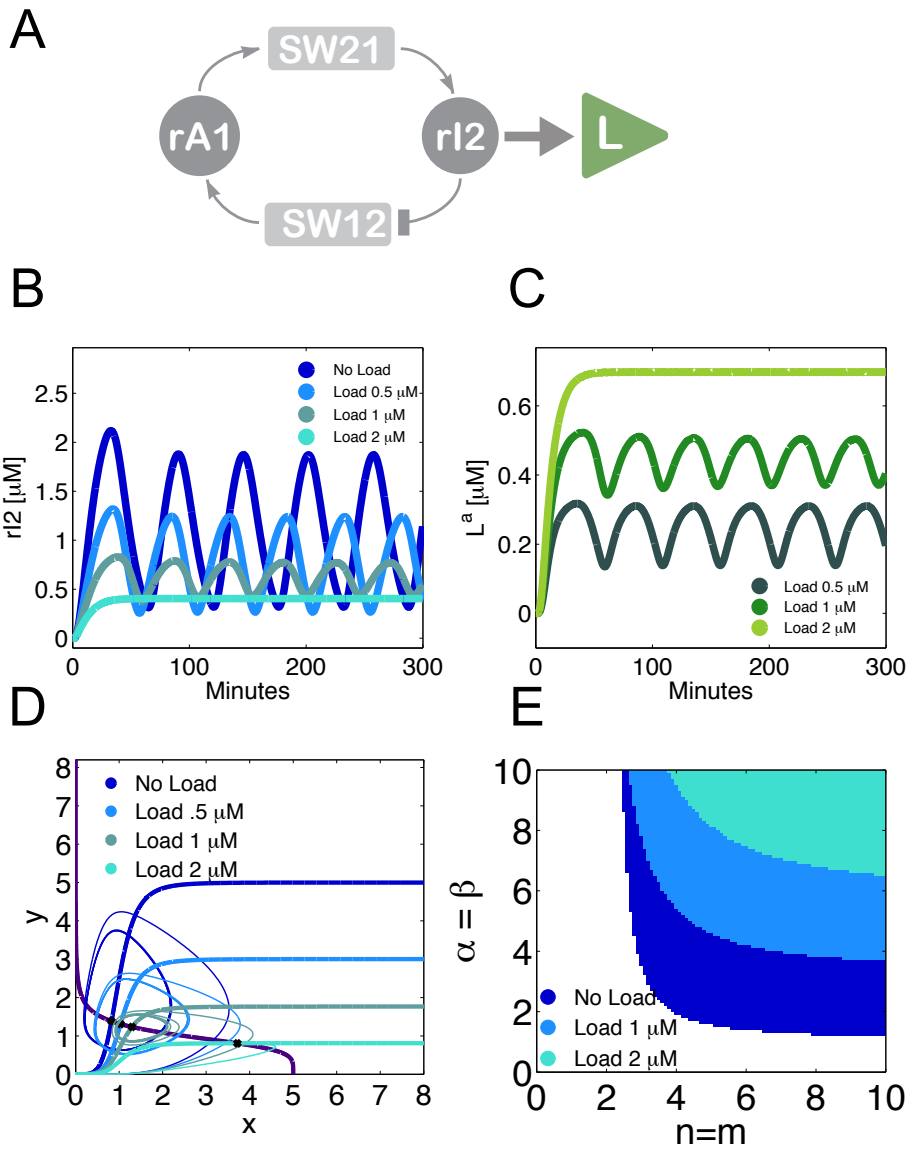

Figure S49: A. Schematic representation for the model problem oscillator coupled to a load. B. Trajectories of the rI2 species as a function of the total amount of load present in solution. C. Corresponding load trajectories. D. Nullclines and trajectories for the x and y variables of the nondimensional model of the oscillator coupled to a load, plotted for variable amounts of total load. E. Oscillatory domain of the nondimensional model, as a function of the total amount of load. The parameters are chosen as: $\mathrm{k_p} = 0.05\,/\mathrm{s}$, $\mathrm{k_d} = 0.002\,/\mathrm{s}$, KA=KI=.5 μM, $[\mathrm{SW21^{tot}}] = [\mathrm{SW12^{tot}}] = 100\,\mathrm{nM}$, m=n=5, $\tau = 500\,\mathrm{s}$, $\mathrm{k_r} = 0.006\,/\mathrm{s}$, $\mathrm{k_f} = 7.9 \cdot 10^3\,/\mathrm{M/s}$.

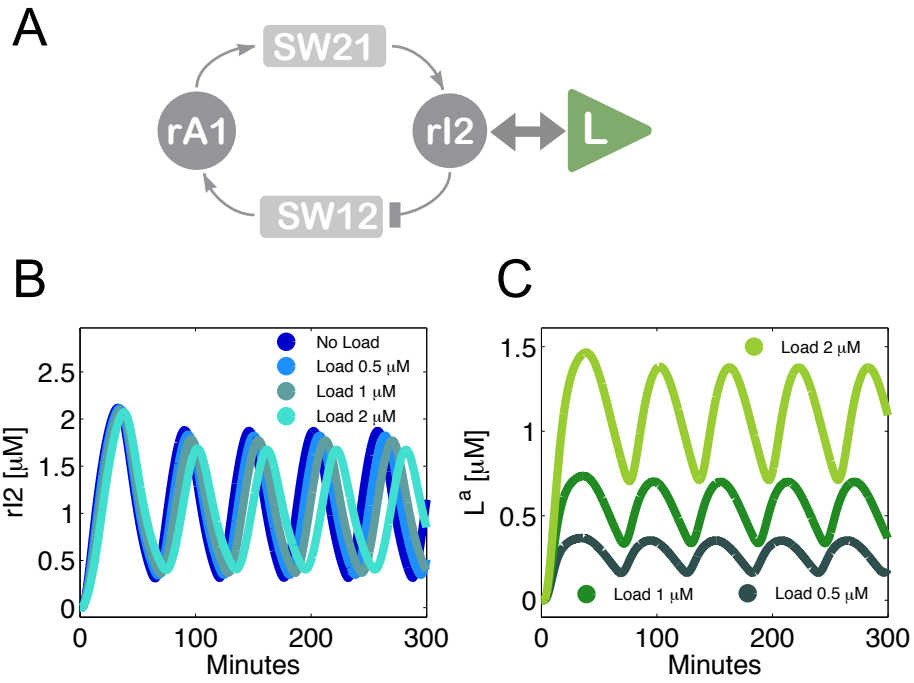

Figure S50: A. Scheme for the oscillator and load trajectories in the non consumptive coupling mode. B. Trajectories of the rI2 species as a function of the total amount of load present in solution. C. Corresponding load trajectories. The parameters are chosen as: $\mathrm{k_p} = 0.05\,/\mathrm{s}$, $\mathrm{k_d} = 0.002\,/\mathrm{s}$, KA=KI=.5 μM, $[\mathrm{SW21^{tot}}] = [\mathrm{SW12^{tot}}] = 100\,\mathrm{nM}$, m=n=5, $\tau = 500\,\mathrm{s}$, $\mathrm{k_r} = 0.006\,/\mathrm{s}$, $\mathrm{k_f} = 7.9 \cdot 10^3\,/\mathrm{M/s}$.

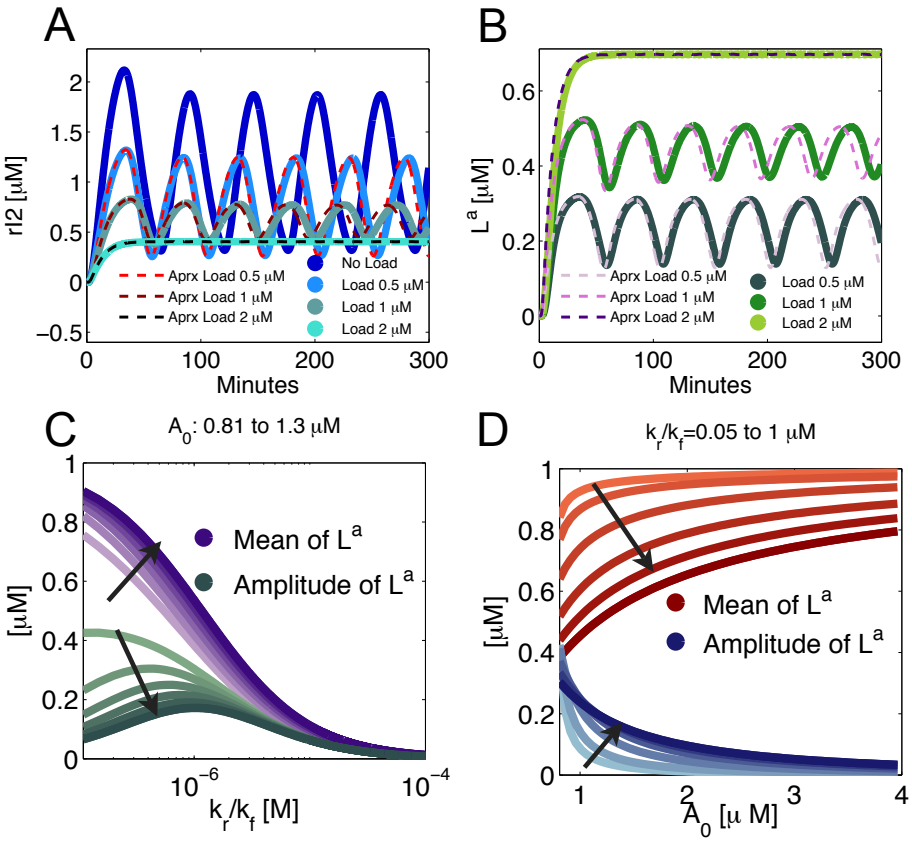

Figure S51: A. Numerical simulation comparing the full solution for the ordinary differential equations (5)–(9) (solid lines) to the solution when the load dynamics are approximated with the quasi steady state expression (10) (dashed lines). B. Load trajectories, comparison between the full solution (solid lines) and the quasi steady state approximation (dashed lines). C. Mean and amplitude of the active load $[\mathrm{L^a}]$ as a function of the ratio of $\mathrm{k_f}$ and $\mathrm{k_r}$, when the driving input is $\mathrm{rI2} = \mathrm{A_0} + \mathrm{A_1}\sin\omega\mathrm{t}$, with $\mathrm{A_0}$ varying between 0.81 (light color) and $1.3\,\mu\mathrm{M}$, and $\mathrm{A_1} = 0.8\mu\mathrm{M}$, $\omega = 0.001\,\mathrm{rad/s}$. D. Mean and amplitude of the active load signal $[\mathrm{L^a}]$ as a function of the baseline $\mathrm{A_0}$ for the input oscillating signal, for ratios of $\mathrm{k_f}$ and $\mathrm{k_r}$ varying between 0.05 and 1 μM. For A. and B. the parameters are chosen as: $\mathrm{k_p} = 0.05\,/\mathrm{s}$, $\mathrm{k_d} = 0.002\,/\mathrm{s}$, KA=KI=.5 μM, $[\mathrm{SW21^{tot}}] = [\mathrm{SW12^{tot}}] = 100\,\mathrm{nM}$, $[\mathrm{L^{tot}}] = 1\,\mu\mathrm{M}$, m=n=5, $\tau = 500\,\mathrm{s}$, $\mathrm{k_r} = 0.006\,/\mathrm{s}$, $\mathrm{k_f} = 7.9\cdot 10^3\,/\mathrm{M/s}$.

- **Consumptive coupling:** If we plug the load stationary solution into the consumptive dynamics of $[\mathrm{rI2}]$, we find:

$$\frac{\mathrm{d}[\widehat{\mathrm{rI2}}]}{\mathrm{dt}} = \mathrm{k_p} \cdot [\mathrm{SW21}] - \mathrm{k_d} \cdot [\widehat{\mathrm{rI2}}] \boxed{-\mathrm{k_f} \cdot [\widehat{\mathrm{rI2}}][\mathrm{L^{tot}}] \left(\frac{\mathrm{k_r}}{\mathrm{k_r}+\mathrm{k_f}[\widehat{\mathrm{rI2}}]}\right),} \tag{11}$$

$$[\widehat{\mathrm{L^a}}](\mathrm{t}) = [\mathrm{L^{tot}}] \left(1 - \frac{\mathrm{k_r}}{\mathrm{k_r} + \mathrm{k_f}[\widehat{\mathrm{rI2}}](\mathrm{t})}\right), \tag{12}$$

  where the box highlights the quasi steady state approximated perturbation term. Loosely speaking, the total amount of load linearly modulates an additional, bounded degradation term. (In fact, the perturbation term converges to $\mathrm{k_r} \cdot [\mathrm{L^{tot}}]$ for high values of $[\mathrm{rI2}]$.) The differential equations above were solved for varying amounts of $[\mathrm{L^{tot}}]$ numerically using MATLAB `ode23` routine; the results are shown in Figure S49 B and C and Figure S51 A and B. Initial conditions were chosen as: $[\mathrm{rA1}](0) = 0\,\mu\mathrm{M}$, $[\mathrm{SW21}](0) = 0\,\mathrm{nM}$, $[\mathrm{rI2}](0) = 0\,\mu\mathrm{M}$, $[\mathrm{SW12}](0) = 100\,\mathrm{nM}$, $[\mathrm{L^a}](0) = 0\,\mu\mathrm{M}$.

- **Non-consumptive coupling:** When we plug the stationary approximation of $[\mathrm{L^a}]$ into the non-consumptive version of equation (7), the resulting perturbation term is zero. This suggests that when $[\mathrm{L^a}]$ converges faster than the oscillator to stationary dynamics, the stationary perturbation on the oscillator nominal trajectories is negligible in the non-consumptive case. However, this does not provide information on the perturbation magnitude produced on the transient dynamics of the oscillator. Figure S50 B and C shows the oscillator and load trajectories simulated in the non-consumptive coupling case. Comparing these plots with those of Figure S49 B and C, we can notice that the perturbation on rI2 is negligible, and therefore the oscillating signal is better propagated to the load.

  The non-consumptive case has been considered in Del Vecchio et al. [2008], where the authors derive an analytical expression for the retroactivity induced by the load. Such derivation is based on time-scale separation arguments requiring arbitrarily fast rates $\mathrm{k_r}$ and $\mathrm{k_f}$. We highlight that we are not making this type of assumption in our analysis. Here, we will concisely summarize the results of Del Vecchio et al. [2008] in the context of our system, referring the reader to the original paper for more technical details.

  Following the reasoning in Del Vecchio et al. [2008], suppose that $\mathrm{k_r}$ is much faster than $\mathrm{k_d}$, and that the second order binding rate $\mathrm{k_f}$ has a resulting speed comparable to the kinetics of $\mathrm{k_r}$. It is then legitimate to assume that equation (9) reaches steady state very fast and can be equated to zero. We can then reason that the total RNA amount $[\mathrm{rI2^{tot}}] = [\mathrm{rI2}] + [\mathrm{L^a}]$ is the slow variable in the system, and we can rewrite equation (9) as a function of $[\mathrm{rI2^{tot}}]$. By setting such equation to zero, we can find $[\mathrm{L^a}]_\mathrm{s} = \mathrm{g}([\mathrm{rI2^{tot}}])$, i.e. we can express the dynamics of $[\mathrm{L^a}]$

on the slow manifold of the system. We can write:

$$\begin{aligned}\frac{\mathrm{d}[\mathrm{rI2}]_\mathrm{s}}{\mathrm{dt}} =& \frac{\mathrm{d}[\mathrm{rI2}^\mathrm{tot}]_\mathrm{s}}{\mathrm{dt}} - \frac{\mathrm{d}[\mathrm{L}^\mathrm{a}]_\mathrm{s}}{\mathrm{dt}},\\ =& \frac{\mathrm{d}[\mathrm{rI2}^\mathrm{tot}]_\mathrm{s}}{\mathrm{dt}} - \frac{\mathrm{d}\,\mathrm{g}([\mathrm{rI2}^\mathrm{tot}]_\mathrm{s})}{\mathrm{d}\,[\mathrm{rI2}^\mathrm{tot}]_\mathrm{s}}\frac{\mathrm{d}[\mathrm{rI2}^\mathrm{tot}]_\mathrm{s}}{\mathrm{dt}},\\ =& \frac{\mathrm{d}[\mathrm{rI2}^\mathrm{tot}]_\mathrm{s}}{\mathrm{dt}}\left(1 - \frac{\mathrm{d}\,\mathrm{g}([\mathrm{rI2}^\mathrm{tot}]_\mathrm{s})}{\mathrm{d}\,[\mathrm{rI2}^\mathrm{tot}]_\mathrm{s}}\right).\end{aligned}$$

The term $\mathrm{d}\,\mathrm{g}([\mathrm{rI2}^\mathrm{tot}]_\mathrm{s})/\mathrm{d}\,[\mathrm{rI2}^\mathrm{tot}]_\mathrm{s}$ is called *retroactivity*, and it expresses the effect that the load has on the dynamics of the molecule it binds to, after a fast transient. Follwing Del Vecchio et al. [2008], this term can be evaluated using the implicit function theorem. The final expression for the variable $[\mathrm{rI2}]_\mathrm{s}$ is:

$$\frac{\mathrm{d}[\mathrm{rI2}]_\mathrm{s}}{\mathrm{dt}} = \frac{\mathrm{d}[\mathrm{rI2}^\mathrm{tot}]_\mathrm{s}}{\mathrm{dt}}\left(1 - \frac{1}{1 + \frac{\kappa}{[\mathrm{L}^\mathrm{tot}]}\left(1 + \frac{[\mathrm{rI2}]_\mathrm{s}}{\kappa}\right)^2}\right),$$

where $\kappa = \mathrm{k_r}/\mathrm{k_f}$. Based on our choice of parameter values we cannot carry out a rigorous timescale separation. However, verifying the resulting retroactivity magnitude is still a useful exercise. Plugging into the above expression the numerical values: $\mathrm{k_r} = 6 \cdot 10^{-3}\,/\mathrm{s}$, $\mathrm{k_f} = 7.9 \cdot 10^3\,/\mathrm{M/s}$, we get $\kappa \approx 0.75\,\mu\mathrm{M}$. Let us assume that $[\mathrm{L}^\mathrm{tot}] \approx 1\,\mu\mathrm{M}$. Also, hypothesize that $[\mathrm{rI2}]_\mathrm{s}$ is in the order of $1\,\mu\mathrm{M}$: then, $(1 + \frac{[\mathrm{rI2}]_\mathrm{s}}{\kappa})^2 \approx 5$. Finally, since $\frac{\kappa}{[\mathrm{L}^\mathrm{tot}]} \approx 0.75$, we can conclude that in the presence of the load, the dynamics of $[\mathrm{rI2}]$, approximated on the slow manifold, are scaled by a factor 0.8 with respect to the load free trajectory (i.e., when $[\mathrm{rI2}^\mathrm{tot}] = [\mathrm{rI2}]$). However, if we were to operate at κ either much larger or much smaller than $1\mu M$, the retroactivity would rapidly approach zero. This would be consistent with our approximate result saying that a non-consumptive coupling causes negligible perturbations on the source of chemical signal.

We remark that we do not invoke a formal timescale separation argument in our stationary approximation, and it is therefore not possible to rigorously compare our results to those in Del Vecchio et al. [2008]. (However, we do justify the validity of our quasi steady state approximation of the load dynamics by comparing their convergence speed to the oscillator speed.)

Consumptive coupling: non-dimensional analysis of the oscillatory domain

The differential equations modeling the oscillator consumptively coupled to the load can be non-dimensionalized following the same procedure shown earlier.

Non-dimensional variables

$$\mathrm{x} = \frac{[\mathrm{rA1}]}{\mathrm{KA}} \quad \mathrm{v} = \frac{[\mathrm{SW21}]}{[\mathrm{SW21^{tot}}]}$$
$$\mathrm{y} = \frac{[\mathrm{rI2}]}{\mathrm{KI}} \quad \mathrm{u} = \frac{[\mathrm{SW12}]}{[\mathrm{SW12^{tot}}]}$$
$$\mathrm{w} = \frac{[\mathrm{L}]}{[\mathrm{L^{tot}}]}$$

Time rescaling

$$\tilde{\mathrm{t}} = \mathrm{t}/\tau$$

Non-dimensional parameters

$$\alpha = \frac{\mathrm{k_p}\,[\mathrm{SW12^{tot}}]}{\mathrm{k_d}\,\mathrm{KA}} \quad \beta = \frac{\mathrm{k_p}\,[\mathrm{SW21^{tot}}]}{\mathrm{k_d}\,\mathrm{KI}}$$
$$\delta = \frac{\mathrm{k_r}}{\mathrm{k_d}} \qquad \theta = \frac{\mathrm{k_f}[\mathrm{L^{tot}}]}{\mathrm{k_d}} \qquad \phi = \frac{\mathrm{k_f KI}}{\mathrm{k_d}}$$

Non-dimensional equations in $\tilde{t}$

$$\gamma\,\dot{\mathrm{x}} = \alpha\mathrm{u} - \mathrm{x} \tag{13}$$
$$\dot{\mathrm{v}} = \frac{\mathrm{x^m}}{1+\mathrm{x^m}} - \mathrm{v} \tag{14}$$
$$\gamma\,\dot{\mathrm{y}} = \beta\mathrm{v} - \mathrm{y}(1+\theta\mathrm{w}) \tag{15}$$
$$\dot{\mathrm{u}} = \frac{1}{1+\mathrm{y^n}} - \mathrm{u} \tag{16}$$
$$\gamma\,\dot{\mathrm{w}} = \delta(1-\mathrm{w}) - \phi\,\mathrm{wy} \tag{17}$$

Note that $\gamma = 1$. Equilibria will be indicated as $\bar{x}$, $\bar{u}$, $\bar{y}$, $\bar{u}$ and $\bar{w}$:

$$(13) = 0 \Longrightarrow \bar{\mathrm{x}} = \alpha\bar{\mathrm{u}}$$
$$(14) = 0 \Longrightarrow \bar{\mathrm{v}} = \frac{\bar{\mathrm{x}}^{\mathrm{m}}}{1+\bar{\mathrm{x}}^{\mathrm{m}}}$$
$$(15)\,\&\,(17) = 0 \Longrightarrow \bar{\mathrm{y}} \quad \text{is the positive solution of} \quad \phi\mathrm{y}^2 + \mathrm{y}(\delta(\theta+1) - \phi\beta\bar{\mathrm{v}}) - \delta\beta\bar{\mathrm{v}} = 0$$
$$(16) = 0 \Longrightarrow \bar{\mathrm{u}} = \frac{1}{1+\bar{\mathrm{y}}^{\mathrm{n}}}$$
$$(17) = 0 \Longrightarrow \bar{\mathrm{w}} = \frac{\delta}{\delta+\phi\bar{\mathrm{y}}}$$

The system Jacobian is:

$$\mathrm{J_y} = \begin{bmatrix} -1 & 0 & 0 & \alpha & 0 \\ \frac{\mathrm{m}\bar{\mathrm{x}}^{(\mathrm{m}-1)}}{(1+\bar{\mathrm{x}}^{\mathrm{m}})^2} & -1 & 0 & 0 & 0 \\ 0 & \beta & -1-\theta\bar{\mathrm{w}} & 0 & -\theta\bar{\mathrm{y}} \\ 0 & 0 & -\frac{\mathrm{n}\bar{\mathrm{y}}^{(\mathrm{n}-1)}}{(1+\bar{\mathrm{y}}^{\mathrm{n}})^2} & -1 & 0 \\ 0 & 0 & -\phi\bar{\mathrm{w}} & 0 & -\delta-\phi\bar{\mathrm{y}} \end{bmatrix}.$$

The nullclines of the system are represented in Figure S49 D. Increasing the load induces similar changes in the nullclines as decreasing β in the absence of load (Figure S48 D), which is equivalent to increasing the degradation rate for $[\mathrm{rI2}]$.

Figure S49 E shows how the oscillatory domain of the system shrinks when the total amount of load is increased. The figure is obtained by checking the eigenvalues of the Jacobian matrix $\mathrm{J_y}$.

23.3 Insulation

Consider the case where the load is coupled consumptively to the oscillator. How can the perturbation on the oscillator be reduced? When it is not practical to modify the binding rates that introduce the coupling, the only way to reduce perturbation is to use a minimal amount of load. We can overcome this restriction by coupling the oscillatory signal to a small amount of another molecular device, whose output is capable of amplifying the oscillator signal and driving large amounts of load. We will call this device an insulator, following the analysis proposed in Del Vecchio et al. [2008]. A schematic representation of this idea is shown in Figure S52 A.

An insulating device can be implemented easily as a small amount of a third switch, Ins, which is directly coupled to the oscillator. The RNA output from the insulating switch, InsOut, is used to drive the load.

The set of chemical reactions representing the insulator and load are:

$$\mathrm{rI2} + \mathrm{Ins} \xrightarrow{k_f} \mathrm{Ins^a}, \qquad \mathrm{Ins^a} \xrightarrow{k_r} \mathrm{Ins},$$

$$\mathrm{Ins^a} \xrightarrow{k_p^i} \mathrm{Ins^a} + \mathrm{InsOut},$$

$$\mathrm{InsOut} \xrightarrow{k_d^i} \emptyset,$$

$$\mathrm{InsOut} + \mathrm{L} \xrightarrow{k_f^i} \mathrm{L^a}, \qquad \mathrm{L^a} \xrightarrow{k_r^i} \mathrm{L},$$

$$\mathrm{Ins^{tot}} = \mathrm{Ins^a} + \mathrm{Ins}, \qquad \mathrm{L^{tot}} = \mathrm{L} + \mathrm{L^a}.$$

The differential equations corresponding to the oscillator and the insulated load are:

$$\begin{aligned}
\frac{\mathrm{d}[\mathrm{rA1}]}{\mathrm{dt}} &= \mathrm{k_p}\cdot[\mathrm{SW12}] - \mathrm{k_d}\cdot[\mathrm{rA1}],\\
\tau\frac{[\mathrm{SW21}]}{\mathrm{dt}} &= [\mathrm{SW21^{tot}}]\left(\frac{\left(\frac{[\mathrm{rA1}]}{\mathrm{KA}}\right)^{\mathrm{m}}}{1+\left(\frac{[\mathrm{rA1}]}{\mathrm{KA}}\right)^{\mathrm{m}}}\right) - [\mathrm{SW21}],\\
\frac{\mathrm{d}[\mathrm{rI2}]}{\mathrm{dt}} &= \mathrm{k_p}\cdot[\mathrm{SW21}] - \mathrm{k_d}\cdot[\mathrm{rI2}] - \mathrm{k_f}\cdot[\mathrm{Ins}][\mathrm{rI2}],\\
\tau\frac{[\mathrm{SW12}]}{\mathrm{dt}} &= [\mathrm{SW12^{tot}}]\left(\frac{1}{1+\left(\frac{[\mathrm{rI2}]}{\mathrm{KI}}\right)^{\mathrm{n}}}\right) - [\mathrm{SW12}],\\
\frac{\mathrm{d}[\mathrm{Ins}]}{\mathrm{dt}} &= \mathrm{k_r}\cdot[\mathrm{Ins^a}] - \mathrm{k_f}\cdot[\mathrm{Ins}][\mathrm{rI2}],\\
\frac{\mathrm{d}[\mathrm{InsOut}]}{\mathrm{dt}} &= \mathrm{k_p^i}\cdot[\mathrm{Ins^a}] - \mathrm{k_d^i}\cdot[\mathrm{InsOut}] - \mathrm{k_f^i}\cdot[\mathrm{InsOut}][\mathrm{L}],\\
\frac{\mathrm{d}[\mathrm{L}]}{\mathrm{dt}} &= \mathrm{k_r^i}\cdot([\mathrm{L^{tot}}] - [\mathrm{L}]) - \mathrm{k_f^i}\cdot[\mathrm{InsOut}][\mathrm{L}].
\end{aligned}$$

The parameters chosen for the numerical analysis of the system are: $\mathrm{k_p} = 0.05\,/\mathrm{s}$, $\mathrm{k_d} = 0.002\,/\mathrm{s}$, KA=KI=$.5\,\mu\mathrm{M}$, $[\mathrm{SW21^{tot}}] = [\mathrm{SW12^{tot}}] = 100\,\mathrm{nM}$, m=n=5, $\tau = 500\,\mathrm{s}$, $\mathrm{k_r} = 0.006\,/\mathrm{s}$, $\mathrm{k_f} = 7.9\cdot 10^3\,/\mathrm{M/s}$, $\mathrm{k_p^i} = 0.15\,/\mathrm{s}$, $\mathrm{k_d^i} = 0.006\,/\mathrm{s}$, $\mathrm{k_r^i} = 0.006\,/\mathrm{s}$ and $\mathrm{k_f^i} = 6\cdot 10^3\,/\mathrm{M/s}$. (Note that the oscillator parameters have not been changed from those used in Section 23.1.) All the parameters have been chosen for illustrative purposes. The above differential equations have been solved numerically using the MATLAB `ode23` solver, and are shown in Figure S52 B and C. Initial conditions were chosen as: $[\mathrm{rA1}](0) = 0\,\mu\mathrm{M}$, $[\mathrm{SW21}](0) = 0\,\mathrm{nM}$, $[\mathrm{rI2}](0) = 0\,\mu\mathrm{M}$, $[\mathrm{SW12}](0) = 100\,\mathrm{nM}$, $[\mathrm{Ins^a}](0) = 0\,\mathrm{nM}$, $[\mathrm{InsOut}](0) = 0\,\mu\mathrm{M}$, $[\mathrm{L^a}](0) = 0\,\mu\mathrm{M}$.

Non-dimensional model

This model can be rendered nondimensional with the same procedure adopted before:

Nondimensional variables

$$\mathrm{x} = \frac{[\mathrm{rA1}]}{\mathrm{KA}} \quad \mathrm{v} = \frac{[\mathrm{SW21}]}{[\mathrm{SW21^{tot}}]}$$
$$y = \frac{[\mathrm{rI2}]}{\mathrm{KI}}, \quad u = \frac{[\mathrm{SW12}]}{[\mathrm{SW12^{tot}}]}$$
$$\mathrm{h} = \frac{[\mathrm{Ins}]}{[\mathrm{Ins^{tot}}]} \quad \mathrm{z} = \frac{[\mathrm{InsOut}]}{[\mathrm{L^{tot}}]}$$
$$w = \frac{[\mathrm{L}]}{[\mathrm{L^{tot}}]}$$

Nondimensional parameters

$$\alpha = \frac{\mathrm{k_p}\,[\mathrm{SW12^{tot}}]}{\mathrm{k_d}\,\mathrm{KA}} \quad \beta = \frac{\mathrm{k_p}\,[\mathrm{SW21^{tot}}]}{\mathrm{k_d}\,\mathrm{KI}}$$
$$\delta = \frac{\mathrm{k_r}}{\mathrm{k_d}} \qquad \theta = \frac{\mathrm{k_f}[\mathrm{Ins^{tot}}]}{\mathrm{k_d}} \qquad \phi = \frac{\mathrm{k_f KI}}{\mathrm{k_d}}$$
$$\lambda = \frac{\mathrm{k_p^i}}{\mathrm{k_d}}\frac{[\mathrm{Ins^{tot}}]}{[\mathrm{L^{tot}}]} \quad \rho = \frac{\mathrm{k_f^i}}{\mathrm{k_d}}[\mathrm{L^{tot}}] \quad \xi = \frac{\mathrm{k_r^i}}{\mathrm{k_d}} \quad \psi = \frac{\mathrm{k_d^i}}{\mathrm{k_d}} \quad \gamma = \frac{1}{\mathrm{k_d}\,\tau}$$

Time rescaling

$\tilde{\mathrm{t}} = \mathrm{t}/\tau$

Nondimensional equations in $\tilde{t}$

$$\gamma\,\dot{\mathrm{x}} = \alpha \mathrm{u} - \mathrm{x} \tag{18}$$
$$\dot{\mathrm{v}} = \frac{\mathrm{x^m}}{1+\mathrm{x^m}} - \mathrm{v} \tag{19}$$
$$\gamma\,\dot{\mathrm{y}} = \beta \mathrm{v} - \mathrm{y}(1+\theta \mathrm{h}) \tag{20}$$
$$\dot{\mathrm{u}} = \frac{1}{1+\mathrm{y^n}} - \mathrm{u} \tag{21}$$
$$\gamma\,\dot{\mathrm{h}} = \delta(1-\mathrm{h}) - \phi\,\mathrm{hy} \tag{22}$$
$$\gamma\,\dot{\mathrm{z}} = \lambda(1-\mathrm{h}) - \mathrm{z}(\psi + \rho\,\mathrm{w}) \tag{23}$$
$$\gamma\,\dot{\mathrm{w}} = \xi(1-\mathrm{w}) - \rho\,\mathrm{zw} \tag{24}$$

Note that $\gamma = 1$.

Equilibria will be indicated as $\bar{x}$, $\bar{u}$, $\bar{y}$, $\bar{u}$, $\bar{h}$, $\bar{z}$ and $\bar{w}$:

$(18) = 0 \Longrightarrow \bar{\mathrm{x}} = \alpha\bar{\mathrm{u}}$

$(19) = 0 \Longrightarrow \bar{\mathrm{v}} = \dfrac{\bar{\mathrm{x}}^{\mathrm{m}}}{1+\bar{\mathrm{x}}^{\mathrm{m}}}$

$(20) = 0 \,\&\, (22) = 0 \Longrightarrow \bar{\mathrm{y}}$ is the positive solution of $\phi\mathrm{y}^2 + \mathrm{y}(\delta(\theta+1) - \phi\beta\bar{\mathrm{v}}) - \delta\beta\bar{\mathrm{v}} = 0$

$(21) = 0 \Longrightarrow \bar{\mathrm{u}} = \dfrac{1}{1+\bar{\mathrm{y}}^{\mathrm{n}}}$

$(22) = 0 \Longrightarrow \bar{\mathrm{h}} = \dfrac{\delta}{\delta+\phi\bar{\mathrm{y}}}$

$(23) = 0 \& (24) = 0 \Longrightarrow \bar{\mathrm{z}}$ is the positive solution of $\rho\psi\mathrm{z}^2 + \mathrm{z}(\xi(\rho+\psi) - \rho\lambda(1-\bar{\mathrm{h}})) = \xi\lambda(1-\bar{\mathrm{h}})$

$(24) = 0 \Longrightarrow \bar{\mathrm{w}} = \dfrac{\xi}{\xi+\rho\bar{\mathrm{z}}}$

The Jacobian of this set of equations is:

$$\mathrm{J}_{\mathrm{yIns}} = \begin{bmatrix} -1 & 0 & 0 & \alpha & 0 & 0 & 0 \\ \frac{\mathrm{m}\bar{\mathrm{x}}^{(\mathrm{m}-1)}}{(1+\bar{\mathrm{x}}^{\mathrm{m}})^2} & -1 & 0 & 0 & 0 & 0 & 0 \\ 0 & \beta & -1-\theta\bar{\mathrm{h}} & 0 & -\theta\bar{\mathrm{y}} & 0 & 0 \\ 0 & 0 & -\frac{\mathrm{n}\bar{\mathrm{y}}^{(\mathrm{n}-1)}}{(1+\bar{\mathrm{y}}^{\mathrm{n}})^2} & -1 & 0 & 0 & 0 \\ 0 & 0 & -\phi\bar{\mathrm{h}} & 0 & -\delta-\phi\bar{\mathrm{y}} & 0 & 0 \\ 0 & 0 & 0 & 0 & -\lambda & -\psi-\rho\bar{\mathrm{w}} & -\rho\bar{\mathrm{z}} \\ 0 & 0 & 0 & 0 & 0 & -\rho\bar{\mathrm{w}} & -\xi-\rho\bar{\mathrm{z}} \end{bmatrix}$$

The nullclines of the system are represented in Figure S52 D. Because the amount of insulator is small, the perturbation introduced in the oscillator dynamics is negligible: the oscillatory domain of the system is almost coincident with that of the oscillator in the absence of load. Figure S52 E shows the oscillatory domain corresponding to different amounts of total load. The figure is obtained by numerically checking the eigenvalues of the Jacobian matrix $\mathrm{J}_{\mathrm{yIns}}$.

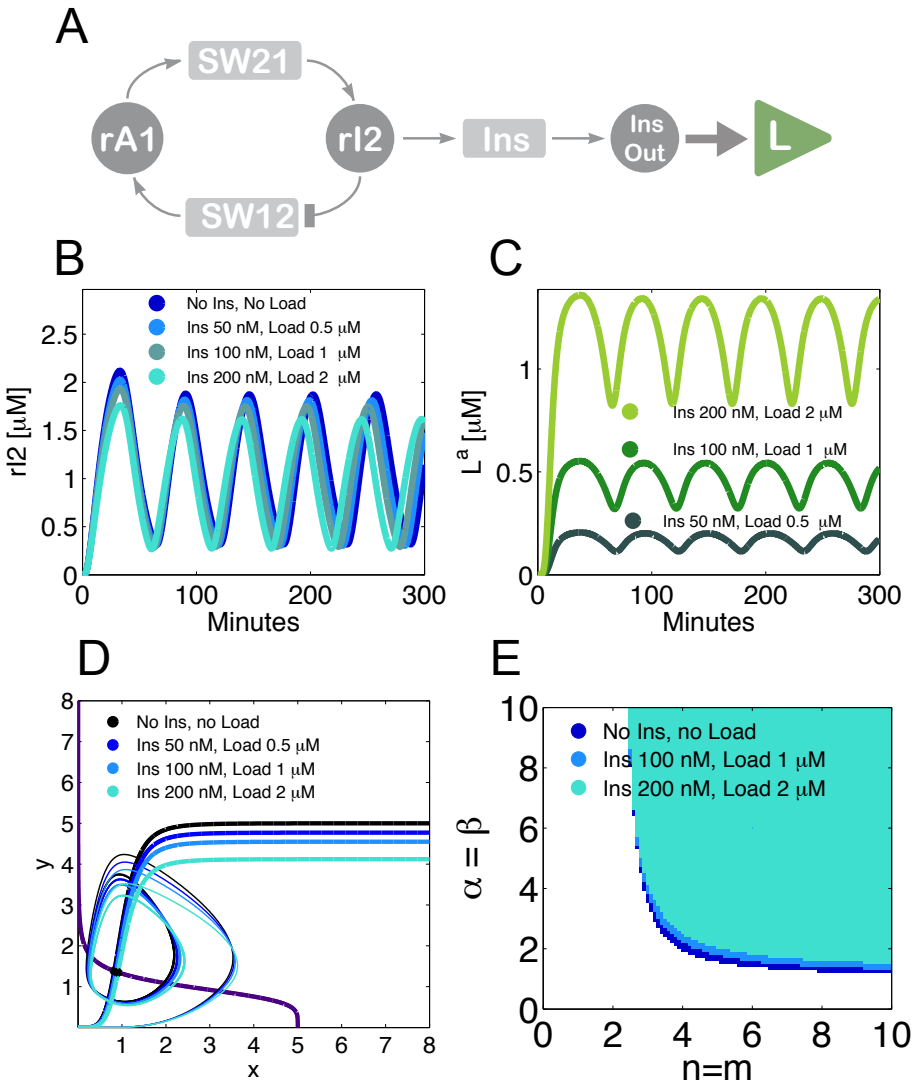

Figure S52: A. Scheme for the oscillator coupled to a load through an insulating switch. B. Trajectories of the oscillator rI2 species as a function of the total amount of insulating genelet and load. C. Corresponding load trajectories. D. Nullclines and trajectories for the nondimensional oscillator, x and y variables (corresponding to rA1 and rI2.) E. Oscillatory domain of the oscillator as a function of the total amount of insulator and load. The parameters are chosen as: $\mathrm{k_p} = 0.05\,/\mathrm{s}$, $\mathrm{k_d} = 0.002\,/\mathrm{s}$, KA=KI=.5 μM, $[\mathrm{SW21^{tot}}] = [\mathrm{SW12^{tot}}] = 100\,\mathrm{nM}$, m=n=5, $\tau = 500\,\mathrm{s}$, $\mathrm{k_r} = 0.006\,/\mathrm{s}$, $\mathrm{k_f} = 7.9 \cdot 10^3\,/\mathrm{M/s}$, $\mathrm{k_p^i} = 0.15\,/\mathrm{s}$, $\mathrm{k_d^i} = 0.006\,/\mathrm{s}$, $\mathrm{k_r^i} = 0.006\,/\mathrm{s}$ and $\mathrm{k_f^i} = 6 \cdot 10^3\,/\mathrm{M/s}$.

24 Core Oscillator Model

A set of DNA and RNA hybridization reactions, branch migration reactions, and Michaelis–Menten enzyme reactions for the core oscillator is as shown below. This set of reaction equations is identical to those used in the extended model of the Design I oscillator in Kim and Winfree [2011]. The standard mass action kinetics and Michaelis–Menten approximations were used to convert these reaction equations to a set of ordinary differential equations as outlined in Kim and Winfree [2011]. Figure S53 shows the schematic diagram for reaction equations excluding the reactions that involve incomplete degradation products (figure adapted from Kim and Winfree [2011]).

DNA/RNA hybridization and branch migration reactions

$$
\begin{aligned}
\mathrm{T12} + \mathrm{A2} &\xrightarrow{k_{TA,12}} \mathrm{T12 \cdot A2} && \text{(Activation)}\\
\mathrm{T21} + \mathrm{A1} &\xrightarrow{k_{TA,21}} \mathrm{T21 \cdot A1} && \text{(Activation)}\\
\mathrm{A1} + \mathrm{dI1} &\xrightarrow{k_{AI,1}} \mathrm{A1 \cdot dI1} && \text{(Annihilation)}\\
\mathrm{rA1} + \mathrm{dI1} &\xrightarrow{k_{rAI,1}} \mathrm{rA1 \cdot dI1} && \text{(Annihilation)}\\
\mathrm{A2} + \mathrm{rI2} &\xrightarrow{k_{AI,2}} \mathrm{A2 \cdot rI2} && \text{(Annihilation)}\\
\mathrm{T12 \cdot A2} + \mathrm{rI2} &\xrightarrow{k_{TAI,12}} \mathrm{T12} + \mathrm{A2 \cdot rI2} && \text{(Inhibition)}\\
\mathrm{T21 \cdot A1} + \mathrm{dI1} &\xrightarrow{k_{TAI,21}} \mathrm{T21} + \mathrm{A1 \cdot dI1} && \text{(Inhibition)}\\
\mathrm{rA1} + \mathrm{A1 \cdot dI1} &\xrightarrow{k_{AIrA,1}} \mathrm{rA1 \cdot dI1} + \mathrm{A1} && \text{(Release)}
\end{aligned}
$$

Michaelis–Menten enzyme reactions

$$
\begin{aligned}
\mathrm{RNAP} + \mathrm{T12 \cdot A2} &\underset{k_{-,ON,12}}{\overset{k_{+}}{\rightleftharpoons}} \mathrm{RNAP \cdot T12 \cdot A2} \xrightarrow{k_{cat,ON,12}} \mathrm{RNAP} + \mathrm{T12 \cdot A2} + \mathrm{rA1}\\
\mathrm{RNAP} + \mathrm{T21 \cdot A1} &\underset{k_{-,ON,21}}{\overset{k_{+}}{\rightleftharpoons}} \mathrm{RNAP \cdot T21 \cdot A1} \xrightarrow{k_{cat,ON,21}} \mathrm{RNAP} + \mathrm{T21 \cdot A1} + \mathrm{rI2}\\
\mathrm{RNAP} + \mathrm{T12} &\underset{k_{-,OFF,12}}{\overset{k_{+}}{\rightleftharpoons}} \mathrm{RNAP \cdot T12} \xrightarrow{k_{cat,OFF,12}} \mathrm{RNAP} + \mathrm{T12} + \mathrm{rA1}\\
\mathrm{RNAP} + \mathrm{T21} &\underset{k_{-,OFF,21}}{\overset{k_{+}}{\rightleftharpoons}} \mathrm{RNAP \cdot T21} \xrightarrow{k_{cat,OFF,21}} \mathrm{RNAP} + \mathrm{T21} + \mathrm{rI2}\\
\mathrm{RNaseH} + \mathrm{rA1 \cdot dI1} &\underset{k_{-,H,1}}{\overset{k_{+,H}}{\rightleftharpoons}} \mathrm{RNaseH \cdot rA1 \cdot dI1} \xrightarrow{k_{cat,H,1}} \mathrm{RNaseH} + \mathrm{dI1}
\end{aligned}
$$

Reactions involving incomplete degradation product

$$
\begin{aligned}
\mathrm{RNaseH} + \mathrm{A2 \cdot rI2} &\underset{k_{-,H,2}}{\overset{k_{+,H}}{\rightleftharpoons}} \mathrm{RNaseH \cdot A2 \cdot rI2} \xrightarrow{k_{cat,H,2}} \mathrm{RNaseH} + \mathrm{A2 \cdot sI2}\\
\mathrm{RNAP} + \mathrm{T12 \cdot A2 \cdot sI2} &\underset{k_{-,ON,12}}{\overset{k_{+}}{\rightleftharpoons}} \mathrm{RNAP \cdot T12 \cdot A2 \cdot sI2} \xrightarrow{k_{cat,ON,12}} \mathrm{RNAP} + \mathrm{T12 \cdot A2 \cdot sI2} + \mathrm{rA1}\\
\mathrm{A2} + \mathrm{sI2} &\underset{k_{s,-}}{\overset{k_{s,+}}{\rightleftharpoons}} \mathrm{A2 \cdot sI2}\\
\mathrm{T12} + \mathrm{A2 \cdot sI2} &\xrightarrow{k_{TA,12}} \mathrm{T12 \cdot A2 \cdot sI2}\\
\mathrm{T12 \cdot A2} + \mathrm{sI2} &\underset{k_{s,-}}{\overset{k_{s,+}}{\rightleftharpoons}} \mathrm{T12 \cdot A2 \cdot sI2}\\
\mathrm{rI2} + \mathrm{A2 \cdot sI2} &\xrightarrow{k_{AI,2}} \mathrm{A2 \cdot rI2} + \mathrm{sI2}
\end{aligned}
$$

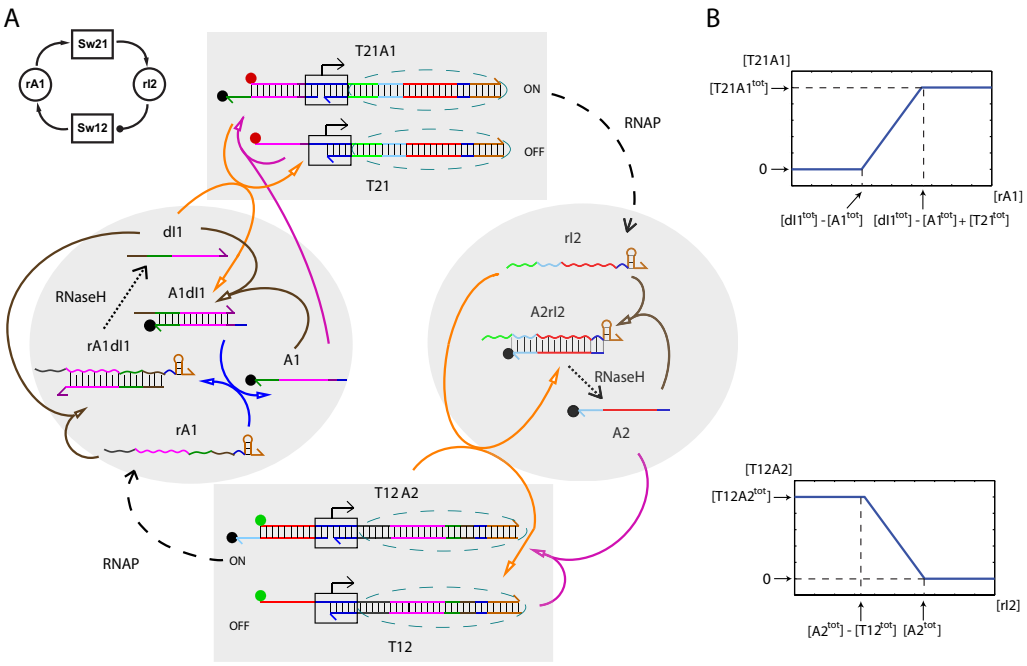

Figure S53: Enzyme and hybridization reactions for the core oscillator. **(A)** Reaction diagram. On the top left is a block diagram for the core oscillator, where arrowheads indicate activation or production and circular ends indicate inhibition. The block diagram corresponds to the detailed diagram highlighted in gray shaded areas: T21·A1 (ON-state switch SW21) and T21 (OFF-state switch SW21) are summarized by the SW21 block; RNA inhibitor rI2 together with its threshold, DNA activator A2, and their complex, A2·rI2, are summarized by the rI2 block; the SW12 and rA1 blocks are defined similarly. The sequence domains are color-coded to indicate identical or complementary sequences; for the switch templates, the dark blue sequence domain inside the rectangle indicates the T7 RNAP promoter sequence with arrows pointing in the direction of transcription, with transcription domains indicated by light blue dashed circles. For fluorescence monitoring, OFF-state switches are labeled with fluorophores, T21 with Texas Red or TYE 665 (red circle) and T12 with TAMRA or TYE 563 (green circle), and both activators A1 and A2 are labeled with Iowa Black RQ quenchers (black circle). Four types of hybridization reactions are indicated by arrows: activation (magenta), inhibition (orange), annihilation (brown), and release (blue). **(B)** Theoretical end-states of hybridization reactions in the absence of enzymes. As the input RNA inhibitor rI2 concentration increases, initially the free DNA activator A2 is consumed without affecting switch state. When all free A2 is consumed (i.e., $[\mathrm{rI2}] = [\mathrm{A2}^{\mathrm{tot}}] - [\mathrm{T12}^{\mathrm{tot}}]$), rI2 displaces A2 from the T12·A2 complex in stoichiometric amounts until all A2 is consumed (i.e., $[\mathrm{rI2}] = [\mathrm{A2}^{\mathrm{tot}}]$), resulting in a piece-wise linear graph. Similarly, the response of switch SW21 to rA1 input is a piece-wise linear graph.

25 Core Oscillator Model Fits

The kinetic simulations and parameter fittings were implemented in MATLAB. Differential equations were solved using the *ode23s* routine, while the cost function of model fits on experimental data was minimized using the *fmincon* routine. We settled on a cost

function using least-squared errors of fluorescence trajectories and characteristics of oscillation (oscillation amplitude, frequency, and damping coefficient) between simulation results and experiments. The error for each experiment is calculated as follows:

$$E = \frac{1}{\mathrm{N_f}} \sum_t ((\Delta \mathrm{T665_t})^2 + (\Delta \mathrm{T563_t})^2) + (\Delta \mathrm{Amp})^2 + (\Delta \mathrm{Fre})^2 + (\Delta \mathrm{Damp})^2,$$

where Δ indicates the difference between experimental and simulation values, $\mathrm{N_f}$ is the number of fluorescence measurements, T665 is the normalized TYE 665 fluorescence signal (calculated as [T21] for simulation results), T563 is the normalized TYE 563 fluorescence signal (calculated as [T12] for simulation results), Amp is the amplitude of oscillation, Fre is the frequency of oscillation, and Damp is the damping coefficient of oscillation. The experimental data were obtained at Caltech (set 5) (cf. Figure S49). The amplitude, frequency, and damping coefficient are calculated for TYE 665 fluorescence signals (calculated as [T21] for simulation results) with details provided in Kim and Winfree [2011]. The amplitude, frequency, and mean signal levels of the core oscillator are generally captured well (Figure S54).

During the fit, each parameter is constrained within a plausible range spanning about two orders of magnitude as shown below. For comparison, the maximum hybridization rates and the range of enzyme constants from other biochemical studies are listed [Rizzo et al., 2002, Martin and Coleman, 1987, Yurke and Mills, 2003].

Table S6: Parameter range for the model fits

Parameters	Lower limit	Upper limit	Other studies
$K_{M,ON}$ (nM)	10	300	15 - 37
$k_{cat,ON}$ (/s)	0.01	0.1	0.73 - 1.12
$K_{M,OFF}$ (μM)	0.1	3	0.1 - 1.1
$k_{cat,OFF}$ (/s)	0.001	0.03	0.11 - 0.18
$K_{M,H}$ (nM)	10	300	16 - 130
$k_{cat,H}$ (/s)	0.01	0.3	0.02 - 0.6
k_{TA}, k_{AI}, k_{TAI}, k_{rAI}, k_{AIrA} (/M/s)	3*10^3	3*10^5	0 - 3*10^6
$k_{s,+}$ (/M/s)	3*10^3	3*10^5	-
$k_{s,-}$ (/s)	0.01	1	-

While we can determine the concentrations of DNA species accurately by absorbance measurement (albeit with $< 5\%$ pipetting error), we also need to determine enzyme concentrations to obtain simulation results. For RNase H, the nominal concentration of enzyme stock quoted by the manufacturer was 1.25 μM. For RNAP, the T7 Megashortscript kit contains an enzyme mix, and we could only approximately determine RNAP

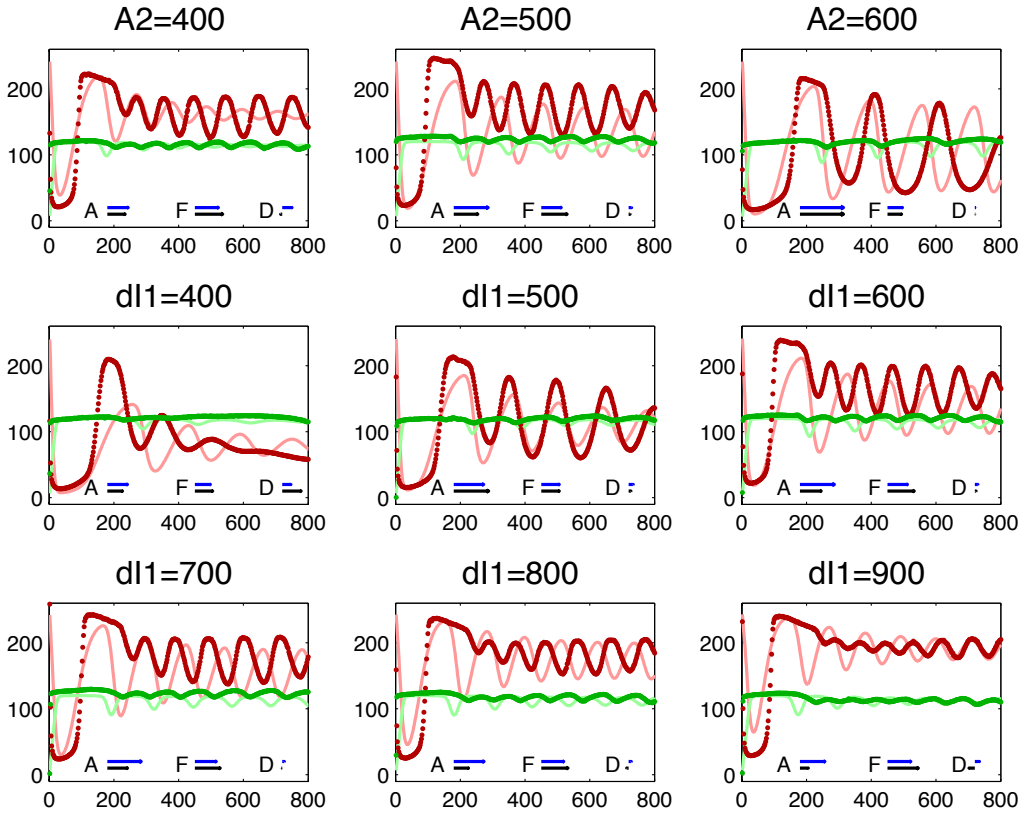

Figure S54: Experimental results and model fits for the core oscillator. Horizontal axes are time in minutes, and vertical axes are normalized concentrations in nM. The experimental time-courses are plotted as dots and simulation time-courses are plotted as lines in lighter shades: TYE 665 of T21 (red) and TYE 563 of T12 (green). The amplitude (A), frequency (F), and damping coefficients (D) of oscillation for experimental and simulation trajectories are shown as black arrows and blue arrows, respectively.

concentration by absorbance measurement (see Table S3). For simulation, we used [RNAP stock] = 1.25 μM and [RNase H stock] = 1.25 μM as the enzyme stock concentrations. In Section 33.1, we list the concentrations of DNA species and estimated enzyme concentrations.

26 Tweezers-coupling Mode I

In the first coupling scenario, dI1 is used to close the tweezers and rA1 is used to open the closed tweezers through toehold-mediated branch migration (Figure 3B). Whenever rA1 molecules become abundant in the system, rA1 hybridizes to dI1 in a stoichiometric manner. If dI1 is bound to the tweezers, rA1 opens up the tweezers; if dI1 is bound to the A1, A1 molecules are released, which in turn can bind to T21. Thus, opening

of the tweezers and turning on of the switch SW21 are both driven by rA1 accumulation. This means that the local maxima in the concentration of open tweezers (which corresponds to high Rhodamine Green fluorescence) are phase-shifted by approximately one-half period with respect to local maxima in the concentration of T21, OFF-state switch SW21 (which corresponds to high TYE 665 fluorescence). Before writing down the reaction equations for the closing and opening of the tweezers, we note that the tweezers interaction with the core oscillator can lead to several unintended hybridization reactions. Single-pair FRET characterization of DNA tweezers has shown that the closed state of DNA tweezers is typically heterogeneous including multimer formations such as tweezers bound to two closing strands on separate hands [Muller et al., 2006]. Thus, we could explore this possibility by modeling a multimer formation, where each hand of the tweezers is bound to a different dI1 molecule, hence the proper closing reaction is blocked (Figure S3). However, when measuring 'r' values, the ratio of minimum to maximum fluorescence measured off-line, for several different combinations of tweezers and dI1 concentrations (Table S5), we observed consistent 'r' values for the Rhodamine Green fluorescence of tweezers. Because we expect that the multimer formation is favored at high concentrations, the consistent 'r' values over a wide range of concentration changes indicate that the percentage of multimer formation is insignificant for typical operating conditions for this mode. Although we cannot rule out this possibility, we chose not to model this side reaction. Also note that the tweezers overhang sequences contain domains similar to the sequence of A1, such that there exists a side reaction between the tweezers and the OFF-state switch SW21, T21 (Figure S3). However, in this case both the fluorescence of tweezers and switch SW21 would be quenched resulting in lower baselines for both fluorophores. Thus, we chose not to explore this side reaction further. For simplicity, the tweezers closing and opening reactions were modeled as single-step reactions as shown below, where we assumed that the hybridization of dI1 on one of the tweezers overhangs leads to an instantaneous closing of the tweezers. The three load traces (set 4) were used to fit $k_{Twc,1}$ and $k_{Two,1}$. All the other parameters and enzyme concentrations were kept constant as determined using the core oscillator traces in Section 25. The error for each experiment is calculated as follows:

$$E = \frac{1}{\mathrm{N_f}} \sum_t ((\Delta \mathrm{T665_t})^2 + (\Delta \mathrm{RG_t})^2) + (\Delta \mathrm{Amp})^2 + (\Delta \mathrm{Fre})^2 + (\Delta \mathrm{Damp})^2,$$

where Δ indicates the difference between experimental and simulation values, $\mathrm{N_f}$ is the number of fluorescence measurements, T665 is the normalized TYE 665 fluorescence signal (calculated as [T21] for simulation results), RG is the normalized Rhodamine Green fluorescence signal, Amp is the amplitude of oscillation, Fre is the frequency of oscillation, and Damp is the damping coefficient of oscillation for TYE 665 fluorescence signal. The model fits are in good overall qualitative agreement with the experimental traces. In particular, the model predicts the correct trend for the load dependence of the core oscillator response (Figure S55, cf. Figure 6A,B). Interestingly, the amplitude change is nonlinear: the amplitude initially increases and then decreases with increasing tweezers load. The period always increases with increasing tweezers load.

26.1 Additional reactions

Tweezers closing and opening

$$\begin{aligned} \mathrm{TwI} + \mathrm{dI1} &\xrightarrow{k_{Twc,1}} \mathrm{TwI} \cdot \mathrm{dI1} \\ \mathrm{TwI} \cdot \mathrm{dI1} + \mathrm{rA1} &\xrightarrow{k_{Two,1}} \mathrm{TwI} + \mathrm{rA1} \cdot \mathrm{dI1} \end{aligned}$$

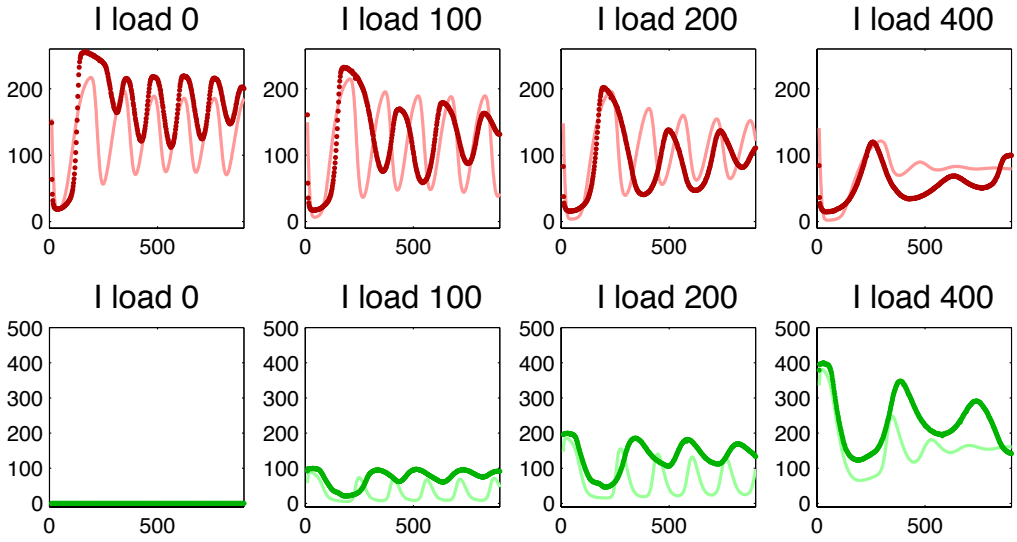

Figure S55: Experimental results (set 4) and model fits for the core oscillator and tweezers mode I. Horizontal axes are time in minutes, and vertical axes are normalized concentrations in nM. The experimental time-courses are plotted as dots and simulation time-courses are plotted as lines in lighter shades: TYE 665 of T21 (red) and Rhodamine Green of TwI (green).

27 Tweezers-coupling Mode II

In the second coupling scenario, A1 is used to close the tweezers and dI1 is used to open the closed tweezers through a toehold-mediated branch migration (Figure 3G). Whenever rA1 molecules become abundant in the system, A1 molecules are released from A1·dI1 complex, which can bind to T21, thus turning on switch SW21. At the same time, A1 can close the tweezers. Thus, closing of the tweezers and turning on of the switch SW21 are both driven by rA1 accumulation. This means that, in contrast to the coupling mode I, local maxima in the concentration of open tweezers (which corresponds to high Rhodamine Green fluorescence) are in-phase with local maxima in the concentration of T21 (which corresponds to high TYE 665 fluorescence). An almost perfect alignment of these two oscillation traces was observed, possibly because A1 hybridizes to the tweezers on roughly the same time-scale as it hybridizes to T21. Several side reactions may occur

for this tweezers-coupling scenario as well. For this mode, the amount of available closing strand A1 is not in excess of the tweezers concentration because A1 is mostly bound to T21 or dI1 (note that the total concentration of A1 is only 300 nM for set 4). Therefore, a multimer formation (e.g., TwII·A1·A1 complex) would be negligible (Figure S4). The RNA activator rA1 may close the tweezers, however, a 9 base toehold is available for A1 to displace rA1 from the tweezers and a 13 base toehold is available for dI1 to strip off rA1 bound to tweezers (Figure S4). Thus, we chose not to model this side reaction with rA1. We use the simple approach of Section 26 to model the tweezers closing and opening reactions. The three load traces (set 4) were used to fit $k_{Twc,2}$ and $k_{Two,2}$ with all the other parameters and enzyme concentrations fixed as determined in Section 25. The cost function is the same as the tweezers-coupling mode I (Section 26). The model fits are in good overall agreement with the experimental traces, again predicting the correct trend for the load dependence of the oscillation response (Figure S56, cf. Figure 6C,D): the amplitude decreases and the period increases with increasing tweezers load.

27.1 Additional reactions

Tweezers closing and opening

$$\begin{aligned} \mathrm{TwII} + \mathrm{A1} &\xrightarrow{k_{Twc,2}} \mathrm{TwII} \cdot \mathrm{A1} \\ \mathrm{TwII} \cdot \mathrm{A1} + \mathrm{dI1} &\xrightarrow{k_{Two,2}} \mathrm{TwII} + \mathrm{A1} \cdot \mathrm{dI1} \end{aligned}$$

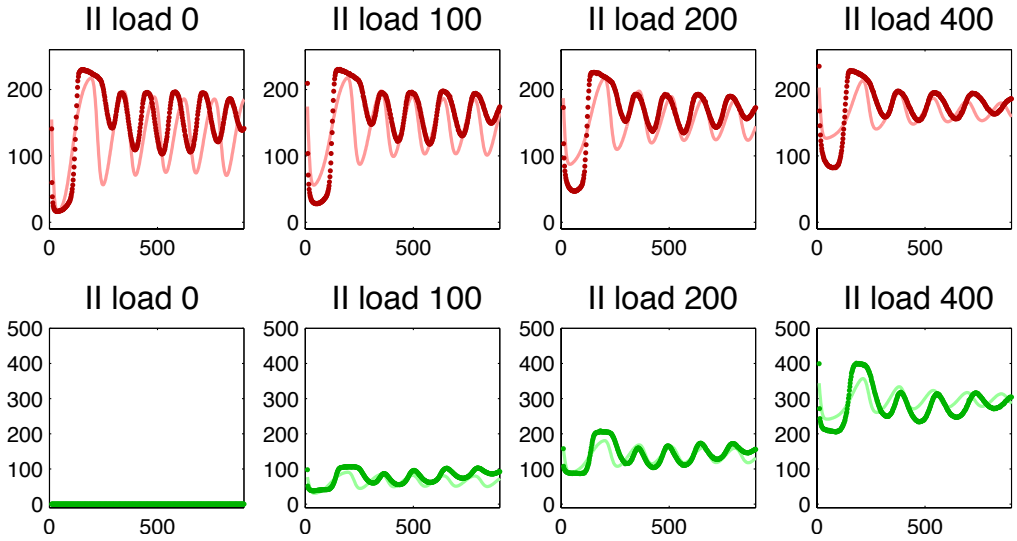

Figure S56: Experimental results (set 4) and model fits for the core oscillator and tweezers mode II. Horizontal axes are time in minutes, and vertical axes are normalized concentrations in nM. The experimental time-courses are plotted as dots and simulation time-courses are plotted as lines in lighter shades: TYE 665 of T21 (red) and Rhodamine Green of TwII (green).

28 Tweezers-coupling Mode III

In the third coupling scenario, rI2 is used to close the tweezers and the degradation of rI2 by RNase H is used to open the closed tweezers (Figure 3L). We expected the tweezers to be in a closed-state when rI2 is abundant. However, the tweezers response exhibited small amplitude possibly because the available closing strand rI2 was in great excess of tweezers leading to a multimer formation, or because the incomplete degradation products of rI2 were interfering with the closing reaction of tweezers (Figure S5). Also note that the tweezers overhang sequences contain domains similar to the sequence of A2, such that there exists a side reaction between the tweezers and the OFF-state switch SW12, T12 (Figure S5). Relatively strong back-action in the core oscillator was observed with only small changes in the response of tweezers. Thus, we designate this tweezers mode as failure, and do not simulate its behavior.

29 Tweezers-coupling Mode IV

In the fourth coupling scenario, rA1 is used to close the tweezers and the degradation of rA1 by RNase H as well as the toehold-mediated branch migration by dI1 to remove rA1 are used to open the closed tweezers. The potential interference of incomplete degradation products of rA1 could be responsible for the strong back-action in the core oscillator and yet very small changes in the response of tweezers (Figure S6). Similar to

the tweezers mode III, we designate this tweezers mode as failure, and do not simulate its behavior.

30 Tweezers-coupling Mode V (Insulator Circuit)

In this tweezers-coupling scenario, another switch template, which was denoted as Insulator (Ins) and is regulated by A2 and rI2, is used for the clocked synthesis of a third RNA species (InsOut) to drive tweezers (Figure 4A). For this mode, the available closing strand TwCls is only in slight excess of TwV such that a multimer formation (e.g., TwV·TwCls·TwCls complex) would be negligible (Figure S9). Because the output InsOut from the new genelet Ins operates TwV, the sequence similarity of TwV to other core oscillator components are largely eliminated, and therefore, we do not expect any significant side reactions for this tweezers-coupling mode. We use the simple approach used for tweezers mode I to model the tweezers closing and opening reactions. The list of reactions is presented below. The three load traces (set 4) were used to fit $k_{TA,Ins}$, $k_{TAI,Ins}$, $K_{M,ON,Ins}$, $k_{cat,ON,Ins}$, $K_{M,OFF,Ins}$, $k_{cat,OFF,Ins}$, $K_{M,H,5}$, $k_{cat,H,5}$, $k_{Twc,5}$, $k_{Two,5}$, and $k_{TwI,5}$. For this mode only, we used a 10% higher RNAP concentration to generate the simulation results, because of the relatively slow oscillation observed in the core oscillator without any tweezers load. All the other parameters including the RNase H concentration were kept constant. The cost function is the same as the one used for tweezers mode I. The model fits are in good overall qualitative agreement with the experimental traces (Figure S57, cf. Figure 6E,F): the amplitude decreases and the period increases with increasing tweezers load, yet the extent of distortions (retroactivity) of the core oscillations is small compared to other modes.

30.1 Additional reactions

Insulator switching

$$\begin{aligned} \mathrm{Ins} + \mathrm{A2} &\xrightarrow{k_{TA,Ins}} \mathrm{Ins \cdot A2} \\ \mathrm{Ins \cdot A2} + \mathrm{rI2} &\xrightarrow{k_{TAI,Ins}} \mathrm{Ins + A2 \cdot rI2} \end{aligned}$$

Insulator output production and degradation

$$\begin{aligned} \mathrm{RNAP + Ins \cdot A2} &\underset{k_{-,ON,Ins}}{\overset{k_+}{\rightleftharpoons}} \mathrm{RNAP \cdot Ins \cdot A2} \xrightarrow{k_{cat,ON,Ins}} \mathrm{RNAP + Ins \cdot A2 + InsOut} \\ \mathrm{RNAP + Ins} &\underset{k_{-,OFF,Ins}}{\overset{k_+}{\rightleftharpoons}} \mathrm{RNAP \cdot Ins} \xrightarrow{k_{cat,OFF,Ins}} \mathrm{RNAP + Ins + InsOut} \end{aligned}$$

$$\mathrm{RNaseH + TwCls \cdot InsOut} \underset{k_{-,H,5}}{\overset{k_{+,H}}{\rightleftharpoons}} \mathrm{RNaseH \cdot TwCls \cdot InsOut} \xrightarrow{k_{cat,H,5}} \mathrm{RNaseH + TwCls}$$

Tweezers closing and opening

$$\begin{aligned}
\mathrm{TwV} + \mathrm{TwCls} &\xrightarrow{k_{Twc,5}} \mathrm{TwV} \cdot \mathrm{TwCls} \\
\mathrm{TwV} \cdot \mathrm{TwCls} + \mathrm{InsOut} &\xrightarrow{k_{Two,5}} \mathrm{TwV} + \mathrm{TwCls} \cdot \mathrm{InsOut} \\
\mathrm{TwCls} + \mathrm{InsOut} &\xrightarrow{k_{TwI,5}} \mathrm{TwCls} \cdot \mathrm{InsOut}
\end{aligned}$$

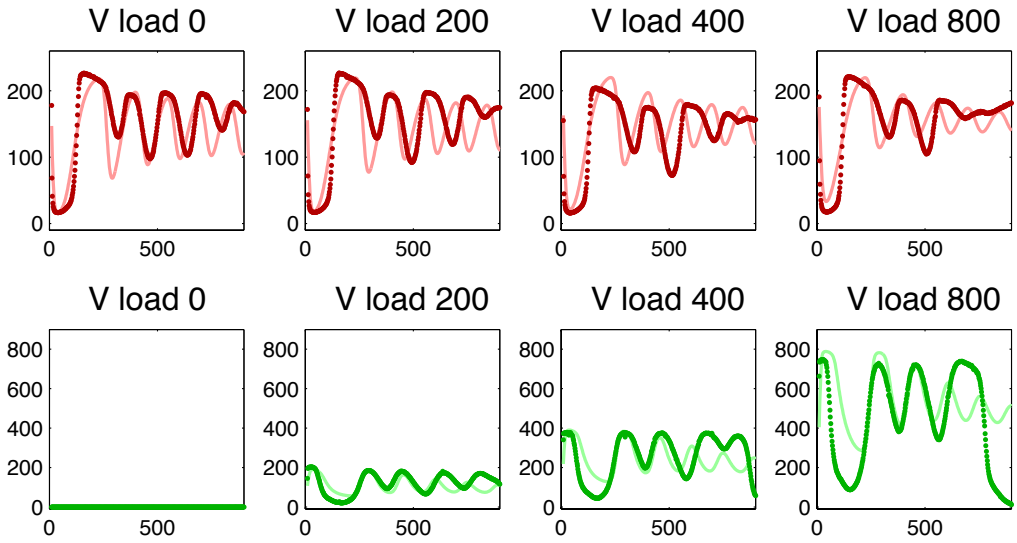

Figure S57: Experimental results (set 4) and model fits for the core oscillator and tweezers mode V. Horizontal axes are time in minutes, and vertical axes are normalized concentrations in nM. The experimental time-courses are plotted as dots and simulation time-courses are plotted as lines in lighter shades: TYE 665 of T21 (red) and Rhodamine Green of TwV (green).

31 Malachite Green Aptamer Production

In this final coupling scenario, the Malachite Green (MG) aptamer switch, TMG1, is used for the clocked synthesis of a third RNA species, MG aptamer (rMG) (Figure 5A). TMG1 binds to A1 as an activator of transcription much like T21, and therefore, rMG production is in parallel with the production of rI2. However, note that rMG is not degraded by RNase H because rMG does not bind to any DNA target strand. When MG is bound to the aptamer sequence rMG, it becomes highly fluorescent, which is used as a readout mechanism for the production of rMG. The MG aptamer binds its ligand tightly ($K_D < 1$ μM [Grate and Wilson, 1999]) and MG is abundantly available for binding (10 μM). We therefore assume that all transcribed rMG molecules bind to MG instantaneously and we do not separately model the rMG and MG binding reactions. The three load traces (set 3) were used to fit $k_{TA,MG}$, $k_{TAI,MG}$, $K_{M,ON,MG}$, $k_{cat,ON,MG}$, $K_{M,OFF,MG}$, and $k_{cat,OFF,MG}$. All the other parameters and enzyme concentrations were

kept constant. The error for each experiment is calculated as follows:

$$E = \frac{1}{\mathrm{N_f}} \sum_t \left((\Delta \mathrm{TR_t})^2 + \left(\frac{\Delta \mathrm{rMG_t}}{\max(\mathrm{rMG_t^{exp}}, \mathrm{rMG_t^{sim}})} \right)^2 \right) + (\Delta \mathrm{Amp})^2 + (\Delta \mathrm{Fre})^2 + (\Delta \mathrm{Damp})^2,$$

where Δ indicates the difference between experimental and simulation values, $\mathrm{N_f}$ is the number of fluorescence measurements, TR is the normalized Texas Red fluorescence signal (calculated as [T21] for simulation results), rMG is the normalized Malachite Green fluorescence signal (i.e., normalized Malachite Green aptamer concentration), Amp is the amplitude of oscillation, Fre is the frequency of oscillation, and Damp is the damping coefficient of oscillation for Texas Red fluorescence signal. The cost function is different from other modes in that the least-squared error on Malachite Green signal was normalized with respect to the maximum fluorescence of the experimental and simulation results at each time point. Unlike other tweezers-coupling modes, where the maximum Rhodamine Green signal is bounded, the Malachite Green signal is unbounded; We performed re-normalization of errors because we do not want the later time points to contribute disproportionately to the cost function. The model fits are in good overall qualitative agreement with the experimental traces, again predicting the correct trend for the load dependence of the oscillation response (Figure S58, cf. Figure 6G,H): the amplitude decreases and the period increases with increasing TMG1 switch load, similar to the tweezers-coupling mode II. This is consistent with the fact that both TwII and TMG1 drain A1 from the core oscillator.

31.1 Additional reactions

Malachite Green template switching

$$\begin{aligned} \mathrm{TMG1} + \mathrm{A1} &\xrightarrow{k_{TA,MG}} \mathrm{TMG1 \cdot A1} \\ \mathrm{TMG1 \cdot A1} + \mathrm{dI1} &\xrightarrow{k_{TAI,MG}} \mathrm{TMG1} + \mathrm{A1 \cdot dI1} \end{aligned}$$

Malachite Green aptamer production

$$\begin{aligned} \mathrm{RNAP} + \mathrm{TMG1 \cdot A1} &\underset{k_{-,ON,MG}}{\overset{k_+}{\rightleftharpoons}} \mathrm{RNAP \cdot TMG1 \cdot A1} \xrightarrow{k_{cat,ON,MG}} \mathrm{RNAP} + \mathrm{TMG1 \cdot A1} + \mathrm{rMG} \\ \mathrm{RNAP} + \mathrm{TMG1} &\underset{k_{-,OFF,MG}}{\overset{k_+}{\rightleftharpoons}} \mathrm{RNAP \cdot TMG1} \xrightarrow{k_{cat,OFF,MG}} \mathrm{RNAP} + \mathrm{TMG1} + \mathrm{rMG} \end{aligned}$$

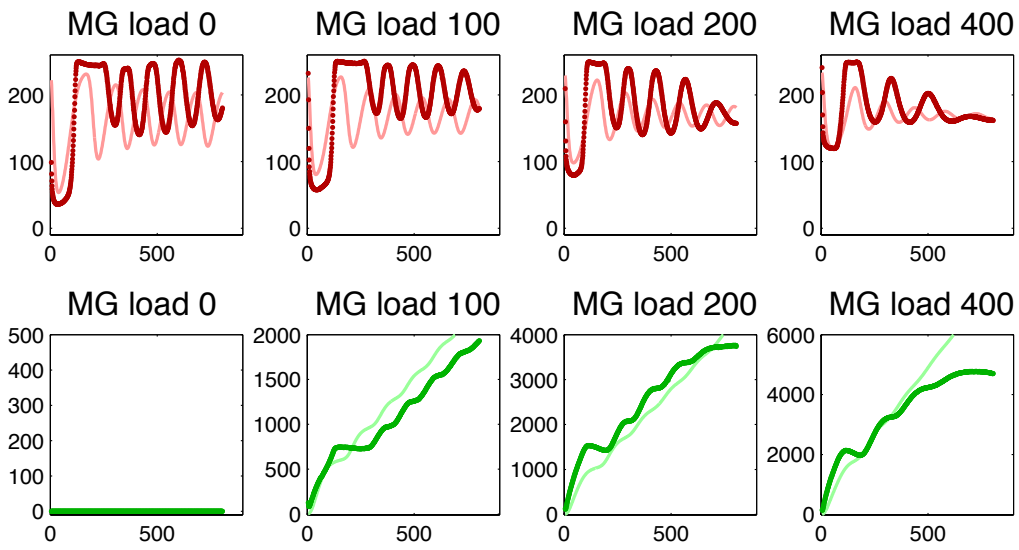

Figure S58: Experimental results (set 3) and model fits for the core oscillator and Malachite Green aptamer signal. Horizontal axes are time in minutes, and vertical axes are normalized concentrations in nM. The experimental time-courses are plotted as dots and simulation time-courses are plotted as lines in lighter shades: Texas Red of T21 (red) and Malachite Green aptamer (green).

32 Effects of the Load on the Oscillator Performance

The concentration of the load that is directly coupled to the oscillator is referred to as the nominal load concentration. For modes I-V, this is equivalent to the concentration of the tweezers added. For the MG aptamer producing system, the nominal load is given by the TMG1 genelet concentration. As an approximate measure of the actual work performed by the core oscillator, we define the effective load as the concentration of downstream tweezers (modes I-V) being switched from closed to open repeatedly. The effective load concentration is calculated as twice the maximum amplitude per oscillation of the tweezers load (max$\{2A_{TW}(n)\}$, $n = 1, 2, 3$) (see Section 16 for details). The relative amplitude and period changes for each tweezers-coupling mode are generally captured well (Figures S59 and S60, cf. Figure 7). One notable discrepancy is that, for mode I, the magnitude of period change is much greater in experiment ($\sim$150%) than in simulation ($\sim$30%) given 400 nM nominal tweezers load. This suggests that there are some important unmodeled reactions for mode I, because the same set of parameters could capture the core oscillator behaviors upon simple reduction of dI1 threshold reasonably well. One hypothesis is that the mode I tweezers interact with RNAP strongly (Figure S36).

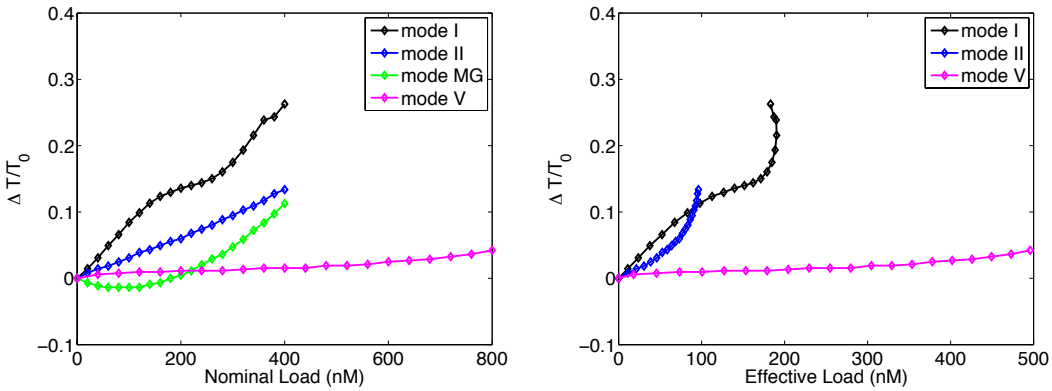

Figure S59: Relative period change as a function of the load concentration. Left: Nominal tweezers load vs. core oscillator period variation. Right: Effective tweezers load vs. core oscillator period variation.

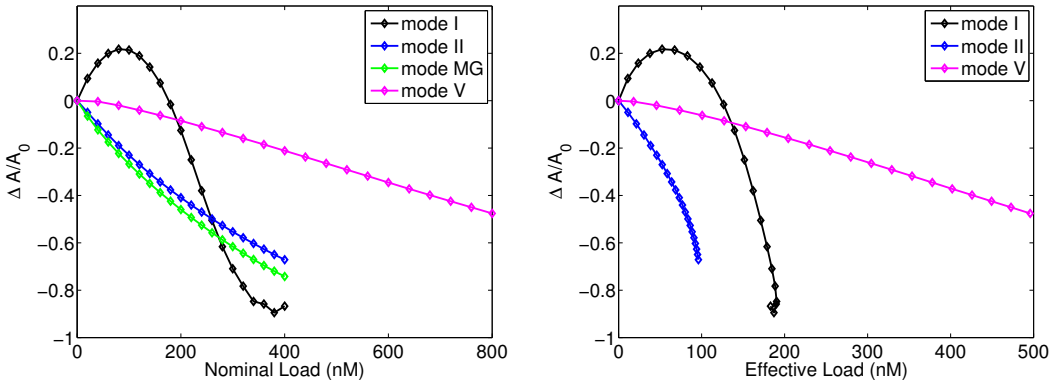

Figure S60: Relative amplitude change as a function of the load concentration. Left: Nominal tweezers load vs. core oscillator amplitude variation. Right: Effective tweezers load vs. core oscillator amplitude variation.

33 Summary of the Experimental and Modeling Conditions

33.1 Experimental conditions for threshold variation of core oscillator (set 5)

The experiments were performed at Caltech. RNAP and RNase H were purchased from Ambion. See Section 4 for details.

Reaction #	T21 (nM)	A1 (nM)	dI1 (nM)	T12 (nM)	A2 (nM)	RNAP (nM)	RNase H (nM)
1	250	300	600	120	400	96	9.7
2	250	300	600	120	500	96	9.7
3	250	300	600	120	600	96	9.7
4	250	300	400	120	500	96	9.7
5	250	300	500	120	500	96	9.7
6	250	300	600	120	500	96	9.7
7	250	300	700	120	500	96	9.7
8	250	300	800	120	500	96	9.7
9	250	300	900	120	500	96	9.7

33.2 Experimental conditions for tweezers-coupling modes (sets 3 and 4)

The experiments for data set 3 (mode MG) were performed at TUM using RNAP and RNase H purchased from Ambion. The experiments for data set 4 (modes I-V) were performed at Caltech using RNAP and RNase H purchased from Ambion. The enzyme batches used at TUM are different from those used at Caltech. We exclusively used experimental data set 4 for model fits, if available, because the enzyme batches are the same as those used for experimental data set 5 (threshold variations in the core oscillator). See Section 4 for details.

Tweezers mode I (set 4)

Reaction #	T21 (nM)	A1 (nM)	dI1 (nM)	T12 (nM)	A2 (nM)	TwI (nM)	RNAP (nM)	RNase H (nM)
1	250	300	650	120	550	0	96	9.7
2	250	300	650	120	550	100	96	9.7
3	250	300	650	120	550	200	96	9.7
4	250	300	650	120	550	400	96	9.7

Tweezers mode II (set 4)

Reaction #	T21 (nM)	A1 (nM)	dI1 (nM)	T12 (nM)	A2 (nM)	TwII (nM)	RNAP (nM)	RNase H (nM)
1	250	300	650	120	550	0	96	9.7
2	250	300	650	120	550	100	96	9.7
3	250	300	650	120	550	200	96	9.7
4	250	300	650	120	550	400	96	9.7

Tweezers mode III (set 4)

Reaction #	T21 (nM)	A1 (nM)	dI1 (nM)	T12 (nM)	A2 (nM)	TwIII (nM)	RNAP (nM)	RNase H (nM)
1	250	300	650	120	550	0	96	9.7
2	250	300	650	120	550	100	96	9.7
3	250	300	650	120	550	200	96	9.7
4	250	300	650	120	550	400	96	9.7

Tweezers mode IV (set 4)

Reaction #	T21 (nM)	A1 (nM)	dI1 (nM)	T12 (nM)	A2 (nM)	TwIV (nM)	RNAP (nM)	RNase H (nM)
1	250	300	650	120	550	0	96	9.7
2	250	300	650	120	550	100	96	9.7
3	250	300	650	120	550	200	96	9.7
4	250	300	650	120	550	400	96	9.7

Tweezers mode V (set 4)

Reaction #	T21 (nM)	A1 (nM)	dI1 (nM)	T12 (nM)	A2 (nM)	Ins (nM)	TwV (nM)	TwCls (nM)	RNAP (nM)	RNase H (nM)
1	250	300	650	120	550	0	100	150	105	9.7
2	250	300	650	120	550	50	200	250	105	9.7
3	250	300	650	120	550	100	400	450	105	9.7
4	250	300	650	120	550	200	800	850	105	9.7

Malachite Green aptamer production (set 3)

Reaction #	T21 (nM)	A1 (nM)	dI1 (nM)	T12 (nM)	A2 (nM)	TMG1 (nM)	RNAP (nM)	RNase H (nM)
1	250	250	700	120	500	0	96	9.7
2	250	250	700	120	500	100	96	9.7
3	250	250	700	120	500	200	96	9.7
4	250	250	700	120	500	400	96	9.7

33.3 Model parameters

Table S7. Model parameters for the core oscillator.

	i=2, j=1	i=1, j=2	Other studies
$K_{M,ON,ij}$ (nM)	93	61	15-37
$k_{cat,ON,ij}$ (/s)	0.020	0.039	0.73-1.12
$K_{M,OFF,ij}$ (μM)	0.14	0.20	0.1-1.1
$k_{cat,OFF,ij}$ (/s)	0.0071	0.0055	0.11-0.18
$K_{M,H,j}$ (nM)	41	84	16-130
$k_{cat,H,j}$ (/s)	0.027	0.214	0.02-0.6
$k_{TA,ij}$ (/M/s)	$1.57*10^5$	$3.60*10^3$	-
$k_{AI,j}$ (/M/s)	$4.75*10^3$	$3.17*10^4$	-
$k_{TAI,ij}$ (/M/s)	$9.99*10^3$	$5.31*10^4$	-
$k_{rAI,j}$ (/M/s)	$1.52*10^4$	-	-
$k_{AIrA,j}$ (/M/s)	$6.28*10^3$	-	-
$k_{s,+}$ (/M/s)	$6.88*10^3$	-	-
$k_{s,-}$ (/s)	0.181	-	-

Table S8. Model parameters for the tweezers.

During the fit, model parameters for the tweezers were constrained within the same upper and lower limits as the parameters for the core oscillators (cf. Table S6).

Parameters	Lower limit	Upper limit	Other studies
$K_{M,ON}$ (nM)	10	300	15 - 37
$k_{cat,ON}$ (/s)	0.01	0.1	0.73 - 1.12
$K_{M,OFF}$ (μM)	0.1	3	0.1 - 1.1
$k_{cat,OFF}$ (/s)	0.001	0.03	0.11 - 0.18
$K_{M,H}$ (nM)	10	300	16 - 130
$k_{cat,H}$ (/s)	0.01	0.3	0.02 - 0.6
k_{TA}, k_{TAI}, k_{Twc}, k_{Two}, k_{TwI} (/M/s)	$3*10^3$	$3*10^5$	0 - $3*10^6$

TwI	
$k_{Twc,1}$ (/M/s)	$1.16*10^5$
$k_{Two,1}$ (/M/s)	$3.58*10^4$

TwII	
$k_{Twc,2}$ (/M/s)	$1.14*10^5$
$k_{Two,2}$ (/M/s)	$1.04*10^4$

TwV	
$k_{Twc,5}$ (/M/s)	4.16*10^4
$k_{Two,5}$ (/M/s)	7.95*10^4
$k_{TwI,5}$ (/M/s)	8.40*10^3
$K_{M,ON,Ins}$ (nM)	90
$k_{cat,ON,Ins}$ (/s)	0.033
$K_{M,OFF,Ins}$ (μM)	0.22
$k_{cat,OFF,Ins}$ (/s)	0.0095
$K_{M,H,5}$ (nM)	122
$k_{cat,H,5}$ (/s)	0.149
$k_{TA,Ins}$ (/M/s)	8.38*10^3
$k_{TAI,Ins}$ (/M/s)	9.97*10^3

MG	
$K_{M,ON,MG}$ (nM)	59
$k_{cat,ON,MG}$ (/s)	0.012
$K_{M,OFF,MG}$ (μM)	2.86
$k_{cat,OFF,MG}$ (/s)	0.0017
$k_{TA,MG}$ (/M/s)	7.30*10^4
$k_{TAI,MG}$ (/M/s)	2.03*10^4

References

D. Del Vecchio and A. Ninfa and E. Sontag. Modular cell biology: Retroactivity and insulation. *Molecular Systems Biology*, 4:161, 2008.

J. Kim. *In vitro synthetic transcriptional networks*. PhD thesis, California Institute of Technology, 2007.

J. Kim and E. Winfree. Synthetic *in vitro* transcriptional oscillators. *Molecular Systems Biology*, 7:465, 2011.

S. Milburn, M. Goldrick, and M. Winkler. Compositions and methods for increasing the yields of in vitro rna transcription and other polynucleotide synthetic reactions, U. S. Patent 5,256,555, 1993.

D. Grate and C. Wilson. Laser-mediated, site-specific inactivation of RNA transcripts. *Proc Natl Acad Sci USA*, 96:6131–6136, 1999.

J. Mallet-Paret and H. L. Smith. The Poincaré-Bendixson theorem for monotone cyclic feedback systems. *Journal of Dynamics and Differential Equations*, 2:367–421, 1990.

C. T. Martin and J. E. Coleman. Kinetic analysis of T7 RNA polymerase-promoter interactions with small synthetic promoters. *Biochemistry*, 26:2690–2696, 1987.

B. K. Muller, A. Reuter, F. C. Simmel, and D. C. Lamb. Single-pair FRET characterization of DNA tweezers. *Nano Letters*, 6:2814–2820, 2006.

J. Rizzo, L. K. Gifford, X. Zhang, A. M. Gewirtz, and P. Lu. Chimeric RNA-DNA molecular beacon assay for ribonuclease H activity. *Mol. Cell. Probes*, 16:277–283, 2002.

G. Russo, M. di Bernardo and E. D. Sontag. Global entrainment of transcriptional systems to periodic inputs. *PLoS Comput Biol*, 6(4):e1000739, 2010.

B. Yurke and A. P. Mills, Jr. Using DNA to power nanostructures. *Genet. Program. Evol. Mach.*, 4:111–122, 2003.